Earth-Science Reviews 153 (2016) 238–273

Contents lists available at ScienceDirect

Earth-Science Reviews

journal homepage: www.elsevier.com/locate/earscirev

Source-to-sink transport processes of fluvial sediments in the South China Sea

Zhifei Liu [a,*], Yulong Zhao [a], Christophe Colin [b], Karl Stattegger [c], Martin G. Wiesner [d], Chih-An Huh [e], Yanwei Zhang [a], Xiajing Li [a], Penjai Sompongchaiyakul [f], Chen-Feng You [g], Chi-Yue Huang [g], James T. Liu [h], Fernando P. Siringan [i], Khanh Phon Le [j], Edlic Sathiamurthy [k], Wahyoe S. Hantoro [l], Jianguo Liu [m], Shouting Tuo [a], Shaohua Zhao [a], Shiwen Zhou [a], Ziding He [a], Yuchen Wang [a], Suratta Bunsomboonsakul [a,f], Yanli Li [a]

[a] State Key Laboratory of Marine Geology, Tongji University, Shanghai 200092, China
[b] UMR 8148 CNRS-GEOPS, Université de Paris-Sud, Orsay 91405, France
[c] Institute of Geosciences, University of Kiel, Kiel 24118, Germany
[d] Institute of Geology, University of Hamburg, Hamburg 20146, Germany
[e] Institute of Earth Sciences, Academia Sinica, Taipei 11529, Taiwan
[f] Department of Marine Science, Chulalongkorn University, Bangkok 10330, Thailand
[g] Department of Earth Sciences, National Cheng Kung University, Tainan 70101, Taiwan
[h] Department of Oceanography, National Sun Yat-sen University, Kaohsiung 80424, Taiwan
[i] Marine Science Institute, University of the Philippines, Quezon City 1101, Philippines
[j] Faculty of Petroleum, Hanoi University of Mining and Geology, Hanoi, Vietnam
[k] School of Marine Science and Environment, University Malaysia Terengganu, Kuala Terengganu 21030, Malaysia
[l] Research Center for Geotechnology, Indonesian Institute of Sciences, Bandung 40135, Indonesia
[m] South China Sea Institute of Oceanology, Chinese Academy of Sciences, Guangzhou 510301, China

ARTICLE INFO

Article history:
Received 18 September 2014
Received in revised form 10 August 2015
Accepted 12 August 2015
Available online 19 August 2015

Keywords:
Fluvial sediments
Clay mineralogy
Sediment geochemistry
Transport process
Mooring observation
Late Quaternary
Source-to-sink
South China Sea

ABSTRACT

The South China Sea offers an excellent case for studying source-to-sink transport processes of fluvial sediments among the global marginal seas. This study synthesizes existing clay mineralogical and geochemical data from ~1500 samples from the seafloor and surrounding rivers, deepwater mooring observation results, and high-resolution glacial–cyclic clay mineralogy records from six high-quality sediment cores. Source-to-sink sediment transport from the river mouth to the continental shelf and then to the abyssal basin is investigated at two time scales: modern process and Late Quaternary glacial cycles. The results firstly show the high diversity of clay mineralogical and geochemical compositions in riverbed surface sediments surrounding the South China Sea, e.g., dominant illite and chlorite in Taiwan, overwhelming majority of smectite in Luzon, dominant kaolinite in South China, and similar amounts of the four clay mineral species in Red and Mekong river systems. The formation of these fluvial sediments through chemical weathering in surrounding drainage systems is controlled principally by the East Asian monsoon climate with warm temperature and high precipitation, and subordinately by tectonic activity and specific lithological character. The basin-wide distribution of clay mineral assemblages combined with neodymium and strontium isotopic compositions reflects strong provenance control and differential settling effects. The differential settling of kaolinite in slightly saline and proximal regions relative to smectite in more saline and distal regions is well demonstrated in the South China Sea. Through combining clay mineralogical distributions on the seafloor with observed oceanic current systems, the modern transport pathways can be well established, e.g., in the northern South China Sea, illite and chlorite from Taiwan are mainly carried by contour currents with the strong influence of mesoscale eddies.

High-resolution sediment dynamic analysis for the Late Quaternary reveals different sediment transport patterns in the northern, western, and southern South China Sea when the land–sea configuration dramatically changed during glacial conditions. In the north, the terrigenous dispersal is mainly controlled by provenance supply and oceanic current transport. In the west, the clay mineral assemblage reflects variations of the prevailing surface current influenced by monsoon winds. In the south, the clay mineral input indicates intensive chemical weathering during interglacial periods and strengthened physical erosion during glacial periods. The transport of terrigenous sediments since the last glaciation is quantitatively reconstructed through studying two deepwater sediment cores located in the northern South China Sea. The relative contributions from three provenances (South China, Luzon, and Taiwan) highlight their distinct variability over the last 28 ka, implying that the

* Corresponding author at: State Key Laboratory of Marine Geology, Tongji University, 1239 Siping Road, Shanghai 200092, China.
E-mail address: lzhifei@tongji.edu.cn (Z. Liu).

http://dx.doi.org/10.1016/j.earscirev.2015.08.005

southward shift of the inter-tropical convergence zone (ITCZ) at 16 ka BP caused an increased sediment contribution from South China, the intensified influence of the Kuroshio Current intrusion controls more efficient westward transport of Luzon sediments, and the stronger deepwater current transports Taiwan-sourced sediments further westward from the last glaciation to the Holocene.

1. Introduction

Marginal seas connect continents with open oceans and they represent a critical component of the global source-to-sink system. Fluvial sediments eroded from drainage systems are transported and then deposited mostly on the continental shelf and slope of marginal seas, which are either the final sedimentary sink or the passage way to open ocean areas. The global discharge of fluvial sediments, annually amounting to 19 billion metric tons, is often confined to the coastal zone but can extend to or beyond the shelf edge if hydrodynamic processes are sufficiently active (Milliman and Farnsworth, 2011) or transport is facilitated by suitable conduits such as submarine canyons (Liu et al., 2013b). Consequently, marginal seas are ideal areas to study sediment source-to-sink transport process, especially when they are enclosed or semi-enclosed systems, in which case the sediment budget and transport pathways can be more easily defined. The South China Sea (SCS) offers such an excellent case for the source-to-sink study among the global marginal seas (Wang and Li, 2009).

As the largest marginal sea separating Asia from the Pacific, the SCS functions as a natural laboratory for studying land–sea interaction, because of its large input and excellent record of fluvial sediments. Being bordered by South China and Taiwan to the north, the Indochina Peninsula to the west, the Malay Peninsula, Sumatra, and Borneo to the south, and Luzon and Palawan to the east, the SCS receives more than 700 million metric tons (Mt) of fluvial sediments annually from numerous surrounding rivers, including several of the world's largest rivers, such as the Pearl River, the Red River, and the Mekong River (Liu and Stattegger, 2014; Fig. 1). This sediment input makes the SCS the largest receptacle of fluvial sediments among enclosed or semi-enclosed marginal seas worldwide (Milliman and Farnsworth, 2011).

These river-borne, terrigenous sediments are produced in quite diverse climatological, tectonic, and lithological settings surrounding the SCS. For example, the Paleozoic–Mesozoic sedimentary rocks, with minor intrusive and extrusive igneous rocks, of the high relief of the eastern Tibetan Plateau make up the majority of the upper and middle reaches of Red and Mekong river systems; they produce a clay mineral assemblage consisting predominantly of illite and chlorite with minor amounts of smectite and kaolinite (Liu et al., 2007b). In contrast, Cenozoic sedimentary and extrusive andesitic–basaltic rocks in Luzon produce the dominant smectite through chemical weathering (Liu et al., 2009b). Characteristic end-members in clay mineralogy and geochemistry from major drainage systems thus provide an efficient way to distinguish various provenances of fluvial sediments and to trace their transport pathway from source-to-sink in the SCS (Liu et al., 2010b, 2012).

Upon entering the SCS, fluvial sediments are further transported by various coastal, surface, and deep/bottom currents, which are related to the East Asian monsoon winds and intrusion of the subsurface Kuroshio Current and deepwater from the western Pacific through the Luzon Strait (e.g., Webster, 1994; Fang et al., 1998; Caruso et al., 2006; Qu et al., 2006; Zhao et al., 2014). Transport patterns of fluvial sediments have been derived based on surface sediments and depositional stratigraphic structures (Liu et al., 2009a; Liu et al., 2010b; Liu et al., 2011, 2013a) and more recently from deepwater mooring observations (Liu et al., 2014; Zhang et al., 2014; Zhao et al., 2014). Sediment transport in SCS deepwater environments is believed to be strongly influenced by large-scale and mesoscale oceanographic hydrodynamic processes, such as near-bottom contour currents and deep-reaching mesoscale eddies. The complexity of current systems along with various sediment composition end-members renders the SCS an interesting but challenging arena to understand sediment dynamics.

Most fluvial sediments that enter the SCS will ultimately deposit on the basin's seafloor because of the semi-enclosed physiography, though a minor amount of sediment could escape the system, such as via seasonal northward transport through the Taiwan Strait (Liu et al., 2008a; Huh et al., 2011). Sedimentary dispersal may involve gravity-flow processes, contourite deposition, hemipelagic advection, and pelagic sedimentation. The well-preserved sedimentary sequences characterized by high sedimentation rates and favorable carbonate preservation in the SCS are suitable for detailed paleoenvironmental reconstructions (Wang et al., 2000, 2014). Therefore, the SCS has drawn great attention from the global paleoceanographic and marine sedimentological communities. Over the past 20 years, at least 16 international cruises have taken place in the SCS with more than 200 sites drilled or cored for scientific purposes (see review by Wang et al., 2014). The marine stratigraphic and paleoenvironmental reconstruction studies based on sediment cores reach back 33 million years (Ma) until the earliest Oligocene when the SCS seafloor started spreading (Wang et al., 2000; Clift et al., 2002; Li et al., 2006). In this review, we synthesize existing clay mineralogical and geochemical data from seafloor and surrounding river surface samples and sedimentary cores as well as deepwater mooring observation results to address the source-to-sink transport process at both modern and Late Quaternary glacial–cyclic time scales.

2. Geological and environmental background

2.1. Geological setting

The South China Sea (SCS) is tectonically situated at the junction of the Eurasian, Pacific, and Indo-Australian plates. It developed from Cenozoic continental margin rifting and has undergone nearly a complete Wilson cycle from continental breakup to seafloor spreading and subduction (Expedition 349 Scientists, 2014). Opening of the SCS took place from ~32 to ~16 Ma during the Oligocene and early Miocene (Taylor and Hayes, 1980, 1983; Briais et al., 1993). Hypotheses for the opening mechanism include two major contrasting end-member tectonic models: southeastward extrusion of the Indochina Peninsula along the Ailao Shan-Red River fault zone owing to the India–Eurasia collision (Tapponnier et al., 1982; Briais et al., 1993) and slab pull and subduction of the proto-SCS under Sabah/Borneo (Taylor and Hayes, 1980, 1983; Hall, 2002). No consensus has been reached. Recently, results confirmed that the cessation of spreading occurred in the early Miocene (15–16 Ma), based on the International Ocean Discovery Program (IODP) Expedition 349 shipboard dating of microfossils in sediments immediately above the basaltic basement and deep tow magnetic anomalies (Expedition 349 Scientists, 2014; Li et al., 2014). The eastward subduction of the SCS oceanic crust along the Manila Trench must have started by the latest Oligocene at ~24 Ma as indicated by uplift of the Zambales Range or during early Miocene at 17 Ma as signaled by the first eruption of volcanoes along the Cordillera Central in Luzon (Hayes and Lewis, 1984). Since then, the subduction has developed an active continental margin with an accretionary prism and a volcanic arc between Taiwan and Luzon, and the SCS has become progressively semi-enclosed.

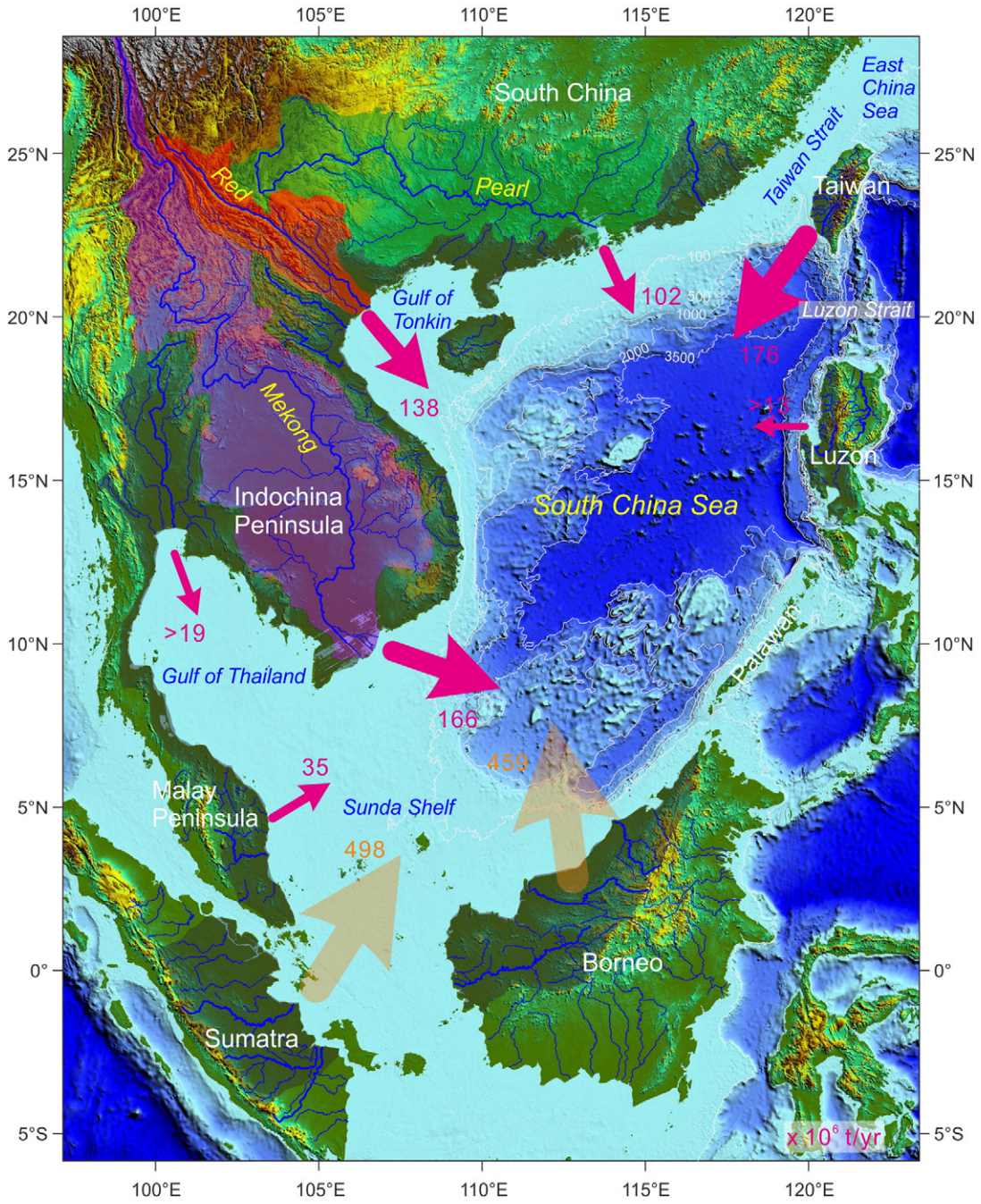

Fig. 1. Fluvial drainage systems and their annual suspended sediment discharge to the South China Sea (SCS) (revised after Liu and Stattegger, 2014). Red arrows with numbers indicate observed fluvial sediment discharge (in million metric tons, Mt, annually) from the Indochina Peninsula in the west (Milliman and Syvitski, 1992; Milliman and Farnsworth, 2011), South China in the north (Milliman and Farnsworth, 2011; Zhang et al., 2012), Taiwan in the northeast (Dadson et al., 2003), Luzon in the east (Liu et al., 2009b), and the Malay Peninsula in the south (Liu et al., 2012), respectively. Pink arrows with numbers show modal sediment discharge from Sumatra and Borneo in the south (Milliman et al., 1999). See Table 1 for detailed sediment discharge data of all major rivers.

Through the plate tectonic evolution of the SCS, characteristic tectonic and lithological settings with a strong north–south contrast have been configured for the surrounding continents and islands (Commission for the Geological Map of the World, 1975; Fig. 2). In the north, South China is mainly composed of Mesozoic–Cenozoic granitic rocks and Paleozoic sedimentary rocks (limestone, shale, and sandstone) in the eastern part and of Paleozoic–Mesozoic carbonate rocks (mainly Permian–Triassic limestone) in the western part. South China has been tectonically stable (cratonic) since the Mesozoic. In contrast, Taiwan represents an extremely active, exposed accretionary prism developed by eastward subduction of the SCS oceanic lithosphere beneath the Philippine Sea Plate after the arc–continent collision at 6.5 Ma (Huang et al., 1997). Tertiary sedimentary rocks (mainly sandstone and mudstone) with associated pre-Tertiary metamorphic rocks in the Central Range and volcanic arc complex in the Coastal Range make up the Cenozoic stratigraphy of Taiwan.

West of the SCS, the Indochina Peninsula with neighboring eastern Tibetan Plateau consists mainly of Paleozoic–Mesozoic sedimentary rocks with minor intrusive and extrusive igneous rocks (Liu et al., 2007b; Fig. 2). A small quantity of igneous rocks and Precambrian metamorphic rocks is exposed along the Ailao Shan-Red River fault zone and in the coastal mountain range of the eastern peninsula.

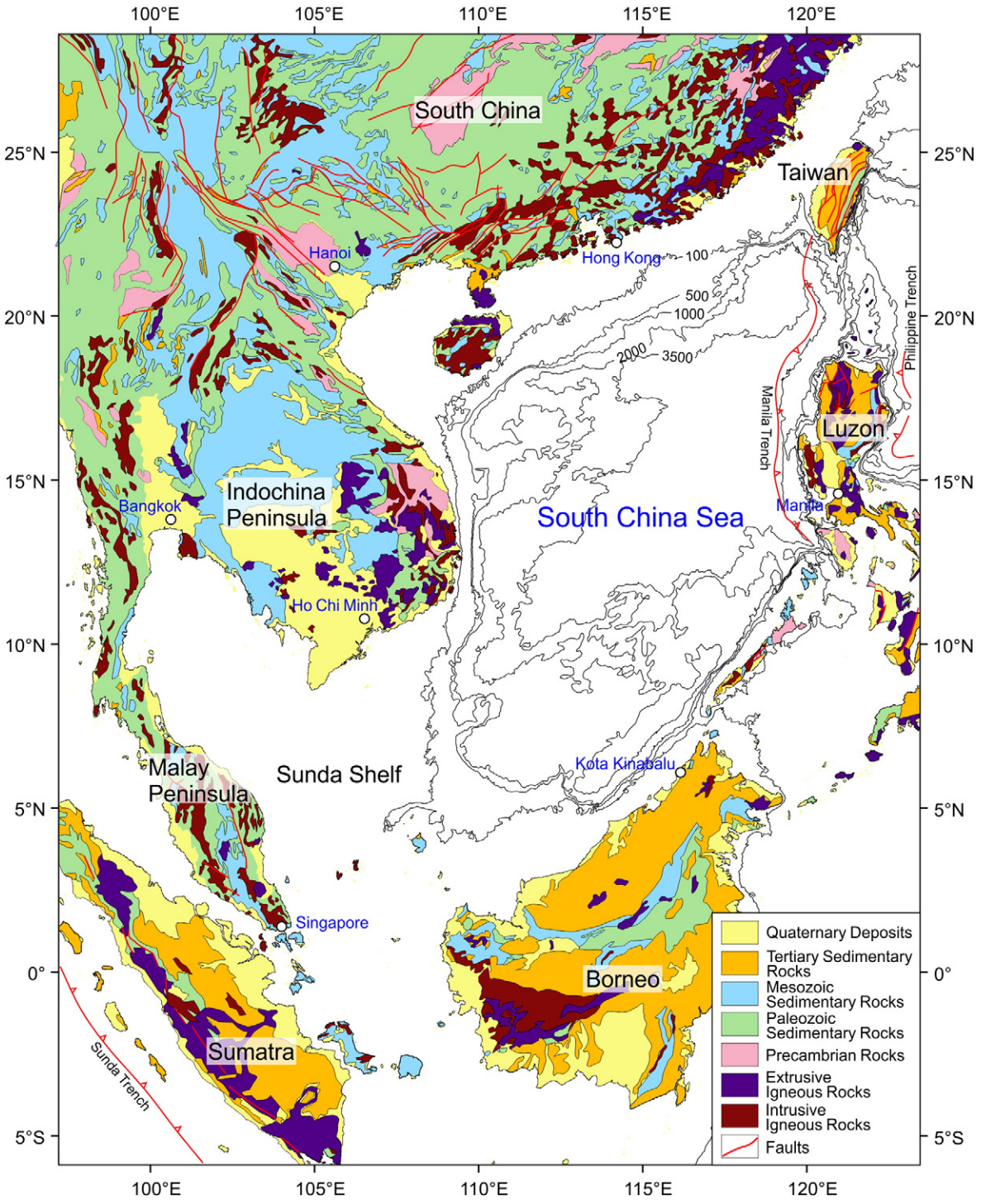

Fig. 2. Geological map of Southeast Asia surrounding the SCS.
Modified after Commission for the Geological Map of the World, 1975; major oceanic fault systems after Hall, 2002).

Geomorphic and tectonic investigations have revealed that the Red River fault system is active today (Leloup et al., 2001; Replumaz et al., 2001) with a minimum 5 mm/year long-term average slip rate since the Pliocene (Schoenbohm et al., 2004). Mesozoic sedimentary rocks (mainly sandstone and mudstone) prevail in the lowland of the southern Indochina Peninsula, in which several large Neogene basalt bodies outcrop.

In the south, the Malay Peninsula consists mainly of Paleozoic–Mesozoic granite and granodiorite and Paleozoic sedimentary rocks (Liu et al., 2012; Fig. 2), similar to the lithology of the eastern part of South China. Minor Mesozoic (mainly Jurassic–Cretaceous) sedimentary rocks and sparse basic volcanic rocks are also present. The sedimentary rocks mainly contain mudstone, sandstone, and limestone, interbedded with andesitic–rhyolitic volcanic rocks (Hutchison, 1968; Sultan and Shazili, 2009). Borneo is dominated by Tertiary sedimentary rocks, with a wide distribution of Paleozoic–Mesozoic sedimentary rocks in the central part and of Paleozoic–Mesozoic granite and granodiorite and Tertiary volcanic rocks in the southwestern part (Fig. 2). The sedimentary rocks are mainly sandy shale, partly interbedded with coals, sandstones, and carbonate rocks (Hutchison, 2005). Scattered

Tertiary basic volcanic rocks and Mesozoic basic–ultrabasic intrusive rocks are found only in central tectonic belts. Sumatra is covered mainly by Quaternary (largely Holocene) intermediate to basic volcanic rocks in the mountains and slopes of the southwest and by late Tertiary sedimentary rocks in the northwest (Liu et al., 2012; Fig. 2). Paleozoic–Mesozoic volcanic, intrusive, and sedimentary rocks and Tertiary basalts are also sparsely distributed. As part of the Sundaland, the Malay Peninsula has been tectonically stable since the Mesozoic (Hutchison, 1968). However, Borneo was tectonically active throughout the Cenozoic with the strongest tectonic uplift during the Oligocene–Miocene period (Hall, 2002; Hutchison, 2005). The magmatism with K–Ar ages of 6–10 Ma at Kinabalu (4218 m) in North Borneo, the highest mountain of Southeast Asia, confirms the rapid uplift during the late Miocene (Rangin et al., 1990). Sumatra has been highly tectonically active since the Tertiary, controlled by northeastward subduction of the Indian Ocean Plate along the Sunda Trench in the eastern Indian Ocean and the Sumatra strike-slip fault on the mountainous range of the southwestern island (Fig. 2; Barber and Crow, 2009). The wide distribution of Quaternary (largely Holocene) basic–intermediate volcanic rocks in the mountains and on the slopes shows the extremely active volcanic eruption history.

In the east, the Eurasian Plate and the Philippine Sea Plate are converging on Luzon across two major subduction zones, the east-dipping Manila Trench in the eastern SCS and the west-dipping Philippine Trench in the western Pacific Ocean (Fig. 2; Liu et al., 2009b). The island is thus characterized by active intra-arc strike slip faults, active volcanism, and high seismic activity. Cretaceous to Quaternary sedimentary and extrusive rocks and Cenozoic intermediate intrusive rocks abound throughout the island (Commission for the Geological Map of the World, 1975; Fig. 2). Pliocene–Quaternary volcanic deposits, mostly andesites and basalts with associated dacites and rhyodacites, mainly occur in southern Luzon. In contrast, Cretaceous–Paleogene undifferentiated strata, commonly mapped as volcanics, are distributed in most mountainous regions of Luzon. Cenozoic intermediate intrusive rocks are associated with the undifferentiated Cretaceous–Paleogene volcanic rocks. Palawan is very different from Luzon, consisting of two major tectonostratigraphic blocks. Northern Palawan is dominated by Jurassic olistostromes containing olistoliths of Permian limestone, Permian and Triassic chert, sandstone, and basaltic rocks, whereas southern Palawan is composed mainly of ophiolitic sequences that were thrust onto the island (Suzuki et al., 2000; Steuer et al., 2013). Northern Palawan is commonly assumed to have drifted from South China to the present position during the SCS spreading in the Oligocene to early Miocene (Hall, 2002).

2.2. Climatic conditions

The East Asian monsoon is the prevailing climate feature in the SCS and its surrounding region. Alternating summer and winter monsoon winds force seasonal precipitation and runoff regimes, which determine, in part, the soil and vegetation distribution (Webster, 1994; Wang et al., 2003). The winter monsoon is accompanied by continental cooling and the development of high pressure over northern Asia, resulting in northeast winds across the SCS (Fig. 3). In contrast, the summer monsoon is accompanied by continental heating, the development of low pressure over central China, and moderate southwesterly winds passing through the SCS. Nowadays, the strong winter monsoon lasts nearly six months (November to April), while the weaker summer monsoon lasts about four months (mid-May to mid-September) (Chu and Wang, 2003).

Driven by the seasonal monsoon winds, precipitation is largely reversed between the north and the south because of the shift of the inter-tropical convergence zone (ITCZ) (Wang et al., 2003). In the north, the annual rainfall amounts to 1700–2000 mm for South China and the Indochina Peninsula and 1900–2100 mm for Luzon, with nearly 85–90% of annual rainfall arriving during the summer monsoon season between May and September (Liu et al., 2007b, 2009b). In the south, annual rainfall is 2500–3000 mm for the Malay Peninsula, Sumatra, and Borneo. However, it is more evenly precipitated throughout the year with an increase of ~20% during the humid season (from November to February), when the winter monsoon affects the region (Liu et al., 2012). The north–south contrast of precipitation is attributed to the moisture that is mainly derived from the SCS.

In contrast to the strong dependence of precipitation on the regional monsoon climate, temperature distribution largely follows the latitudinal zonality of climate at the Earth's surface. In the subtropical zone, e.g., South China and the northern Indochina Peninsula, the annual temperature variation is strongly seasonal with the highest average value of ~20 °C in summer (July–August) and the lowest average value of 10 °C in winter (December–January) as a case at Guangzhou (Liu et al., 2007b). However, in the tropical zone, e.g., the Malay Peninsula, Sumatra, and Borneo, the annual average temperature is 27 °C with a seasonal difference of <2.5 °C at Kuantan (the Malay Peninsula) and <1.1 °C at Bandar Seri Begawan (Borneo) and Palembang (Sumatra) (Liu et al., 2012). In the middle SCS region between subtropical and tropical zones, e.g., Luzon and the southern Indochina Peninsula, the annual average temperature is stable at ~28 °C with a seasonal difference of ~5 °C at Manila (Luzon) and 4 °C at Ho Chi Minh City (the southern Indochina Peninsula) (Liu et al., 2007b, 2009b).

2.3. Oceanography

The general surface circulation in the SCS changes largely seasonally with monsoon winds and also has strong influence from the Kuroshio Current intrusion in the northern part (Shaw and Chao, 1994; Fang et al., 1998; Su, 2004) (Fig. 3). In winter, a basin-wide cyclonic gyre (NW Luzon Cyclonic Gyre) exists in the northern SCS with two cores, one located immediately to the northwest of Luzon (called NW Luzon Cyclonic Eddy) and the other located at about 17°N and 116°E (Fang et al., 1998). A series of mesoscale anticyclonic eddies distributed along the continental slope from the southwest of Taiwan to the west of the Dongsha Islands (called the Loop Current and SCS Branch of Kuroshio/SCS Warm Current) are suggested as the detachment of warm rings from the Kuroshio Current (Hu et al., 2000; Caruso et al., 2006; Yuan et al., 2006). The northeastward SCS Warm Current is a flow separated from the SCS Branch of Kuroshio Current. The coastal current mainly on the northern shelf (called the Guangdong Coastal Current) flows southwestward during the winter monsoon winds. In summer, the NW Luzon Cyclonic Gyre still exists in the northern SCS but is reduced and shifts eastward, whereas the NW Luzon Cyclonic Eddy stays at the approximately same location (Fang et al., 1998). The mesoscale anticyclonic SCS Branch of Kuroshio/SCS Warm Current eddies also shifts southeastward and the reversed Guangdong Coastal Current merges with the SCS Warm Current becoming the prevailing northeasterly surface current forced by the summer monsoon winds. Influenced probably by the NW Luzon Cyclonic Gyre, the coastal current west of Luzon (called the NW Luzon Coastal Current) flows to the north regardless of monsoon winds.

The intrusion of the Kuroshio Current can occur any time of the year but is a transient phenomenon, existing less than 30% of the time on average (Yuan et al., 2006). The dominant path of the Kuroshio Current intrusion in winter is a direct route from northeast of Luzon to southwest of Taiwan and then westward along the northern slope of the SCS, along the boundary between the NW Luzon Cyclonic Gyre/Eddy in the south and the SCS Branch of Kuroshio/Loop Current in the north (Fig. 3), whereas in summer, the flow shifts southward and becomes weak (Yuan et al., 2006). Although the Kuroshio Current intrusion may have different appearances as reported by various researchers, called a SCS branch of the Kuroshio, a loop current, a cyclonic eddy, or a seasonally reversing Guangdong coastal current (see review by Hu et al., 2000), the westward movement of mesoscale eddies originating

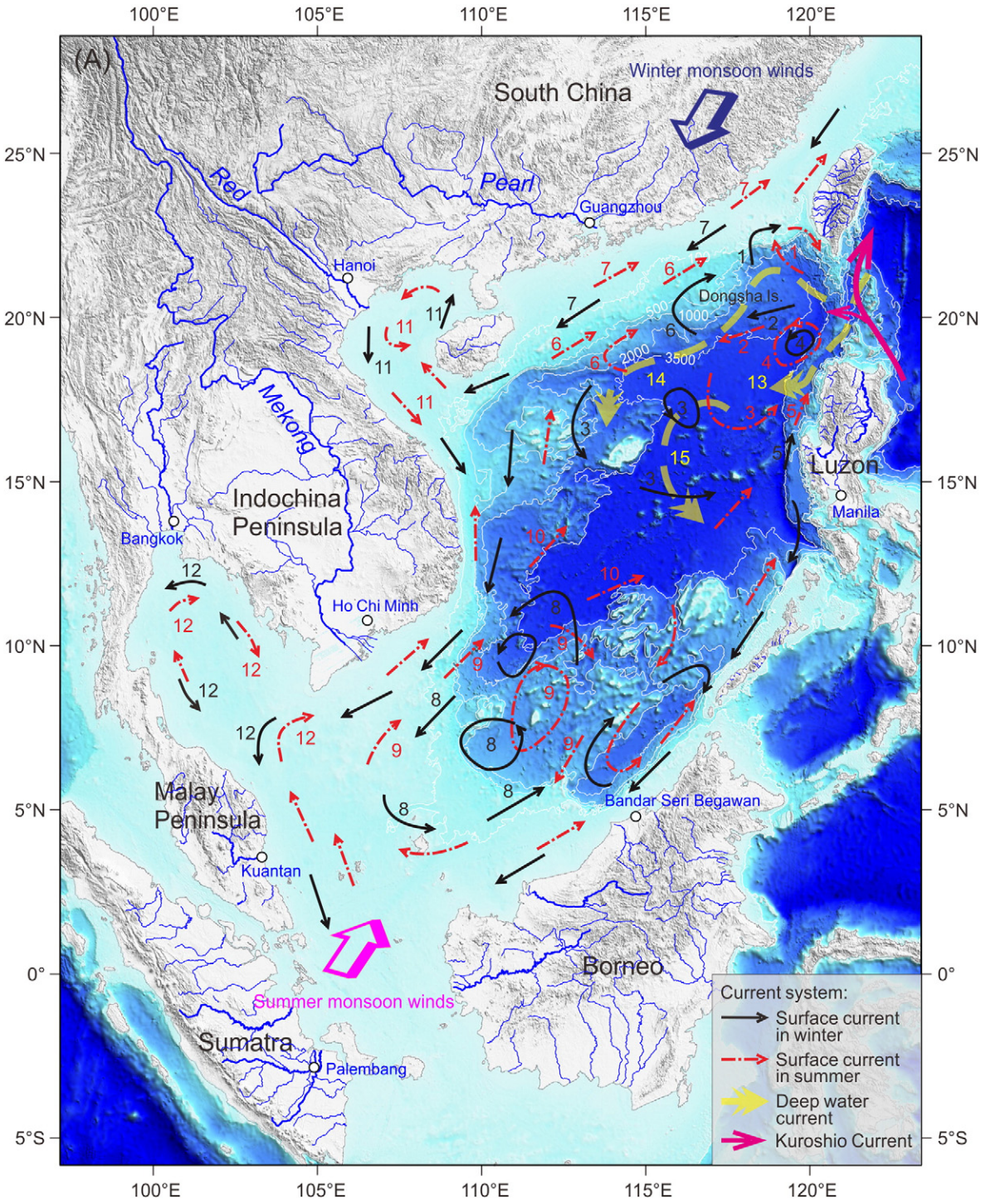

Fig. 3. Monsoon and current systems in the SCS. Monsoon winds after Webster (1994); major surface currents after Fang et al. (1998); Gulf of Tonkin surface currents after Xia et al. (2001) and Wu et al. (2008); Gulf of Thailand surface currents after Wattayakorn et al. (1998) and Tangang et al. (2011); Kuroshio Current after Caruso et al. (2006); deepwater currents deduced from Qu et al. (2006), Wang et al. (2011), and Zhao et al. (2014). Numbers for winter (black) and summer (red) surface currents: 1, Loop Current; 2, SCS Branch of Kuroshio; 3, NW Luzon Cyclonic Gyre; 4, NW Luzon Cyclonic Eddy; 5, NW Luzon Coastal Current; 6, SCS Warm Current; 7, Guangdong Coastal Current; 8, SCS Southern Cyclonic Gyre; 9, SCS Southern Anticyclonic Gyre; 10, SE Vietnam Offshore Current; 11, Gulf of Tonkin Surface Current; 12, Gulf of Thailand Surface Current. Numbers for deep currents: 13, Luzon Deep Current after Zhao et al. (2014); 14, SCS Contour Current deduced after Qu et al. (2006); 15, Deep Cyclonic Current after Wang et al. (2011).

from the Kuroshio Current intrusion is important for mass, heat, salt, and sediment transport in the northern SCS (Zhang et al., 2014).

Driven mainly by monsoon winds, the southern SCS is occupied by the SCS Southern Cyclonic Gyre in winter, which extends onto the northern Sunda Shelf (Fig. 3; Fang et al., 1998), and a weaker anticyclonic gyre can exist in the Palawan Trough region, southeast of the main gyre. In summer, the reversed SCS Southern Anticyclonic Gyre occupies a similar region, with a weaker cyclonic gyre in the southwest of Palawan. At the northern edge of SCS Southern Anticyclonic Gyre is a very strong offshore-directed jet called the SE Vietnam Offshore Current, which is located at a latitude of about 11°N. The central SCS circulation is governed largely by the interaction between the northern

and southern SCS current systems although it is not yet well understood.

Circulation in the Gulf of Tonkin was traditionally considered to follow seasonal monsoon winds with northeasterly winter wind forcing a gulf-wide cyclonic gyre, and southwesterly summer wind driving an anticyclonic circulation (Yu and Liu, 1993). However, recent measurement and simulation realized that the Qiongzhou Strait, with westward mean flow year-round, plays a key role in the cyclonic gyre in summer (Shi et al., 2002), resulting in cyclonic circulation in all seasons for the Gulf of Tonkin (Xia et al., 2001; Wu et al., 2008; Fig. 3). However, in the Gulf of Thailand, surface currents are driven mainly by seasonal monsoon winds anticyclonic in summer (March–August) and cyclonic in winter (September–November) despite weak currents throughout the area during January to February (Wattayakorn et al., 1998; Fig. 3). Numerical experiments reveal that the cyclonic circulation in winter and anticyclonic circulation in summer at the entrance region of the Gulf of Thailand could be understood as the extension of the SCS Southern Cyclonic Gyre and the SCS Southern Anticyclonic Gyre, respectively (Tangang et al., 2011; Fig. 3).

The Luzon Strait with a sill depth of about 2400 m is the only deep passage connecting the SCS with the western Pacific. Sediment transport by the deepwater flow from the Luzon Strait westward to the northern slope of the SCS has been deduced from previous studies (Lüdmann et al., 2005; Shao et al., 2007; Liu et al., 2010b). However, analysis of deep current systems in the SCS and their connection to the western Pacific was conducted only recently using numerical simulations with in situ mooring observations. Qu et al. (2006) reported the density field based on synthetic salinity data that shed some light on deep SCS circulation. They deduced that the deep water current (2000–2500 m) turns northwestward after entering the SCS through the Luzon Strait, and then turns southwestward along the continental margin off southeast China as the SCS Contour Current (Fig. 3). The existence of this deep layer circulation in the SCS is clearly seen in high-resolution general circulation models (Qu et al., 2004). In the deeper central SCS basin from 2400 m to the bottom, a cyclonic circulation forced by the Luzon overflow exists (Wang et al., 2011); this is called the Deep Cyclonic Current (Fig. 3). Recent in situ observation in the Luzon Strait revealed that deep Pacific water first flows into the Luzon Strait through the Bashi Channel and the Taltung Canyon, then turns southward along the Luzon Trough, and finally enters the SCS through two gaps on the southern Hengchun Ridge (Zhao et al., 2014; Fig. 3). The observed deep circulation helps to explain cross-basin sediment transport and sediment deposition in the final sink.

2.4. Fluvial sediment discharge

Numerous rivers including several of the world's largest rivers (e.g., the Pearl River, the Red River, and the Mekong River) and small mountainous rivers (e.g., rivers in southwestern Taiwan) supply as much as 700 Mt/year of observed suspended sediments to the SCS (Fig. 1, Table 1), representing 3.7% of estimated global fluvial sediment discharge to the world ocean (Milliman and Farnsworth, 2011). Field studies of northern Borneo and northeastern Sumatra are very limited or not available. However, models of river discharge suggest that their total fluvial sediment discharge to the SCS is as much as 957 Mt/year (Milliman et al., 1999; Fig. 1). Consequently, the total fluvial sediment discharge to the SCS is ~1600 Mt/year, amounting to 8.4% of annual sediment discharge to the global ocean (Milliman and Farnsworth, 2011), making the SCS the largest sink for fluvial sediments among enclosed or semi-enclosed marginal seas worldwide. All of the sediment delivery data considered in making these estimates are for pre-dam conditions and the values could have decreased owing to dam construction in recent decades (Saito et al., 2007; Kondolf et al., 2014).

Among these fluvial drainage systems, southwestern Taiwan represents the largest source of suspended sediment discharged directly to the SCS, with a total load of 176 Mt/year carried by rivers from the Cho-Shui River southward to the Lin-Pien River (Dadson et al., 2003; Table 1). Sediment loads from the Cho-Shui River and the Kao-Ping River (54.1 Mt/year and 49 Mt/year, respectively) are largest in Taiwan, although much of Cho-Shui River's sediment discharge is reported to move northward after draining into the Taiwan Strait (Liu et al., 2008a; Huh et al., 2011). South China contributes about 102 Mt/year of fluvial sediments to the SCS with a dominant sediment load of 84.3 Mt/year from the Pearl River, the 15th largest river in the world in terms of sediment discharge (Zhang et al., 2012).

The Indochina Peninsula in the western margin of the SCS contributes a huge amount of sediment to the system, primarily from the Red River in the north and the Mekong River in the south (Fig. 1, Table 1). In the northwestern corner, the total sediment discharge of 138 Mt/year to the Gulf of Tonkin is dominated by the sediment load from the Red River (130 Mt/year). Similarly, the total sediment discharge of 166 Mt/year from the remaining part of Vietnam's coast is dominated by the sediment load of the Mekong River (160 Mt/year) (Milliman and Syvitski, 1992). Although there are tens of small rivers draining into the SCS from middle Vietnam, they only contribute a few million tons to the sediment load in contrast to the small mountainous rivers of Taiwan (Table 1). Further to the west, several moderate rivers in middle Thailand supply more than 19 Mt/year of fluvial sediment into the Gulf of Thailand with the Chao Phraya being the largest contributor (11 Mt/year) (Fig. 1).

Further in the south, however, sediment discharge data are not available for most rivers draining the Malay Peninsula, Sumatra, and Borneo. Taking into consideration the extremely abundant rainfall, along with high topographic relief, the three mountainous geomorphic units could generate and contribute a large amount of sediment to the ocean. Milliman et al. (1999) employed the algorithms of Milliman and Syvitski (1992) to estimate the total sediment load of 910 Mt/year and 780 Mt/year for Borneo and Sumatra, respectively. Approximate 459 Mt/year from northern Borneo and 498 Mt/year from northeastern Sumatra drain directly into the SCS (Fig. 1). However, we are suspicious of such a huge sediment discharge because observed sediment loads from the two largest rivers in northern Borneo, the Rajang and the Baram, are reported to reach only 30 Mt/year and 12 Mt/year, respectively (Table 1). Sediment discharge from four major-moderate rivers in the northeastern Malay Peninsula amounts only to 35 Mt/year (Fig. 1; Liu et al., 2012). Therefore, more observations are required to better constrain the fluvial sediment discharge from this region.

In the east, small-moderate fluvial drainage systems are well developed in Luzon. With available sediment loads amounting to 13 Mt/year from three moderate rivers in western Luzon (Milliman and Syvitski, 1992; Liu et al., 2009b; Table 1), the total sediment discharge to the SCS was estimated to be 42 Mt/year (Liu and Stattegger, 2014).

3. Clay mineralogy and geochemistry of river-borne sediments

River-borne terrigenous sediments compose ~80% of total SCS surface sediments and average 63% of the total accumulated sediments since the opening of SCS in the early Oligocene (Huang, 2004; Huang and Wang, 2006). Other components of the sediments are mostly biogenic carbonate with negligible biogenic silicates and volcanic materials. Mineralogical assemblage and geochemical composition of these terrigenous sediments not only indicate the climatic conditions, tectonic activity, and specific lithological character from physical and chemical weathering processes on land (Liu et al., 2007b, 2009b, 2012), but also reflect the transport pathways in the sea, both of which are of critical importance for paleoenvironmental reconstruction (Clift et al., 2002, 2014; Li et al., 2003; Liu et al., 2003, 2004, 2010b; Shao et al., 2007, 2009; Wan et al., 2007, 2010). Clay minerals are typical weathering products on the Earth's surface best indicating various intensities and processes of chemical weathering, and they are easily semi-quantitatively

Table 1
Drainage area, runoff, and observed suspended sediment discharge of major rivers flowing directly into the South China Sea (SCS).

River name	Drainage area (10^3 km^2)	Runoff (mm/year)	Suspended sediment discharge (Mt/year)	Data source
Cho-Shui (Taiwan)	2.989	1200	54.1	Dadson et al. (2003)
Pei-Kang (Taiwan)	0.597	1300	2.2	Dadson et al. (2003)
Po-Tzu (Taiwan)	0.289	1400	2.1	Dadson et al. (2003)
Pa-Chang (Taiwan)	0.441	1500	6.3	Dadson et al. (2003)
Chi-Shui (Taiwan)	0.227	1300	1.8	Dadson et al. (2003)
Tseng-Wen (Taiwan)	1.157	1100	25.1	Dadson et al. (2003)
Yen-Shui (Taiwan)	0.146	1200	1.1	Dadson et al. (2003)
Erh-Jen (Taiwan)	0.175	1800	30.2	Dadson et al. (2003)
Kao-Ping (Taiwan)	3.076	2500	49	Dadson et al. (2003)
Tung-Kang (Taiwan)	0.175	2900	0.4	Dadson et al. (2003)
Lin-Pien (Taiwan)	0.31	2500	3.3	Dadson et al. (2003)
Total SW Taiwan			**176**	
Jiulongjiang (South China)	15	1000	3.1	Milliman and Farnsworth (2011)
Hanjiang (South China)	30	867	10	Milliman and Farnsworth (2011)
Pearl River (South China)	450	636	84.3	Zhang et al. (2012)
Moyangjiang (South China)	6.1	1393	0.8	Milliman and Farnsworth (2011)
Jianjiang (South China)	9.5	579	1.5	Milliman and Farnsworth (2011)
Nanliujiang (South China)	6.6	773	1.1	Milliman and Farnsworth (2011)
Changhuajiang (South China)	5.1	745	0.08	Milliman and Farnsworth (2011)
Nandujiang (South China)	6.6	773	1.1	Milliman and Farnsworth (2011)
Total South China			**102**	
Thai Binh (Indochina)	15	600	1	Milliman and Farnsworth (2011)
Red River (Indochina)	120	1000	130	Milliman and Syvitski (1992)
Ma (Indochina)	28	607	3	Milliman and Farnsworth (2011)
Nam San (Indochina)	11			Milliman and Farnsworth (2011)
Ca (Indochina)	27	815	4	Milliman and Farnsworth (2011)
Total N Indochina			**138**	
Thu-Bon (Indochina)	10	1400	2	Milliman and Farnsworth (2011)
Ba (Indochina)	14	643	1	Milliman and Farnsworth (2011)
Da Nhim (Indochina)	8			Milliman and Farnsworth (2011)
Sai Gon (Indochina)	44		3	Milliman and Farnsworth (2011)
Mekong (Indochina)	790	590	160	Milliman and Syvitski (1992)
Total S Indochina			**166**	
Bangpakhlong (Gulf Thai)	10	490		Milliman and Farnsworth (2011)
Khlong Phum Duang (Gulf Thai)	3	1133	0.12	Milliman and Farnsworth (2011)
Chao Phraya (Gulf Thai)	160	188	11	Milliman and Syvitski (1992)
Mae Klong (Gulf Thai)	31	419	8.1	Milliman and Farnsworth (2011)
Petch (Gulf Thai)	6	233		Milliman and Farnsworth (2011)
Total Upper Gulf of Thailand			**19**	
Pattani (Malay)	4	750	0.35	Milliman and Farnsworth (2011)
Kelantan (Malay)	12	1500	13.9	Liu et al. (2012)
Trengganu (Malay)	3.3	1970	0.8	Liu et al. (2012)
Pahang (Malay)	19	947	20.4	Liu et al. (2012)
Total NE Malay Peninsula			**35**	
Siak (Sumatra)	16			Milliman and Farnsworth (2011)
Kampar (Sumatra)	36	917		Milliman and Farnsworth (2011)
Inderagiri (Sumatra)	22	818		Milliman and Farnsworth (2011)
Hari (Sumatra)	50	920		Milliman and Farnsworth (2011)
Musi (Sumatra)	61	1311		Milliman and Farnsworth (2011)
Total NE Sumatra				
Tutong (Borneo)	2.3	1913	0.25	Milliman and Farnsworth (2011)
Baram (Borneo)	22.8	2500	12	Hiscott (2001)
Kidurong (Borneo)	5.4			Milliman and Farnsworth (2011)
Rajang (Borneo)	50	2270	30	Staub et al. (2000)
Lupar (Borneo)	7			Milliman and Farnsworth (2011)
Sambas (Borneo)	6.8			Milliman and Farnsworth (2011)
Landek (Borneo)	10			Milliman and Farnsworth (2011)
Kapuas (Borneo)	82	1220		Milliman and Farnsworth (2011)
Pawan (Borneo)	13	2923		Milliman and Farnsworth (2011)
Total N Borneo			**42**	
Cagayan (Luzon)	30.4	1542		Liu et al. (2009b)
Vigan (Luzon)	5.2	2104		Liu et al. (2009b)
Agno (Luzon)	6.3	1050	4.7	Liu et al. (2009b)
Pampanga (Luzon)	8.6	880	3.5	Liu et al. (2009b)
Angat (Luzon)	0.57		4.6	Milliman and Syvitski (1992)
Total Luzon			**13**	

identified in forms of mineralogical particles (Holtzapffel, 1985; Chamley, 1989), allowing the quantitative evaluation of fluvial sediment transport process, and therefore are key for the source-to-sink study of fluvial sediments in the SCS (Liu et al., 2008b, 2010b).

In this chapter, we synthesize recently available clay mineralogical and geochemical data of surface samples throughout the SCS seafloor and surrounding drainage systems to present their distribution characteristics and to investigate how the fluvial sediments are produced through chemical weathering. Total 1135 surface or core top samples from the seafloor and 370 surface samples from all 180 river systems surrounding the SCS are combined together to present the basin-wide distribution of clay mineralogical compositions (Fig. 4). Major-element

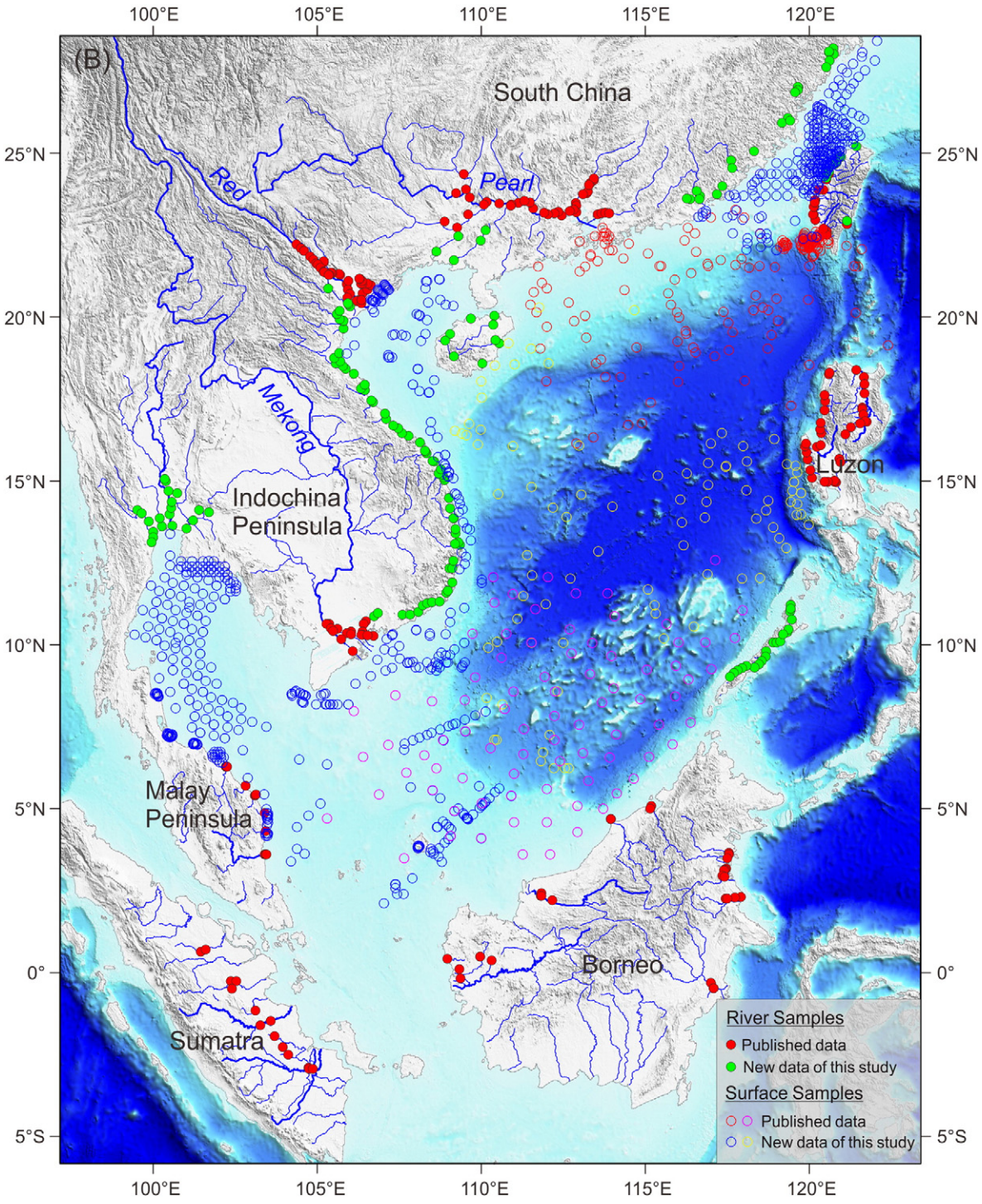

Fig. 4. Locations of surface samples from the seafloor and surrounding rivers used in this study. Published data of river samples: the Pearl, Red, and Mekong rivers from Liu et al. (2007b); Taiwan rivers from Liu et al. (2008b, 2010b); Luzon rivers from Liu et al. (2009b); the Malay Peninsula and Sumatra rivers from Liu et al. (2012); Borneo rivers from Liu et al. (2007c, 2012). Published data of seafloor surface samples: northern SCS (red circles) from Liu et al. (2007a, 2008b, 2010b); southern SCS (purple circles) from Liu et al. (2010a).

geochemistry on both bulk and clay-fraction particles of surface samples from major fluvial systems are included to demonstrate various intensities and processes of chemical weathering, which are strongly related to regional climatic and tectonic controls. Nd and Sr isotopes of part of these samples help to better constrain fluvial sediment provenances in the SCS. Of the seafloor surface samples, clay mineralogy of 216 samples from the northern SCS and 83 samples from the southern SCS were previously published (Liu et al., 2007a, 2008b, 2010b; Liu et al., 2010a), and 836 samples are presented here for the first time. These new seafloor samples are located mainly in the Taiwan Strait (266 samples, Huh et al., 2011), the Gulf of Tonkin (62 samples, Wiesner et al., 2012), the Gulf of Thailand (202 samples), and the southwestern SCS (~160 samples, Stattegger et al., 1997; Wiesner et al., 1999, 2006) (Fig. 4). Of the river surface samples, clay mineralogy and major-element geochemistry of 227 river samples from Taiwan, Luzon, South China (Pearl River), the Indochina Peninsula (Red and Mekong rivers), the Malay

Peninsula, Sumatra, and Borneo were reported previously (Liu et al., 2007b, 2007c, 2008b, 2009b, 2010b, 2012); 143 new samples were collected in East China (Zhejiang), South China (Fujian, Guangxi, and Hainan), middle Vietnam (all coastal rivers through south to north), middle Thailand, and Palawan (Fig. 4). Nd and Sr isotopic compositions of 47 seafloor surface samples and 53 river samples are mostly based on the literature (Goldstein and Jacobsen, 1988; Li et al., 2003; Liu et al., 2007b; Shao et al., 2009; Wei et al., 2012). Among them, Nd isotopes of 14 river samples from Taiwan, Luzon, and Borneo represent new data. All data sources and GPS (Global Position System) locations of these samples can be found in the Supplementary data Tables S1 and S2.

3.1. Analytical methods

Laboratory analysis of clay mineralogy, major elements, and Nd isotopic geochemistry of these new samples followed the analytical methods of previously published data (Liu et al., 2007b, 2008b, 2009b, 2010b, 2012), which are briefly summarized here. Clay minerals were identified by X-ray diffraction (XRD) using a PANalytical diffractometer at the State Key Laboratory of Marine Geology, Tongji University (Shanghai). Three XRD runs were performed on oriented mounts of non-calcareous clay-sized (<2 μm) particles, following pretreatment conditions of air-drying, ethylene–glycol solvation for 24 h, and heating at 490 °C for 2 h (Holtzapffel, 1985). Identification of clay minerals was made mainly according to the position of the (001) series of basal reflections on the three XRD diagrams. Semi-quantitative estimates of peak areas of the basal reflections for the main clay mineral groups of smectite (including mixed-layers) (15–17 Å), illite (10 Å), and kaolinite/chlorite (7 Å) were carried out on the glycolated curve using the MacDiff software (Petschick, 2000). Following the laboratory routine, the weighting factors introduced by Biscaye (1965) or Holtzapffel (1985) were not used when generating relative weight percentages of each clay mineral. Replicate analyses of selected samples gave a precision of ±2% (2σ), and the semi-quantitative evaluation of each clay mineral has an accuracy of ~5%. Clay mineralogical data of Liu et al. (2010a) in the southern SCS were obtained on a D8 Advance diffractometer with the weighting factors of Biscaye (1965), and therefore they were re-calculated using the method of this study to keep consistency in the data for comparison.

Major elements were measured on both carbonate-free bulk (<63 μm) and clay-fraction (<2 μm) samples using an IRIS Advantage inductively coupled plasma-optical emission (ICP-OES) at the State Key Laboratory of Marine Geology, Tongji University (Shanghai) (Liu et al., 2009b, 2012). Particles <63 μm were wet sieved to remove potential local coarse grains that may significantly change the general geochemical composition. Organic matter and carbonate were then removed using 10% H_2O_2 and 0.5% HCl, respectively, in order to obtain pure terrigenous silicate particles. About 30–40 mg of prepared bulk and clay-fraction sediments was heated under 600 °C to obtain the loss of ignition (LOI), and then was dissolved using a mixture solution of HNO_3 and HF on a hot plate. The eluted sample was diluted with 2% HNO_3 for the major element measurement. Replicate analyses (N = 20) of GSR-5, GSR-6, and GSD-9 standards during the study gave an accuracy of 4% for major elements. Replicate analyses of selected samples gave a precision of ±2% (2σ) for bulk particles and ±1% (2σ) for clay fractions.

Nd isotopic composition of river samples was analyzed on bulk (<63 μm) carbonate- and organic-free sediments using a Thermo Scientific Multi-Collector Induced Coupled Plasma Mass Spectrometer (MC-ICPMS NEPTUNE^{Plus}) at the Laboratoire des Sciences du Climat et de l'Environnement (LSCE) in Gif-sur-Yvette following the procedure described by Colin et al. (1999). In brief, decarbonated and organic-free samples were dissolved in HF-$HClO_4$ and HNO_3–HCl mixtures. Rare earth elements (REEs) were then purified using a cationic resin (AG50W-X8). Nd was extracted and purified using an Ln-Spec column following Copard et al. (2010). The Nd isotopic composition was analyzed at a concentration of 15 ppb. $^{143}Nd/^{144}Nd$ ratios were corrected for mass fractionation relative to $^{146}Nd/^{144}Nd = 0.7219$ applying an exponential fractionation correction. During the analysis, every three samples were bracketed with analyses of standard solutions from La Jolla at similar Nd concentrations to those of the samples. Replicate analyses of the La Jolla standard (n = 61) yielded a mean $^{143}Nd/^{144}Nd$ of 0.511854 ± 0.000012, which is comparable to its certified value of 0.511860 ± 0.000020. Nd results are expressed as $\varepsilon Nd(0) = [((^{143}Nd/^{144}Nd_{meas}) / 0.512638) - 1] \times 1000$, using the chondritic uniform reservoir (CHUR) value given by Jacobsen and Wasserburg (1980).

3.2. Clay mineralogical composition in surrounding fluvial systems

The clay mineral assemblages in surrounding fluvial systems are similar within each drainage system or region defined as province or sub-province, but largely different between provinces. Therefore, we group the clay mineral components in each province or sub-province (Table 2) and present them as average mineral assemblages indicated by pie charts in Fig. 5.

Table 2
Average clay mineral assemblages of various provinces and sub-provinces in fluvial drainage systems surrounding the SCS with minimum and maximum values in brackets. Regions in bold show their drainage systems with significant fluvial sediment discharge to the SCS.

Region	Province	Sample number	Smectite (%)	Illite (%)	Kaolinite (%)	Chlorite (%)
Taiwan	**a**	**38**	**4 (0–10)**	**56 (48–66)**	**4 (0–10)**	**36 (29–42)**
East China (Zhejiang)	b	17	23 (19–30)	37 (30–42)	16 (12–23)	24 (21–30)
South China (Fujian)	c1	13	1 (0–3)	16 (13–20)	70 (62–78)	13 (10–19)
South China (Pearl River)	**c2**	**36**	**1 (0–4)**	**35 (21–51)**	**46 (34–65)**	**18 (10–23)**
South China (Guangxi)	c3	5	2 (1–4)	17 (12–22)	65 (55–72)	16 (10–21)
South China (Hainan)	c4	9	6 (0–11)	12 (7–16)	76 (62–84)	6 (4–7)
Indochina (Red River)	**d1**	**43**	**7 (2–19)**	**44 (31–58)**	**26 (19–33)**	**23 (19–27)**
Indochina (North Vietnam)	d2	24	3 (0–7)	37 (24–51)	43 (28–58)	17 (13–23)
Indochina (Middle Vietnam)	d3	16	1 (0–4)	9 (5–13)	77 (64–85)	13 (4–21)
Indochina (South Vietnam)	d4	19	28 (8–52)	13 (5–19)	53 (33–67)	6 (0–13)
Indochina (Mekong River)	**d5**	**17**	**9 (4–15)**	**37 (33–42)**	**31 (27–32)**	**23 (20–28)**
Thailand	**e**	**20**	**42 (23–58)**	**17 (6–27)**	**32 (24–40)**	**9 (3–20)**
Malay Peninsula	**f**	**12**	**1 (0–1)**	**17 (11–25)**	**78 (71–84)**	**4 (2–9)**
Sumatra	**g**	**14**	**19 (8–26)**	**8 (4–15)**	**57 (50–68)**	**16 (11–21)**
Borneo (North Borneo)	**h1**	**19**	**1 (0–4)**	**56 (44–75)**	**18 (12–24)**	**25 (12–31)**
Borneo (West Borneo)	h2	6	14 (10–14)	13 (12–21)	47 (46–58)	26 (25–32)
Borneo (East Borneo)	h3	7	9 (6–13)	22 (18–26)	42 (35–50)	27 (21–29)
Palawan (South Palawan)	i1	10	54 (14–93)	21 (0–32)	5 (1–10)	20 (8–32)
Palawan (North Palawan)	i2	10	0 (0–2)	42 (38–53)	33 (23–35)	25 (18–31)
Luzon	**j**	**35**	**87 (76–95)**	**1 (0–3)**	**5 (1–11)**	**7 (2–12)**

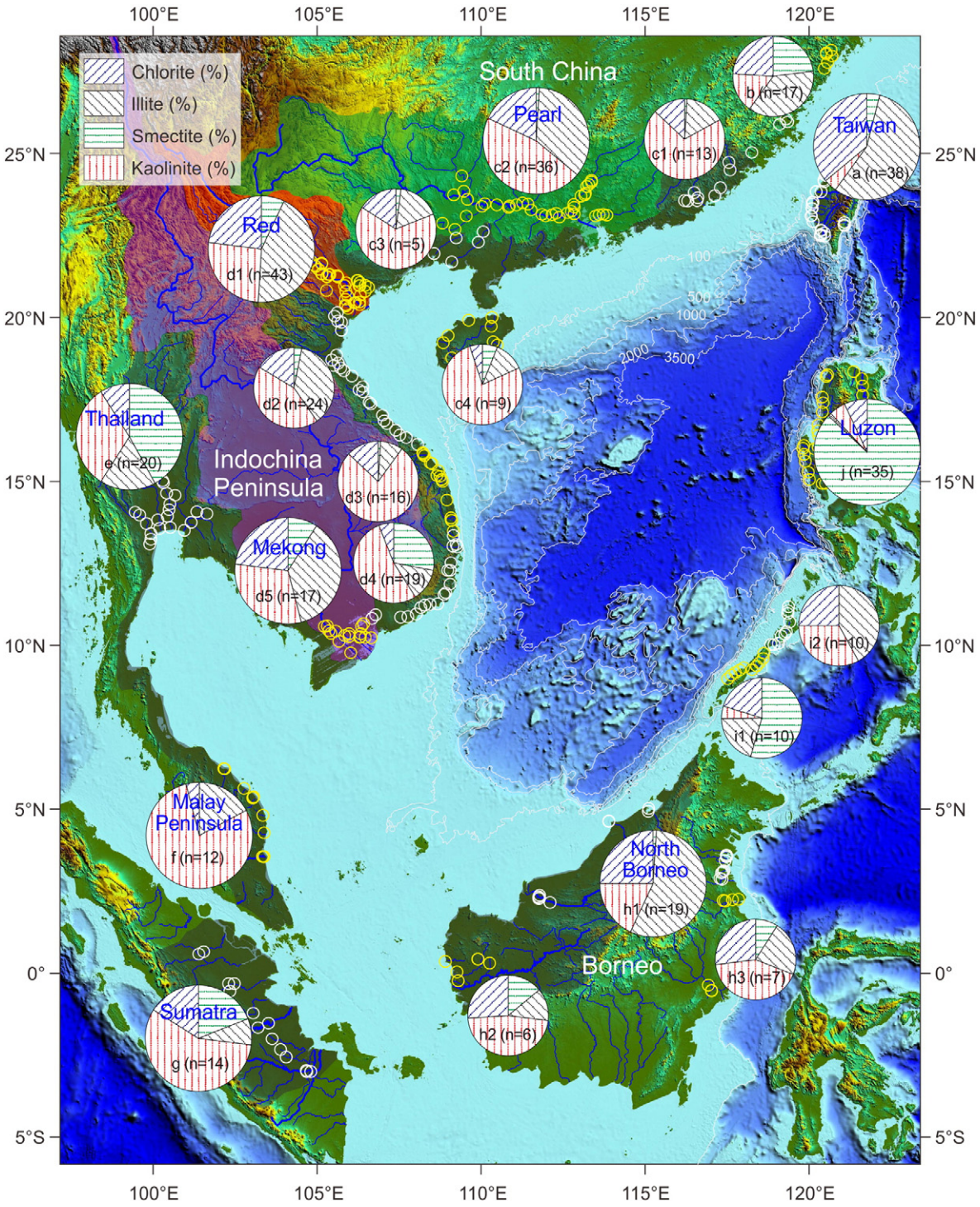

Fig. 5. Distribution of average clay mineral assemblages for surface samples (represented by pie charts) in all fluvial drainage systems surrounding the SCS. The calculated average data are listed in Table 2. Locations of river samples in different provinces or sub-provinces are distinguished by different colors (yellow or white). Relatively larger sizes of pie charts indicate significant fluvial sediment discharge from nine major drainage systems. N = number of surface samples. Refer to the caption of Fig. 4 for sources of published data.

3.2.1. Average clay mineralogical composition in fluvial sediments

Taiwan (Province a) sediments from all 17 small to moderate rivers in the western and southern island consist dominantly of illite (56%) and chlorite (36%), with scarce amounts of smectite (4%) and kaolinite (4%) (Fig. 5, Table 2) (Liu et al., 2008b, 2010b). The smectite and kaolinite contents are minimal in most southwestern rivers, such as the Kao-Ping River, with listed percentages <3% (Supplementary data Table S1). The majority of illite and chlorite implies a strong physical weathering of exposed Tertiary sedimentary rocks under rapid uplift activities since the Pliocene. Taiwan becomes an end-member of characteristic illite and chlorite assemblage for fluvial sediment provenances in the northern SCS (Liu et al., 2008b).

South China has ~20 moderate to major rivers flowing directly into the SCS extending from Fujian in the east, draining into the Taiwan Strait, to Guangxi and Hainan in the west, draining into the SCS, with the Pearl River having the dominant drainage area and suspended

sediment discharge (Table 1). A total of 36 surface samples distributed in the eastern, northern, and western Pearl River (Sub-Province c2) consist mainly of kaolinite (46%), illite (35%), and chlorite (18%) with scarce amount of smectite (1%) (Fig. 5, Table 2) (Liu et al., 2007b). The clay mineral assemblage from different river sections generally varies within the range of 10% (Supplementary data Table S1), but at some locations in the eastern and northern parts of the river, kaolinite can reach as high as 64–78% (e.g., PR05), whereas at a location in the western part, illite reaches 61% (e.g., PR41-1). Similarly, small-moderate river sediments in Fujian (Sub-Province c1), Guangxi (Sub-Province c3), and Hainan (Sub-Province c4) regions in South China all contain high kaolinite contents, averaging up to 65–76%, with a few locations of 84%; their illite and chlorite contents are in ranges of 12–16% and 6–16%, respectively, and smectite content is scarce (<6%). The dominant kaolinite content throughout the South China drainage systems suggests an intensive chemical weathering of exposed rocks including granites in the east and sedimentary rocks across the entire basin (Liu et al., 2007b). For comparison, the clay mineralogy of river samples in East China is presented here although these rivers directly flow into the East China Sea. A total of 17 surface samples from 12 small-moderate rivers in Zhejiang of East China (Province b) contain moderate amounts of all four clay mineral species: smectite (23%), illite (37), kaolinite (16%), and chlorite (24%) (Fig. 5, Table 2), and they are quite different from neighboring rivers in South China and Taiwan.

The Indochina Peninsula has more than 50 small to major rivers flowing into the SCS. Sediments in Red River and Mekong River drainage systems (Sub-Provinces d1 and d5, respectively) contain dominant illite (averagely 44% and 37%, respectively) and less abundant chlorite (both at 23%) and kaolinite (26% and 31%, respectively); smectite (7% and 9%, respectively) is a minor component (Fig. 5, Table 2) (Liu et al., 2007b). Relatively high content of illite reflects decreased hydrolytic processes in continental weathering and increased direct rock erosion under cold and arid climatic conditions. Both the Red and Mekong rivers drain the high relief of the eastern Tibetan Plateau and its marginal regions, showing significantly increased physical erosion, with higher erosion in the Red River drainage basin as indicated by its higher illite content (Liu et al., 2007b). Most other small rivers in Vietnam provide kaolinite as the predominant component with significant variations of illite and smectite contents, and we divide them into three Sub-Provinces: North Vietnam (Sub-Province d2), Middle Vietnam (Sub-Province d3), and South Vietnam (Sub-Province d4) (Fig. 5). River sediments in North Vietnam consist mainly of kaolinite (43%) and illite (37%), with less abundant chlorite (17%) and very scarce smectite (3%). In Middle Vietnam, kaolinite (77%) is strongly dominant, with minor amounts of chlorite (13%), illite (9%), and scarce smectite (1%). In South Vietnam, kaolinite (53%) is still dominant, but with relatively high content of smectite (28%) and minor amounts of illite (13%) and chlorite (6%). The high content of kaolinite in these small Vietnamese rivers shows locally intensive chemical weathering, which is similar to Hainan and Guangxi of western South China (Fig. 5).

In Middle Thailand (Province e), four moderate rivers drain the western Indochina Peninsula and then flow into the upper part of Gulf of Thailand. 20 samples from these rivers contain very high smectite content (42%) and less abundant kaolinite (32%), with minor amounts of illite (17%) and chlorite (9%) (Fig. 5, Table 2). The highest content of smectite reaches 68% at a sample in the Petch River in western Thailand (Supplementary data Table S1). The high contents of smectite and kaolinite reflect strong chemical weathering and the basaltic lithology of these drainage systems.

In the Malay Peninsula (Province f), 12 samples collected from 6 small rivers are dominated by kaolinite (78%) with minor amounts of illite (17%) and scarce chlorite (4%) and smectite (1%) (Fig. 5, Table 2) (Liu et al., 2012). Similarly, in Sumatra (Province g), a total of 14 surface samples collected from 7 small to moderate rivers contain predominantly kaolinite (57%), with minor amounts of smectite (19%), chlorite (16%), and illite (8%) (Fig. 5, Table 2) (Liu et al., 2012). Such high content of kaolinite in both the Malay Peninsula and Sumatra reflects intensive chemical weathering of the tropical climate regardless of the lithological and tectonic setting. The Malay Peninsula with the highest content of kaolinite and almost no smectite stands for an end-member of clay mineralogy for fluvial sediment provenances in the southern SCS.

Borneo displays dramatic variation in the clay mineral assemblage of surface sediments. North Borneo (Sub-Province h1) sediments (19 samples collected from 6 small to moderate rivers) consist dominantly of illite (56%), with less abundant chlorite (25%), kaolinite (18%), and very scarce smectite (1%) (Fig. 5, Table 2) (Liu et al., 2007c, 2012). On the contrary, in West Borneo (Sub-Province h2) and East Borneo (Sub-Province h3), kaolinite is dominant in the clay mineral assemblages with averages of 47% and 42%, respectively; illite becomes less abundant (13% and 22%, respectively); chlorite (21–32% for both regions) and smectite (6–14% for both regions) are also less abundant (Fig. 5, Table 2) (Liu et al., 2012). Similarly to the Malay Peninsula and Sumatra, the high content of kaolinite in West and East Borneo indicates intensive chemical weathering. However, the high content of illite and moderate content of chlorite in North Borneo likely result from the active tectonic setting especially the rapid uplift of northeastern Borneo, which strongly intensifies the physical erosion of parent rocks (Liu et al., 2012).

Palawan, although small, consists of two very different blocks with distinguished lithological settings, which produce two different clay mineralogical provinces. North Palawan (Sub-Province i2) sediments from 10 tiny rivers contain dominant illite (42%) and kaolinite (33%), with less abundant chlorite (25%) and almost no smectite (Fig. 5, Table 2). On the contrary, South Palawan (Sub-Province i1) sediments also from 10 tiny rivers contain dominant smectite (54%), with less abundant illite (21%), chlorite (20%), and scarce kaolinite (5%). The clay mineral assemblage in fluvial sediments of North Palawan is similar to that of the Pearl River, with both containing high kaolinite and almost no smectite. This correlation fits well the tectonic assumption that the North Palawan block drifted away from South China during the SCS seafloor spreading (Hall, 2002). Instead, South Palawan with the dominant lithology of an ophiolitic sequence is easily weathered to form smectite.

Luzon (Province j) presents a dominance of smectite (87%) with minor chlorite (7%), kaolinite (5%), and scarce illite (1%) in the clay mineral assemblage of 35 samples collected from 21 small to moderate rivers (Fig. 5, Table 2) (Liu et al., 2009b). The clay distribution displays an island-wide consistency (Supplementary data Table S1). The majority of andesitic – basaltic volcanic and sedimentary rocks along with the tectonically active geological setting and subtropical East Asian monsoon climate are responsible for the predominance of smectite (Liu et al., 2009b). Such high content of smectite in Luzon makes the island an end-member of clay mineralogy for fluvial sediment provenances in the eastern SCS.

3.2.2. Forcing mechanism of chemical weathering on surrounding land areas

The distribution of clay mineral assemblage in sediments of surrounding fluvial systems shows four significant features (Figs. 5 and 6A): (1) high kaolinite content (generally close to or much larger than 50%) in South China, most parts of Vietnam, the Malay Peninsula, Sumatra, and West and East Borneo, with extremely high values in the Malay Peninsula (averagely 78%); (2) high illite and chlorite contents (together larger than 80%) in Taiwan and North Borneo with the highest values (up to 98%) in Taiwan; (3) high smectite content (average 87%) in Luzon with the highest value up to 97% in the western part of island; (4) moderate contents of all four clay mineral species in the Red River, the Mekong River, and Middle Thailand with relatively higher illite content in the Red and Mekong river systems and higher smectite content in the Middle Thailand drainage systems. The features in clay mineral distribution are related to the intensity of chemical weathering,

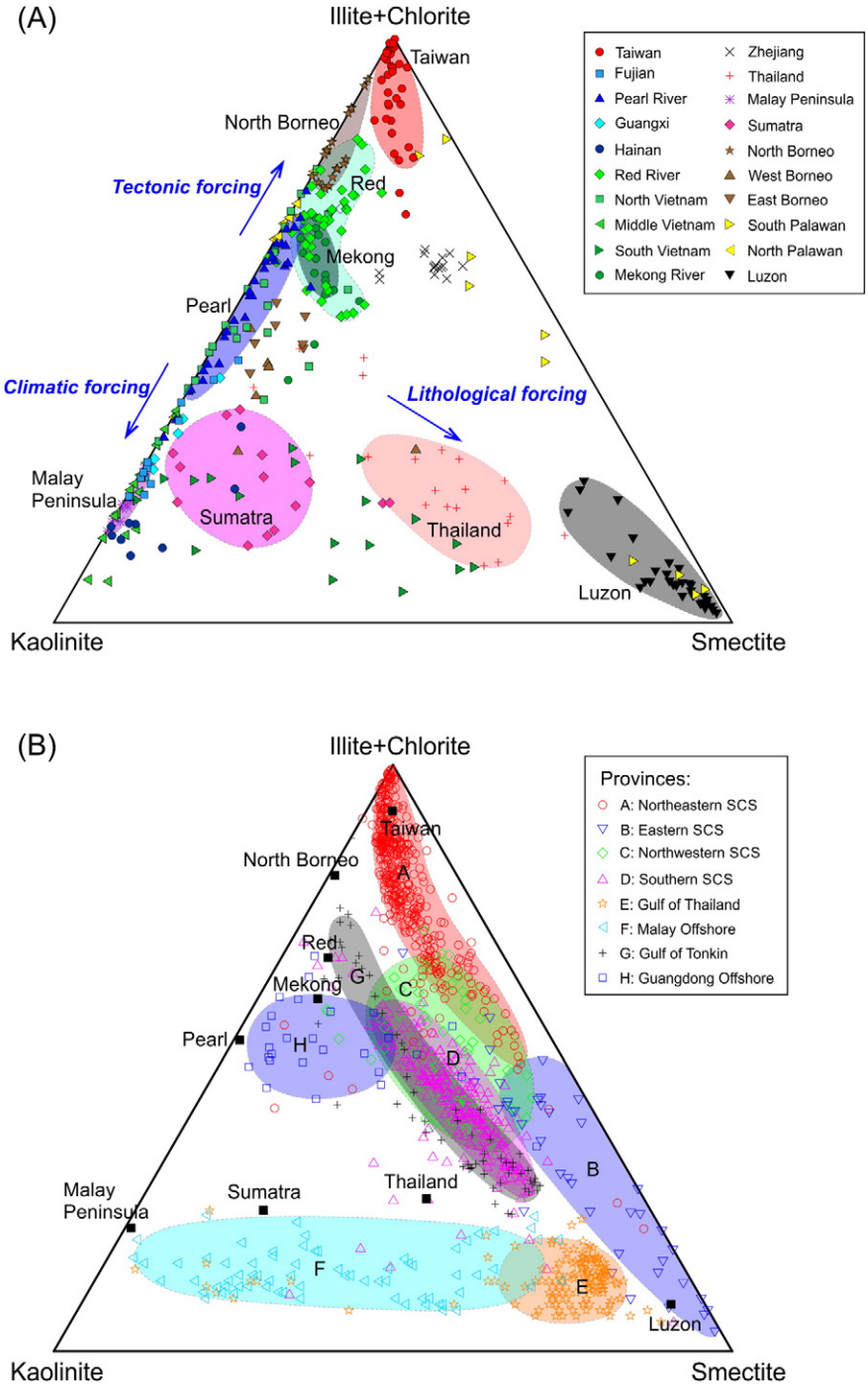

Fig. 6. Ternary diagram of the major clay mineral groups illite + chlorite, kaolinite, and smectite. (A) Fluvial surface samples. Areas defined by different shades of color show nine major drainage systems with significant fluvial sediment discharge. The principal forcing processes on clay mineral formation are also indicated. (B) Seafloor surface samples. Shaded areas show eight provinces (A–H) of clay mineral assemblages distributed in surface samples. Refer to the caption of Fig. 4 for sources of published data.

which is generally controlled by climatic conditions and geological settings.

Kaolinite is usually formed by monosialitization (both mobile and transitional elements tend to be expelled) of parent rocks, representing the intensive chemical weathering (hydrolysis) under warm and humid climate (Chamley, 1989). Kaolinite is widely distributed in the fluvial systems surrounding the SCS, with very high contents generally close to or much larger than 50% in South China, most parts of Vietnam, the Malay Peninsula, Sumatra, and West and East Borneo; relatively less abundant kaolinite (larger than 25%) also exists widely in the Red River, the Mekong River, Middle Thailand, and North Palawan (Fig. 5). In some regions, kaolinite contents are extremely high with values larger than 70% such as in the Malay Peninsula, Hainan and Fujian in South China, and a few locations in Middle Vietnam. Under warm and humid East Asian monsoon climate conditions, parent rocks enriched in alkali and alkaline elements (e.g., granite, granodiorite, and intermediate-acid volcanic rocks) such as in the Malay Peninsula and South China are easily and intensively weathered to form kaolinite. Furthermore, stable tectonics since the Mesozoic in these two regions allow sufficient time and climatic conditions for monosialitization

processes to occur. However, the majority of Quaternary intermediate-basic volcanic rocks and Upper Tertiary sedimentary rocks in Sumatra also have very high kaolinite content (average 57%) (Fig. 5) although the lithology and tectonic settings are completely different from those of the Malay Peninsula and South China. Such results suggest that the monsoon climate with warm temperature and high precipitation greatly contributes to the extremely strengthened chemical weathering on the intermediate-basic volcanic and sedimentary rocks in Sumatra (Liu et al., 2012). Therefore, the significantly high content of kaolinite indicates overwhelming climatic forcing on the chemical weathering occurring in the fluvial drainage systems surrounding the SCS (Fig. 6A).

Illite and chlorite are primary minerals and they are formed through weak hydrolysis and/or strong physical erosion of bedrocks. Illite and chlorite, generally higher than 80% together, prevail in the clay assemblage of Taiwan and North Borneo, with extremely high values (up to 98%) occurring in Taiwan (Fig. 5). They are abundant also in the Red and Mekong river systems. Active tectonic settings in Taiwan and North Borneo, especially the rapid uplift since late Miocene in Taiwan (Huang et al., 1997) and during Oligocene–Miocene in North Borneo (Hutchison, 2005), have resulted in extremely strong physical erosion of parent rocks. Along with lithological features of the major Mesozoic–Cenozoic sedimentary rocks, i.e., absence of intermediate-acid rocks that are essential to produce a large amount of kaolinite, the intense seasonal precipitation accelerates physical erosion to form clay mineral assemblages with a majority of illite and chlorite in Taiwan and North Borneo. Such clay mineral assemblages also develop on the high relief of the eastern Tibetan Plateau and the Indochina Peninsula, providing high contents of illite and chlorite to the Red and Mekong river drainage systems. The general linear correlation between illite and chlorite in all surface samples in the surrounding drainage systems confirms that they are two analogous minerals resulting from similar physical erosion of bedrocks (Fig. 7A) (Liu et al., 2010b). Therefore, illite and chlorite represent active tectonics and precipitation-caused physical erosion (Fig. 6A).

Smectite usually results from bisialitization (subtraction of mobile ions from minerals) and indicates the secondary product of chemical weathering of ferromagnesian aluminosilicates (Liu et al., 2009b). Under hot and humid climate conditions, weathering is prone to be accelerated on volcanic rocks. The rapidity of volcanic rock weathering often leads to a dramatic abundance of smectite that forms easily on andesitic–basaltic materials. The majority of Quaternary (mainly Holocene) intermediate-basic volcanic rocks in Sumatra are potential parent rocks for the large production of smectite through the bisialitization process. Unlike the dominant occurrence of smectite in Luzon, however, the smectite content in Sumatra is only moderate with an average of 19%. Moderate smectite and dominant kaolinite in Sumatra suggest efficient bisialitization reactions followed by well-developed monosialitization. We do not think topographic profiles with various slope types in drainage basins of Sumatra could affect the chemical weathering of smectite toward kaolinite, because all investigated samples collected from various topographic locations have similar results with dominant kaolinite, confirming that the tropical climate is the primary forcing factor. Therefore, smectite in Luzon and Middle Thailand reflects strong lithological (intermediate-basic volcanic) forcing on the chemical weathering in subtropical regions (Fig. 6A).

3.3. Clay mineralogical composition of seafloor surface sediments

The densely distributed surface or core top samples from the seafloor allow us to investigate the basin-wide clay mineralogical distribution, which is highly related to fluvial sources and transport processes. The clay mineral assemblage on the seafloor throughout the SCS demonstrates characteristic patterns for all four clay mineral species (Fig. 8). The patterns are very different from our knowledge obtained previously on low-resolution studies (Chen, 1978; Liu et al., 2003; Liu et al., 2010a).

3.3.1. Spatial distribution of clay mineral assemblages on the seafloor

Smectite and illite are two dominant clay minerals in seafloor surface sediments with average contents of 34% and 32%, respectively. Two areas with the highest smectite contents (>60%) are located in the west of Luzon and in the Gulf of Thailand, respectively (Fig. 8A). In most parts of the Sunda Shelf, the central basin, and the Gulf of Tonkin, the smectite content is also high, usually >40%. In contrast, the smectite content is quite low (mostly <5%) in the northeastern SCS surrounding Taiwan, offshore South China, and offshore North Borneo. Instead, illite is abundant in the northeastern SCS with two high-value belts (>40%) extending from the region surrounding Taiwan, where the illite content is >60%, southwestward to the lower part of continental slope and westward to the continental shelf (Fig. 8B). The North Borneo offshore also has a narrow belt of high content of illite (>40%). In most parts of SCS basin, the illite content is generally higher than 30%. However, in offshore Luzon, the Gulf of Thailand, and the major part of Gulf of Tonkin, the illite content is low, generally less than 20%. Our results with high content of smectite (average 71%) in the Gulf of Thailand are quite different from those obtained in a recent investigation by Shi et al. (2015), who suggest clay mineral assemblages of major illite (30–63%), moderate kaolinite (25–48%) and chlorite (9–23%), and minor smectite (0–16%) for surface sediments in the western Gulf of Thailand. Their analytical technique used a pretreatment of ethylene–glycol solvation that have may strongly affected the detection of expanded smectite, and thus more technique details need to be examined before direct comparison can be made of the two sets of clay mineralogy data.

Kaolinite and chlorite are two minor clay minerals on the seafloor with average contents of 16% and 18%, respectively. The kaolinite distribution presents three remarkable features (Fig. 8C): (1) the kaolinite distribution with high values (>50%) is very limited, only found in the narrow coastal zones of South China, northern Vietnam, and Malay Peninsula; (2) the kaolinite content is moderate (around 15–30%) in the southern SCS including the Sunda Shelf; and (3) in the central–eastern and northeastern SCS, the kaolinite content is very low, mostly less than 10% and even less than 5% west of Luzon. The chlorite distribution shows a similar pattern to the illite distribution throughout the entire seafloor (Fig. 8D), but generally its contents are less than illite by ~20%. The linear correlation between illite and chlorite of all seafloor surface samples confirm that the two minerals have similar variation trends throughout the SCS (Fig. 7B).

Based on the spatial distribution of the four major clay mineral contents, we divide the basin-wide clay mineral assemblage into eight provinces (Fig. 9). Provinces A–D cover most seafloor areas and provinces E–H are located in limited areas. Province A (Northeastern SCS) is characteristic of high contents of illite and chlorite (total ~80%) with minor smectite and kaolinite. Such an illite and chlorite assemblage presents a clear Taiwan-sourced clay mineral feature with a mixture of smectite from Luzon (Figs. 6B and 8B, D). Province B (Eastern SCS) is represented by a very high content of smectite (63%) with minor illite, chlorite, and kaolinite, and the clay minerals in this province show a Luzon-sourced feature (Figs. 6B and 8A). Province C (Northwestern SCS) shows a clay mineral assemblage with moderate contents of four species, i.e., smectite (32%), illite (30%), chlorite (20%), and kaolinite (18%). Similarly, Province D (Southern SCS) displays moderate contents of the four clay mineral species with relatively higher content of smectite, i.e., smectite (38%), illite (26%), chlorite (16%), and kaolinite (20%). The moderate contents of clay mineral distributions in these two provinces may reflect a strong mixture of clay mineral species from different sources, with relatively more kaolinite to Province D from southern sources, e.g., the Malay Peninsula, Sumatra, and Borneo (Fig. 6B). Province E (Gulf of Thailand) is also characterized by high content of smectite (71%) with minor kaolinite and illite and scarce

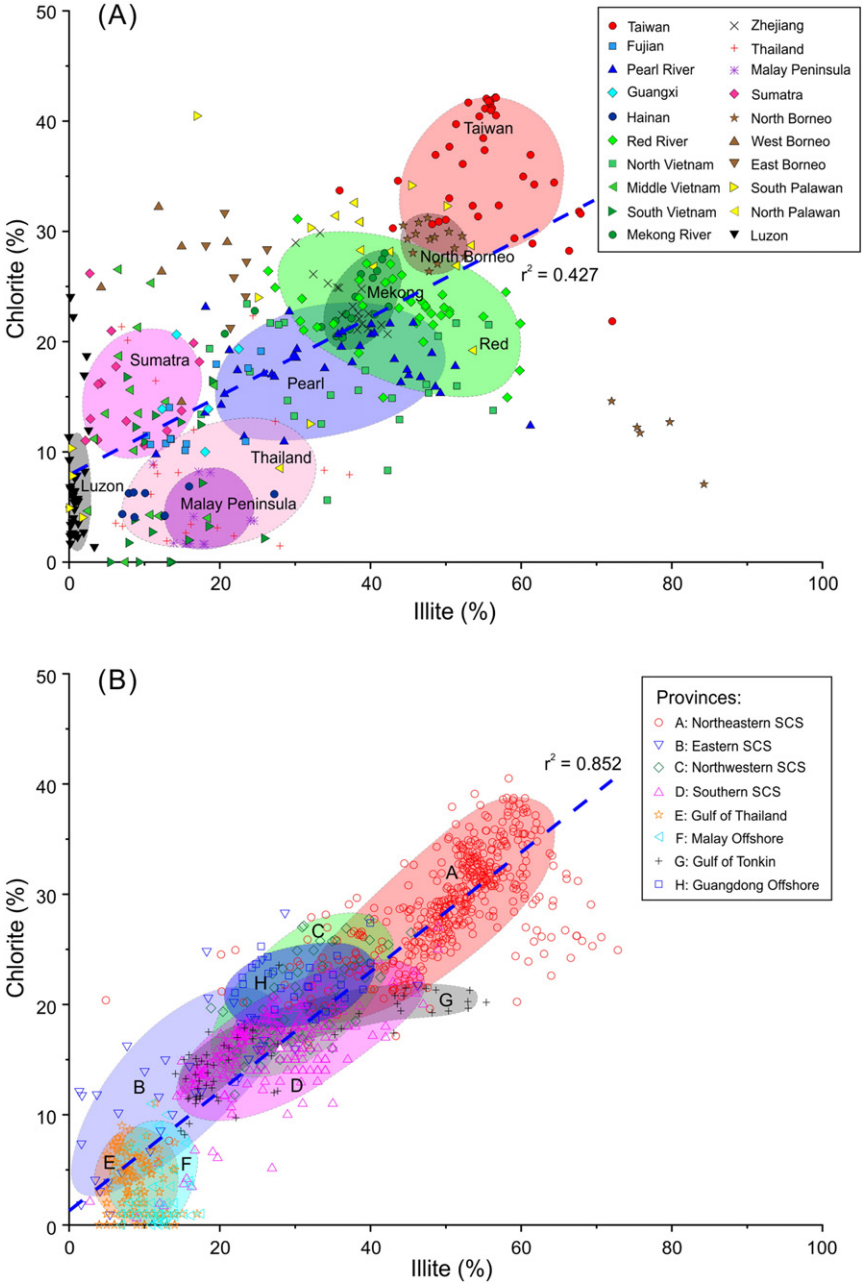

Fig. 7. Linear correlation between illite (%) and chlorite (%) in surface sediments of the SCS and surrounding fluvial drainage systems. (A) Fluvial surface samples. Shaded areas show nine major drainage systems with significant fluvial sediment discharge. (B) Seafloor surface samples. Shaded areas show eight provinces (A–H) of clay mineral assemblages distributed in surface samples. Refer to the caption of Fig. 4 for sources of published data.

chlorite. The high content of smectite in this province fits well with the high smectite content in fluvial sediments of Middle Thailand implying its origin (Figs. 5 and 6B). Province F (Malay Offshore) is limited in a narrow coastal belt with the high content of kaolinite offshore the Malay Peninsula. The dominant kaolinite (51%) and smectite (35%) comprise the major clay mineral components in this province, suggesting that the majority of kaolinite is from the Malay Peninsula with the mixture of smectite from other sources (Fig. 6B). Province G (Gulf of Tonkin) contains moderate contents of four clay mineral species, i.e., smectite (36%), illite (27%), chlorite (16%), and kaolinite (21%). This province has a similar clay mineralogical character as the Red River with varied smectite contents (Fig. 6B). Province H (Guangdong Offshore) is constrained in the coastal zone offshore South China with the relatively high content of kaolinite (33%) consistent with the major source being the Pearl River (Figs. 6B and 8C).

3.3.2. Provenance control and differential settling

The distribution of clay mineral assemblages on the entire seafloor shows three significant features (Figs. 8 and 9): (1) The clay mineral distribution is strongly controlled by the provenance, especially in some areas adjacent to drainage systems with their prevailing clay mineral species, such as high contents of illite and chlorite in the northeastern SCS nearby Taiwan (Province A) and high content of smectite in the eastern SCS nearby Luzon (Province B). (2) The differential settling occurs at least for kaolinite and smectite sedimentation through their transport from fluvial estuary to abyssal basin by

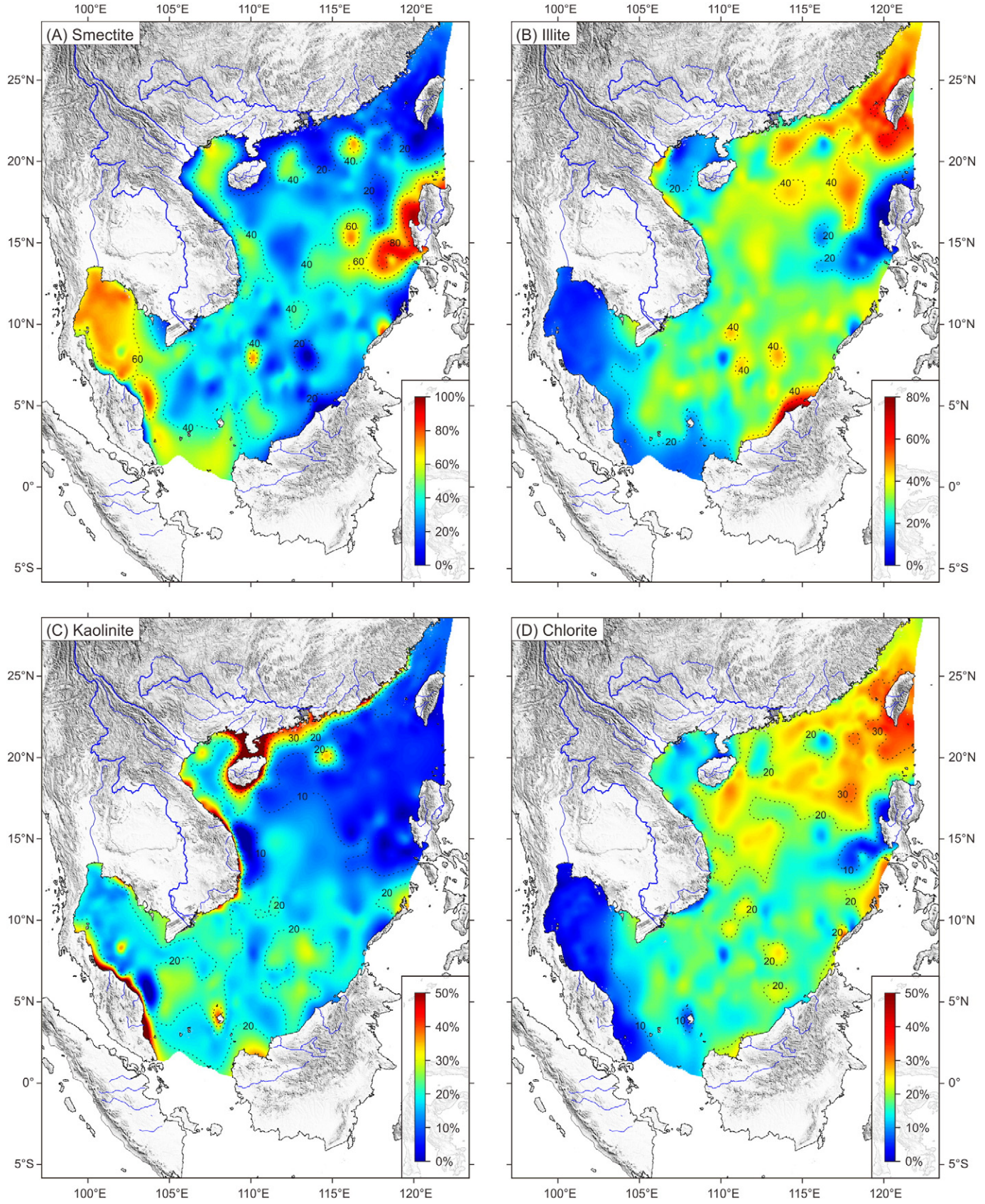

Fig. 8. Spatial distribution of the percentage contents of four major clay minerals in seafloor surface sediments in the SCS. (A) Smectite. (B) Illite. (C) Kaolinite. (D) Chlorite. Note that scales on color bar are variable for the four maps.

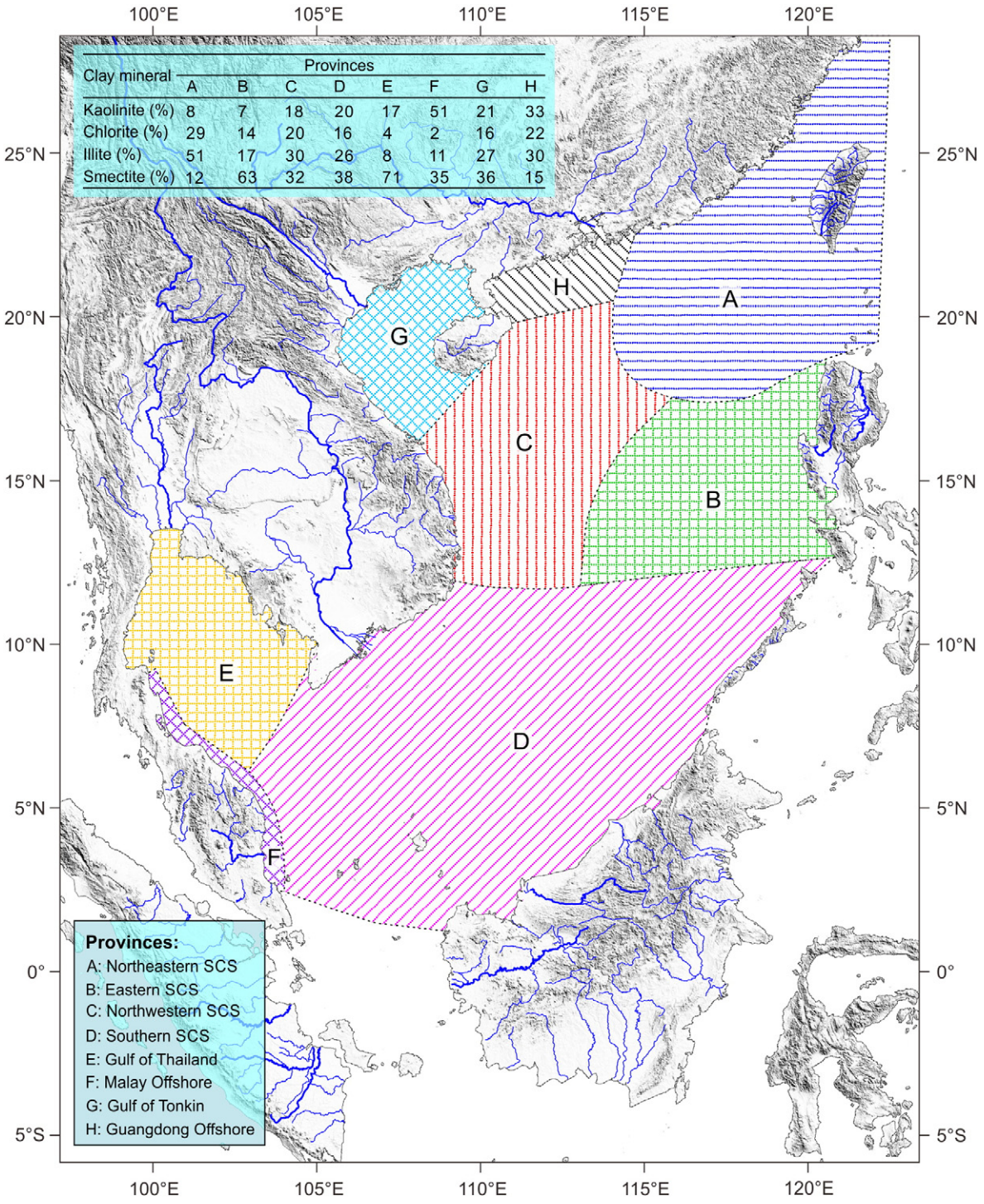

Fig. 9. Distribution of clay mineral assemblage provinces (A–H) in seafloor surface sediments of the SCS. Average contents of clay minerals in all provinces are indicated. The determination of various provinces is based on approximate changes of clay mineral assemblages with some uncertainty when investigated sample locations are sparse. The range of Province H is mainly based on the 20% kaolinite contour line (Liu et al., 2010b).

comparing the clay mineral assemblages in river sediments with seafloor surface sediments. (3) All four clay mineral species are relatively homogeneous with similar contents in the western and southern SCS (Provinces C and D) despite being at different water depths and close to various fluvial systems.

High contents of illite and chlorite in the northeastern SCS with extremely high values of >90% surrounding Taiwan gradually decrease westward and southwestward to ~60% on the continental shelf and the abyssal basin, indicating a Taiwan-sourced illite and chlorite assemblage (Fig. 8B, D). This distribution pattern fits well with the high contents of illite and chlorite in Taiwan rivers (Fig. 5). Similarly, the high content of illite off North Borneo suggests that the prevailing origin of illite derives from North Borneo (Fig. 8B). In the eastern SCS and the Gulf of Thailand, high content of smectite suggests provenance-controlling transport processes, with sediments deriving from nearby Luzon and Middle Thailand fluvial systems, respectively (Fig. 8A).

However, widely distributed kaolinite in surrounding fluvial systems with high values, generally close to or much larger than

50% in South China, most parts of Vietnam, the Malay Peninsula, Sumatra, and West and East Borneo, extends only to narrow coastal zones offshore of the source regions (provinces F and H) (Fig. 8C), unlike the cases of widely distributed illite and chlorite with high contents in the northeastern SCS or smectite in the eastern SCS. The obvious contrast between kaolinite-rich source areas and the limited seafloor extent suggests that most of kaolinite settles out as soon as it enters the sea or is transported only for a limited distance in the nearby coastal zone. On the contrary, the smectite content is usually high (generally >40%) in most parts of the central and eastern basin, the Gulf of Tonkin, the Sunda Shelf, and the Gulf of Thailand (Fig. 8A). Such a distribution does not fit the smectite sources in surrounding drainage systems, where the smectite content in most rivers is quite low (<15%); only the rivers of Luzon provide a very high content of smectite (87%) (Fig. 5). Even in the Gulf of Thailand, the surface seafloor sediments have a high content of smectite, mostly >60%, and river samples from Middle Thailand only contain an average of 42%. We interpret this to mean that strong differential settling occurs at least for kaolinite and smectite sedimentation during their transport from fluvial mouth to the abyssal basin (Liu and Li, 2011). Kaolinite is usually large in size, ranging from 0.5 to 8.0 μm, and smectite is usually smaller than 1 μm (Gibbs, 1977; Johnson and Kelley, 1984). The larger kaolinite likely settles faster than smectite during their transport (Gibbs, 1977). Furthermore, the flocculation of kaolinite in alkaline seawater is enhanced, speeding up its deposition (Chamley, 1989; Patchineelam and De Figueiredo, 2000). Instead, the flocculation of smectite is considered to be accelerated in more saline and distal waters (Patchineelam and De Figueiredo, 2000). This mechanism would explain the very limited

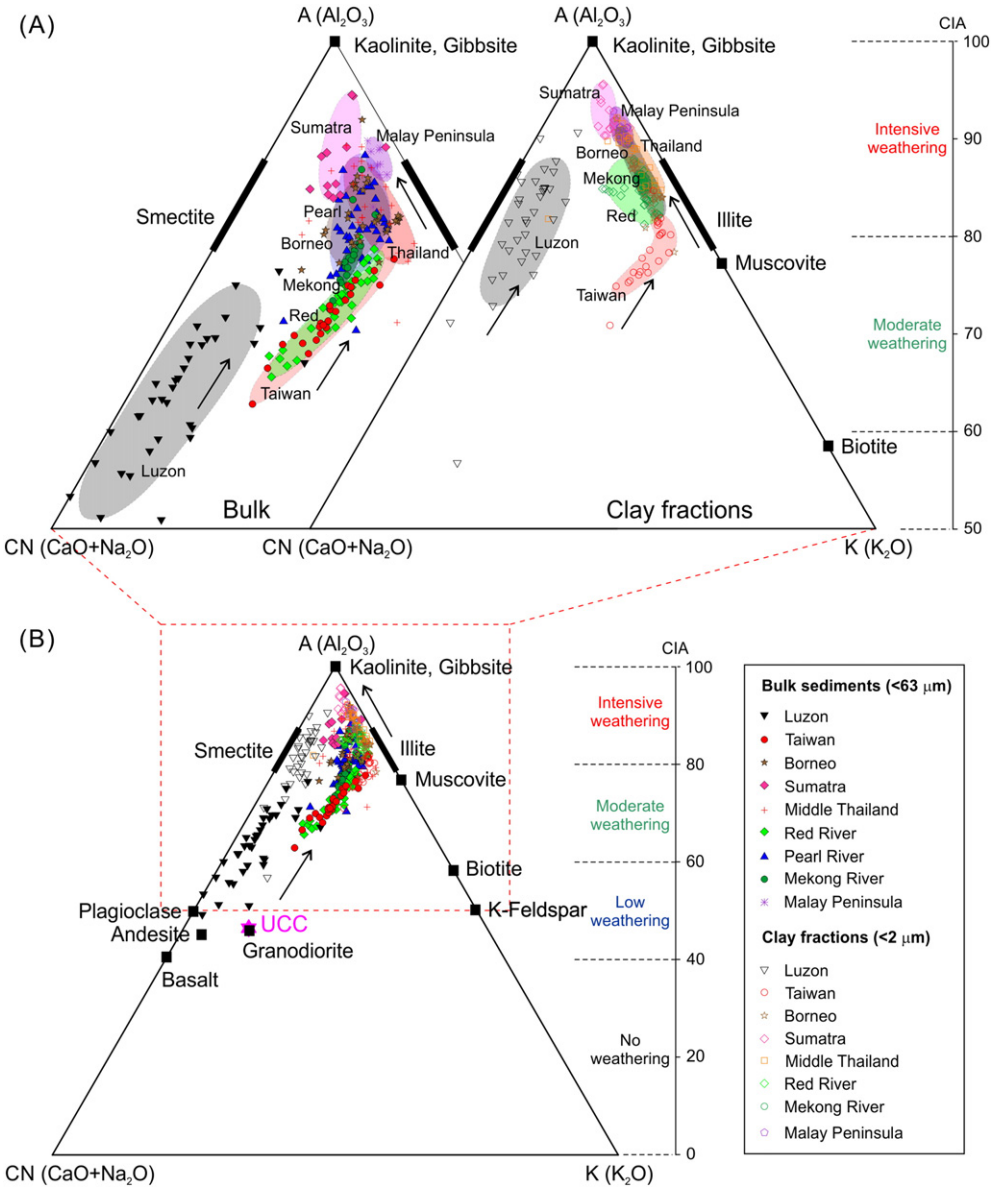

Fig. 10. Major elemental Al_2O_3–(CaO + Na_2O)–K_2O (A–CN–K) ternary diagram of bulk and clay-fraction sediments in surrounding fluvial drainage systems showing their weathering trends. A (left: bulk sediments; right: clay fractions) is an enlarged plot of the dashed box in B. UCC (upper continental crust) (Taylor and McLennan, 1985) is plotted as a reference point. Arrows indicate weathering trends exhibited by these river sediments, showing that clay-fraction sediments have experienced stronger chemical weathering than bulk sediments. Shaded areas show nine major drainage systems with significant fluvial sediment discharge. Scales for the chemical index of alteration (CIA = [Al_2O_3 / (Al_2O_3 + CaO* + Na_2O + K_2O)] × 100, where CaO* represents CaO associated with the silicate fraction of the sample; Nesbitt and Young, 1982) are indicated to show the degrees of chemical weathering with values less than 40 meaning no weathering, values between 40 and 60 showing low weathering, values between 60 and 80 indicating moderate weathering, and values between 80 and 100 representing intensive weathering.

distribution of kaolinite in provinces F and H versus the widespread smectite.

Similar amounts of four clay mineral species in the western and southern SCS (Fig. 8) reflect ocean mixing and/or the initial mixed river source from the surrounding drainage systems. For instance, high contents of illite and chlorite with low content of smectite from the Mekong River are completely mixed upon entering the sea, and their transport pathway even in the coastal zone off the river mouth is not traceable from the surface sediment. Similarly, relatively high content of kaolinite and high content of illite can only be observed in narrow coastal belts off northwestern and northern Borneo, respectively. Apart from the coastal zones of Borneo, fluvial sediments in the entire central and southern basin are highly mixed.

3.4. Major elemental and Nd–Sr isotopic compositions

Like the clay mineralogical distribution in the fluvial systems, major elements (Fig. 10) and Nd–Sr isotopic compositions (Fig. 11) are also similar in each major drainage system or region defined as a province, but largely different between provinces.

3.4.1. Major elemental compositions of fluvial sediments

Major elements of both bulk and clay-fraction sediments from major river samples consist mainly of SiO_2, Al_2O_3, and Fe_2O_3, and their total content is up to ~80%; concentrations of CaO, K_2O, MgO, MnO, Na_2O, P_2O_5, and TiO_2 are relatively low, with their total content less than 6% (Supplementary data Table S2) (Liu et al., 2007b, 2009b, 2012). By comparing bulk with clay-fraction major element compositions, we find that clay-fraction sediments usually contain higher Al_2O_3, Fe_2O_3, and TiO_2, and lower SiO_2, CaO, K_2O, and Na_2O than bulk sediments, indicating that clay-fraction sediments are enriched with the immobile elements and are leached of the mobile elements during the chemical weathering process.

The chemical leaching of mobile alkali and alkaline elements can be well understood by plots of weathering trends such as the Al_2O_3–(CaO + Na_2O)–K_2O (A–CN–K) ternary diagram (Nesbitt and Young, 1984, 1989). The overall results show that both bulk and clay-fraction sediments from all river samples display different levels of chemical weathering from the low-moderate degrees in Luzon to the intensive degree in Sumatra and the Malay Peninsula (Fig. 10). Clay-fraction samples are much closer to the Al_2O_3 apex than bulk samples (Fig. 10A), indicating preferential leaching of CaO, Na_2O, and K_2O, and enrichment of Al_2O_3 during the formation of clay minerals.

All Luzon river samples plot linearly and parallel to the A–CN line, indicating preferential leaching of CaO and Na_2O and enrichment of Al_2O_3, while K_2O contents (less abundant) are constant, under low-moderate degrees of chemical weathering for bulk sediments and moderate-intensive degrees of chemical weathering for clay-fraction sediments as indicated by their chemical index of alternation (CIA) values of 50–70 and 70–85, respectively (Fig. 10). The distribution of data plots close to the A–CN line, completely separated from all other samples in both bulk and clay-fraction sediments, suggests a majority of andesitic–basaltic volcanic rock sources (Liu et al., 2009b). The clay-fraction plots very close to the smectite reference segment, fitting well with the predominance of smectite in clay mineral assemblages in Luzon river sediments (Fig. 5).

River samples from Taiwan, the Red River, and the Mekong River present a moderate degree of chemical weathering for bulk sediments (CIA = 60–80) and an intensive degree for most clay-fraction sediments (CIA = 75–90) except for Taiwan samples (Fig. 10). Samples from the Pearl River, Middle Thailand, and Borneo show moderate–intensive weathering degrees for bulk sediments (CIA = 75–85) and an intensive

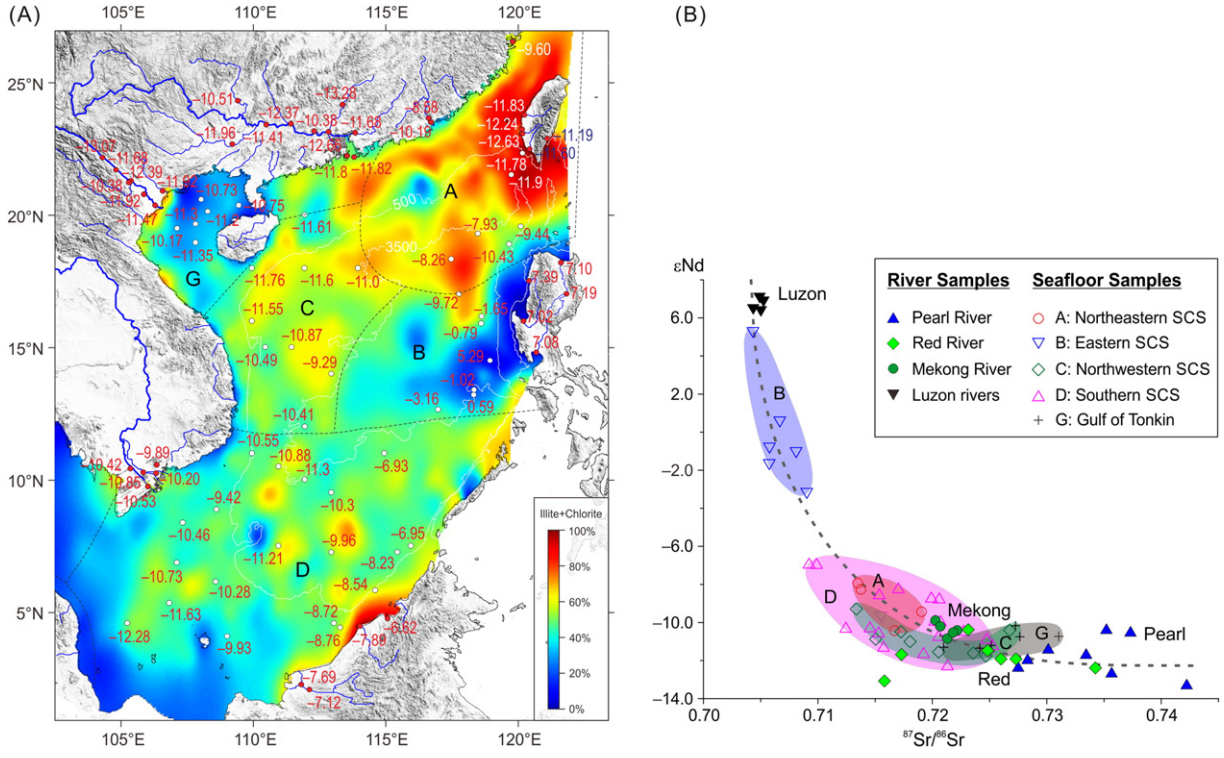

Fig. 11. Distribution of εNd values and correlation between εNd and $^{87}Sr/^{86}Sr$ of surface sediments in the SCS and surrounding fluvial drainage systems. (A) Locations of surface samples and their εNd values. Distribution of illite + chlorite percentage on the seafloor is plotted for comparison. Dashed black lines show the clay mineral assemblage provinces. (B) Correlation between εNd and $^{87}Sr/^{86}Sr$ of surface sediments. Shaded areas show corresponding five provinces on the seafloor with available data of εNd and $^{87}Sr/^{86}Sr$. Data of the Pearl, Red, and Mekong rivers from Liu et al. (2007b); two data points at the Pearl River mouth from Li et al. (2003) and Shao et al. (2009); Hanjiang and Minjiang river values from Shao et al. (2009); SCS surface samples from Li et al. (2003) and Wei et al. (2012). Nd isotopic data of Taiwan, Luzon, and Borneo in (A) are new data of this study. Data of Luzon in (B) were derived from river suspended particles (Goldstein and Jacobsen, 1988). See Table 3 for detailed Nd and Sr isotopic compositions.

Table 3
Nd and Sr isotopes of surface sediments in the SCS and surrounding fluvial drainage systems.

No.	Sample	Latitude (°N)	Longitude (°E)	$^{87}Sr/^{86}Sr$	$^{143}Nd/^{144}Nd$	εNd	Data source
Northeastern SCS (Province A)							
1	92	19.565	120.155	0.719055 ± 13	0.512154 ± 13	−9.44	Wei et al. (2012)
2	94	19.292	118.530	0.713477 ± 17	0.512232 ± 13	−7.93	Wei et al. (2012)
3	105	18.905	119.710	0.716697 ± 16	0.512103 ± 12	−10.43	Wei et al. (2012)
4	165	18.340	117.533	0.713764 ± 17	0.512215 ± 12	−8.26	Wei et al. (2012)
5	185	17.012	117.827	0.715510 ± 17	0.512140 ± 13	−9.72	Wei et al. (2012)
6	T6-10	Taiwan Offshore		–	0.512070 ± 8	−11.08	Shao et al. (2009)
7	79-38	21.533	119.800	–	0.512029 ± 8	−11.9	Li et al. (2003)
Eastern SCS (Province B)							
8	198	16.177	118.670	0.705755 ± 17	0.512554 ± 13	−1.65	Wei et al. (2012)
9	208	15.902	118.667	0.705773 ± 18	0.512598 ± 12	−0.79	Wei et al. (2012)
10	254	14.492	118.995	0.704326 ± 17	0.512909 ± 13	5.29	Wei et al. (2012)
11	295	13.205	118.383	0.706674 ± 17	0.512668 ± 13	0.59	Wei et al. (2012)
12	307	12.650	117.030	0.709025 ± 17	0.512476 ± 13	−3.16	Wei et al. (2012)
13	320	13.397	118.392	0.708098 ± 16	0.512586 ± 11	−1.02	Wei et al. (2012)
Northwestern SCS (Province C)							
14	S003	20.000	112.000	0.723583 ± 19	0.512043 ± 12	−11.61	Wei et al. (2012)
15	S009	18.000	110.000	0.724684 ± 19	0.512035 ± 12	−11.76	Wei et al. (2012)
16	S007	18.000	114.000	0.718058 ± 18	0.512074 ± 12	−11.0	Wei et al. (2012)
17	S013	16.000	110.000	0.720548 ± 17	0.512046 ± 12	−11.55	Wei et al. (2012)
18	S016	15.000	110.500	0.717267 ± 17	0.512100 ± 12	−10.49	Wei et al. (2012)
19	S018	15.000	111.500	0.715053 ± 17	0.512081 ± 12	−10.87	Wei et al. (2012)
20	S021	14.000	113.000	0.713366 ± 9	0.512162 ± 12	−9.29	Wei et al. (2012)
21	S024	12.000	112.000	0.726755 ± 20	0.512105 ± 12	−10.41	Wei et al. (2012)
22	83-18	18.001	111.986	–	0.512043 ± 7	−11.6	Li et al. (2003)
Southern SCS (Province D)							
23	S029	11.000	110.000	0.715303 ± 17	0.512097 ± 12	−10.55	Wei et al. (2012)
24	NS90-68	8.370	107.383	0.722726 ± 30	0.512102 ± 9	−10.46	Wei et al. (2012)
25	NS90-70	8.867	108.665	–	0.512155 ± 7	−9.42	Wei et al. (2012)
26	S031	10.500	111.000	0.724758 ± 17	0.512080 ± 13	−10.88	Wei et al. (2012)
27	S033	10.000	112.000	0.715740 ± 19	0.512059 ± 11	−11.3	Wei et al. (2012)
28	S035	9.500	113.000	0.712441 ± 16	0.512110 ± 12	−10.3	Wei et al. (2012)
29	S043	7.500	111.000	0.725279 ± 17	0.512063 ± 12	−11.21	Wei et al. (2012)
30	S047	7.250	113.000	0.720711 ± 17	0.512127 ± 12	−9.96	Wei et al. (2012)
31	S052	7.250	115.500	0.717031 ± 13	0.512216 ± 11	−8.23	Wei et al. (2012)
32	S053	7.500	116.000	0.709882 ± 17	0.512282 ± 12	−6.95	Wei et al. (2012)
33	NS88-44	5.818	114.651	0.715360 ± 56	0.512200 ± 8	−8.54	Wei et al. (2012)
34	NS88-62	4.404	113.336	0.720602 ± 18	0.512189 ± 7	−8.76	Wei et al. (2012)
35	NS88-68	4.566	113.097	0.719912 ± 17	0.512191 ± 7	−8.72	Wei et al. (2012)
36	NS90-40	6.136	108.628	0.714553 ± 14	0.512111 ± 7	−10.28	Wei et al. (2012)
37	NS90-54	6.854	107.159	0.720555 ± 30	0.512088 ± 8	−10.73	Wei et al. (2012)
38	NS90-57	5.334	106.876	0.719230 ± 17	0.512042 ± 6	−11.63	Wei et al. (2012)
39	NS90-59	4.559	105.285	0.721330 ± 40	0.512009 ± 10	−12.28	Wei et al. (2012)
40	NS89-61	4.073	109.066	0.720222 ± 28	0.512129 ± 8	−9.93	Wei et al. (2012)
41	S057	11.000	115.000	0.709235 ± 17	0.512283 ± 11	−6.93	Wei et al. (2012)
Gulf of Tonkin (Province G)							
42	B22	20.600	108.083	0.731040 ± 18	0.512088 ± 12	−10.73	Wei et al. (2012)
43	B36	20.367	109.500	0.727645 ± 17	0.512087 ± 10	−10.75	Wei et al. (2012)
44	B39	20.133	108.333	0.725148 ± 19	0.512064 ± 12	−11.2	Wei et al. (2012)
45	B55	19.667	107.867	0.720986 ± 13	0.512059 ± 12	−11.3	Wei et al. (2012)
46	B61	19.500	107.167	0.727262 ± 19	0.512117 ± 12	−10.17	Wei et al. (2012)
47	B78	18.967	107.867	0.724148 ± 19	0.512056 ± 12	−11.35	Wei et al. (2012)
Pearl River							
48	PR04	23.110	113.896	0.733442 ± 3	0.512039 ± 41	−11.68	Liu et al. (2007b)
49	PR09-2	24.180	113.422	0.742222 ± 5	0.511957 ± 6	−13.28	Liu et al. (2007b)
50	PR15-2	23.151	112.891	0.735662 ± 6	0.511989 ± 5	−12.66	Liu et al. (2007b)
51	PR19	23.172	112.346	0.735209 ± 3	0.512106 ± 9	−10.38	Liu et al. (2007b)
52	PR25	23.456	111.480	0.727507 ± 2	0.512004 ± 3	−12.37	Liu et al. (2007b)
53	PR30	23.423	110.536	0.730134 ± 3	0.512053 ± 9	−11.41	Liu et al. (2007b)
54	PR37-2	24.317	109.468	0.737314 ± 5	0.512099 ± 29	−10.51	Liu et al. (2007b)
55	PR40-1	22.681	109.260	0.728329 ± 2	0.512025 ± 3	−11.96	Liu et al. (2007b)
56	LDY-2	22.240	113.590	–	0.512033 ± 6	−11.8	Li et al. (2003)
57	L1-5	Lingdingyang		–	0.512032 ± 8	−11.82	Shao et al. (2009)
Red River							
58	RS03	21.288	105.437	0.734244 ± 4	0.512003 ± 4	−12.39	Liu et al. (2007b)
59	RS11	22.170	104.353	0.715813 ± 3	0.511968 ± 4	−13.07	Liu et al. (2007b)
60	RS16	21.707	104.868	0.717309 ± 3	0.512039 ± 4	−11.68	Liu et al. (2007b)
61	RS23	21.234	105.350	0.723133 ± 3	0.512106 ± 6	−10.38	Liu et al. (2007b)
62	RS26	20.787	105.923	0.725997 ± 3	0.512027 ± 6	−11.92	Liu et al. (2007b)
63	RS32	20.370	106.344	0.724829 ± 5	0.51205 ± 3	−11.47	Liu et al. (2007b)
64	RS35	20.914	106.622	0.727307 ± 3	0.512027 ± 5	−11.92	Liu et al. (2007b)

(continued on next page)

Table 3 (*continued*)

No.	Sample	Latitude (°N)	Longitude (°E)	$^{87}Sr/^{86}Sr$	$^{143}Nd/^{144}Nd$	εNd	Data source
Mekong River							
65	MR02	10.555	106.407	0.720276 ± 3	0.512131 ± 5	−9.89	Liu et al. (2007b)
66	MR04	10.235	106.373	0.720699 ± 2	0.512115 ± 4	−10.20	Liu et al. (2007b)
67	MR09	10.271	105.892	0.721307 ± 3	0.512082 ± 5	−10.85	Liu et al. (2007b)
68	MR13	10.420	105.410	0.722173 ± 3	0.512104 ± 5	−10.42	Liu et al. (2007b)
69	MR16	9.735	106.074	0.721801 ± 3	0.512098 ± 5	−10.53	Liu et al. (2007b)
Luzon rivers							
70	LZ03	14.939	120.761	–	0.513001 ± 4	7.08	This study
71	LZ13	15.980	120.226	–	0.512998 ± 4	7.02	This study
72	LZ22	17.559	120.467	–	0.513017 ± 4	7.39	This study
73	LZ31	18.123	121.673	–	0.513002 ± 4	7.10	This study
74	LZ36	16.972	121.657	–	0.513006 ± 4	7.19	This study
75	Arba[a]	17.517	120.400	0.70502 ± 3	0.512175 ± 19	6.4	Goldstein and Jacobsen (1988)
76	Agno[a]	15.980	120.226	0.70435 ± 5	0.512181 ± 14	6.5	Goldstein and Jacobsen (1988)
77	Cagayan[a]	18.123	121.673	0.70524 ± 4	0.512201 ± 11	6.9	Goldstein and Jacobsen (1988)
78	Pampanga[a]	15.515	120.956	0.70491 ± 5	0.512208 ± 14	7.1	Goldstein and Jacobsen (1988)
Taiwan rivers							
79	CK2	23.836	120.284	–	0.512032 ± 4	−11.83	This study
80	CK5	23.085	120.127	–	0.512010 ± 4	−12.24	This study
81	CK6	22.918	120.185	–	0.511991 ± 4	−12.63	This study
82	CK7-1	22.637	120.442	–	0.512043 ± 4	−11.60	This study
83	CK10	22.794	121.139	–	0.512065 ± 3	−11.19	This study
Hanjiang River							
84	H1	Hanjiang River		–	0.512198 ± 13	−8.58	Shao et al. (2009)
85	H2	Hanjiang River		–	0.512116 ± 11	−10.19	Shao et al. (2009)
Minjiang River							
86	M1	Minjiang River		–	0.512146 ± 9	−9.60	Shao et al. (2009)
Borneo rivers							
87	BN5	4.903	115.154	–	0.512299 ± 4	−6.62	This study
88	BN12	4.596	113.953	–	0.512233 ± 5	−7.89	This study
89	MK16	2.282	111.814	–	0.512244 ± 5	−7.69	This study
90	MK19	2.106	112.158	–	0.512273 ± 5	−7.12	This study

[a] Samples from suspended particles of rivers.

degree for clay-fraction sediments (CIA = 85–95) (Fig. 10) (Liu et al., 2007b, 2012). Their weathering trends show the leaching of CaO and Na_2O first (plots linearly parallel to the A–CN line) and then removal of K_2O (plots parallel to the A–K line). The shift of chemical leaching from CaO and Na_2O to K_2O occurs approximately at the transition of moderate to intensive degrees of chemical weathering. The correlation to references of UCC (upper continental crust) and granodiorite, suggest that the source rocks are upper continental crust, e.g., granodiorite and intermediate sedimentary rocks. The chemical weathering processes indicated by the leaching of alkali and alkaline elements correspond well to the clay mineral assemblages. For example, the moderate weathering in drainage systems of Taiwan, the Red River, and the Mekong River corresponds to high contents of illite and chlorite, which are formed through weak hydrolysis and/or strong physical erosion of bedrocks, and the moderate–intensive weathering in drainage systems of the Pearl River, Middle Thailand, and Borneo corresponds to a relatively high content of kaolinite reflecting the intensive weathering.

Major elements of fluvial samples in Sumatra and the Malay Peninsula indicate strongly intensive weathering for both bulk and clay-fraction sediments (CIA = 85–95), as they plot parallel to the A–K line and closer to the Al_2O_3 apex than all other samples (Fig. 10) (Liu et al., 2012). The extremely strong chemical weathering in these two regions, which corresponds to high content of kaolinite (78% in the Malay Peninsula and 57% in Sumatra, respectively; Fig. 5), is due to the warm and humid East Asian monsoon climate conditions. Furthermore, parent rocks enriched in alkali and alkaline elements (e.g., granite, granodiorite, and intermediate-acid volcanic rocks) such as in the Malay Peninsula are easily and intensively weathered to form kaolinite. However, the majority of Quaternary intermediate-basic volcanic rocks and Upper Tertiary sedimentary rocks in Sumatra can also produce very high content of kaolinite, because the monsoon climate with high temperature and abundant precipitation greatly strengthens the chemical weathering process (Liu et al., 2012).

Therefore, these results show that not only climate and tectonism but also the lithologies of parent rocks in drainage systems play significant roles in the outcome of the weathering processes. Four controlling mechanisms of chemical weathering can be summarized: (1) The long-term tropical warm and humid climate combined with relatively stable tectonic setting leads to strongly intensive chemical weathering regardless of the variability in parent rocks, e.g., the Malay Peninsula and Sumatra (Liu et al., 2012). (2) The strong tectonic uplift combined with tropical warm and humid climate or the stable tectonic setting combined with subtropical warm and humid climate can induce moderate–intensive chemical weathering, e.g., Borneo and South China (Liu et al., 2007b, 2012). (3) The strong tectonic uplift combined with subtropical warm and humid climate can produce the moderate chemical weathering, e.g., Taiwan and the Indochina Peninsula (Liu et al., 2007b). (4) The lithology-dominated control (volcanic rocks) under subtropical climate conditions usually yields low to moderate chemical weathering, e.g., Luzon (Liu et al., 2009b).

3.4.2. Nd and Sr isotopic compositions of fluvial and seafloor surface sediments

Nd and Sr isotopes are proven tracers for provenance studies of terrigenous particles in marine sediments (Grousset et al., 1988; Colin et al., 1999, 2006). These tracers have been applied for fluvial sediment provenance studies in the SCS at different time scales, including modern processes by analyzing seafloor surface sediments (Wei et al., 2012), the glacial–interglacial variation during the Late Quaternary based on

studying sediment cores (Boulay et al., 2005; Liu et al., 2005), and the long-term geological history since the early Oligocene by studying ocean drill cores (Clift et al., 2002; Li et al., 2003). The agreement of these provenance studies of SCS fluvial sediments is remarkable, although some strong debates regarding sediment provenances at the geological time scales are still ongoing (Clift et al., 2002; Li et al., 2003). Here, we synthesize available literature data combined with our new results on εNd and $^{87}Sr/^{86}Sr$ isotopes of surface sediments in the SCS and surrounding fluvial drainage systems to obtain basin-wide fluvial sediment provenances.

The spatial distribution of εNd values of 47 seafloor surface samples and 53 river samples shows rough zonal features indicating that values of seafloor sediments are highly correlated to river sediments in nearby fluvial drainage systems (Fig. 11A, Table 3). The Pearl and Red river systems have similar εNd composition ranges, from −13.28 to −10.38 (average −11.79) and from −13.07 to −10.38 (average −11.83), respectively, presenting a challenge to separate the two sources if using merely the single εNd tracer (Liu et al., 2007b). The εNd values of Taiwan samples range from −12.63 to −11.19 (average −11.90), also falling within the variation range of the Pearl and Red rivers, suggesting that the neodymium isotope is not an efficient tracer for sediment provenance analysis in the northern SCS. Surface sediments on the Mekong River delta provide similar εNd compositions, from −10.85 to −9.89 (average −10.38), slightly larger than values in Red and Pearl river systems (Liu et al., 2007b). However, fluvial sediments in Luzon rivers have the most positive εNd values, ranging from 7.02 to 7.39 (average 7.16), very close to earlier published values from suspended particles collected in same rivers with a range of 6.4–7.1 (average 6.73) (Table 3; Goldstein and Jacobsen, 1988), providing a strong contrast between Luzon and South China and the Indochina Peninsula. In the south, river samples of Borneo provide εNd values ranging from −7.89 to −6.62 (average −7.33), very different from the Mekong River sediments.

The rough zonal distribution of εNd values on the SCS seafloor fits generally well with the clay mineral assemblage provinces, despite the difficulty of mapping the isotopic distribution with contour lines (Fig. 11A). In the northeastern SCS (Province A), εNd values increase from about −11.9 in nearby Taiwan southwestward to about −8.26 in the deep basin (Shao et al., 2009; Wei et al., 2012), showing the strong mixture of Taiwan- with Luzon-sourced sediments. Such a mixture trend is also well presented by the high-value belt of abundant illite and chlorite extending from Taiwan southwestward to the deep basin (Fig. 11A). Further to the south, εNd values range from −3.16 to 5.29 (average −0.12) in the eastern SCS (Province B), where the illite and chlorite assemblage is less than 40% and the smectite content is higher than 40%, indicating dominant sediment input from nearby Luzon (Wei et al., 2012). In the northwestern SCS (Province C), εNd values are similar to each other from −11.76 to −9.29 (average −10.95), close to values in the Pearl and Red river systems. Similarly, in the Gulf of Tonkin (Province G), εNd values are from −11.35 to −10.17 (average −10.92), suggesting that the εNd cannot distinguish sediments from provinces C and G. However, in the southern SCS (Province D), εNd values in the eastern part (near Borneo) are more positive, ranging from −8.76 to −6.95 (average −8.24) (Li et al., 2003; Wei et al., 2012), representing the important sediment input from Borneo. In most of the southern SCS, εNd values vary from −12.28 to −9.42 (average −10.69) (Wei et al., 2012), going beyond the value range (from −10.85 to −9.89) of Mekong River sediments, suggesting a strong mixture of various provenances.

Coupled with Nd isotopes, Sr isotopic compositions can be also used to identify the provenance of SCS sediments (Boulay et al., 2005; Liu et al., 2005; Wei et al., 2012), although $^{87}Sr/^{86}Sr$ values could be slightly altered by strong chemical weathering (Colin et al., 2006). Sediments in the western SCS and the Gulf of Tonkin (provinces C and G) have the highest $^{87}Sr/^{86}Sr$ (0.7134–0.7310) and lowest εNd (−11.76 to −9.29) values (Wei et al., 2012), and their sources could be identified from one of or both Pearl and Red river systems (Fig. 11B, Table 3). Instead, sediments in the eastern SCS (Province B) have the lowest $^{87}Sr/^{86}Sr$ (0.7043–0.7090) and highest εNd (−3.16 to 5.29) values, and they are clearly derived from Luzon (Wei et al., 2012). However, northeastern SCS sediments (Province A) have εNd values that are between values for the Pearl River, Luzon, and Taiwan, showing a potential mixture of sediments. Because $^{87}Sr/^{86}Sr$ values are not available for Taiwan samples, the precise provenance study based on the coupled Nd and Sr isotopes is not possible at this stage. Sediments in most of southern SCS (western Province D) with $^{87}Sr/^{86}Sr$ (0.7124–0.7253) and εNd (−12.28 to −9.42) values (Wei et al., 2012) can be correlated to Mekong River sediments. However, coupled Nd and Sr isotopes from Borneo, the Malay Peninsula, and Sumatra are needed for reliable provenance analysis in the southern SCS. Although clay mineralogy is an efficient tracer for provenance study of terrigenous sediments in the SCS, especially in the northern SCS (Liu et al., 2008b, 2010b, 2010c), clay mineralogy coupled with Nd and Sr isotopes are helpful for improving further provenance analysis.

4. Modern source-to-sink transport process

The spatial distribution of clay mineralogy and geochemistry of surface sediments on the SCS seafloor and in surrounding drainage systems provides a macro-scale view of source-to-sink transport of fluvial sediments on time scales of years to tens of years. To evaluate the dominant transport processes based on these recently deposited surface sediments, a comprehensive comparison of the sediment distribution patterns with various current systems in the SCS is needed. Further to verify the resulting transport process, long-term in situ deep-water mooring observations including sediment and hydrology measurements are essential, and such investigations have recently been carried out in the northern SCS.

4.1. Transport process from shelf to abyssal basin

The spatial distribution of clay minerals throughout the SCS has a close relation to the current patterns (Fig. 12). In the northern SCS, relatively high contents (>40%) of smectite prevail in the region west of the Dongsha Islands, fitting well with the flow shift from the westward SCS Branch of Kuroshio to the northeastward SCS Warm Current (Figs. 12A and 13A). The SCS Branch of Kuroshio and SCS Warm Current generate numerous mesoscale westward-propagating eddies, which are frequently observed along the continental slope from the southwest of Taiwan to the west of the Dongsha Islands (Fig. 3). Smectite is likely transported by these eddies from the Luzon Strait westwards and then deposited on the slope and outer shelf (Liu et al., 2010b). The mesoscale eddies are detached as warm rings from the Kuroshio Current (Hu et al., 2000; Caruso et al., 2006; Yuan et al., 2006). The intrusion of the Kuroshio Current happens in the Luzon Strait, where chemically weathered smectite is accumulated from the Luzon arc system, discharged from Luzon rivers and/or transported northward through the NW Luzon Coastal Current (Fig. 13A). Therefore, smectite in the northern SCS seems to be transported mainly via the surface current (i.e., the SCS Branch of Kuroshio and the NW Luzon Coastal Current) under in the influence of the Kuroshio Current intrusion.

The spatial distribution of high contents of illite and chlorite in the northern SCS displays tongue-shaped patterns extending from Taiwan southwestward offshore along the continental shelf and the lower continental slope, respectively (Fig. 8B, D). Considering the similar distribution and high linear correlation of illite and chlorite (Fig. 7), we use illite + chlorite to show their combined distribution (Fig. 12B). The distribution belt with high illite + chlorite content at the 2000–2500 m water depth matches well with the SCS Contour Current, which is thought to flow southwestward along the lower continental slope off southeastern China (Fig. 3) (Qu et al., 2006). Most likely, the deep SCS Contour Current, which enters the SCS through the Luzon

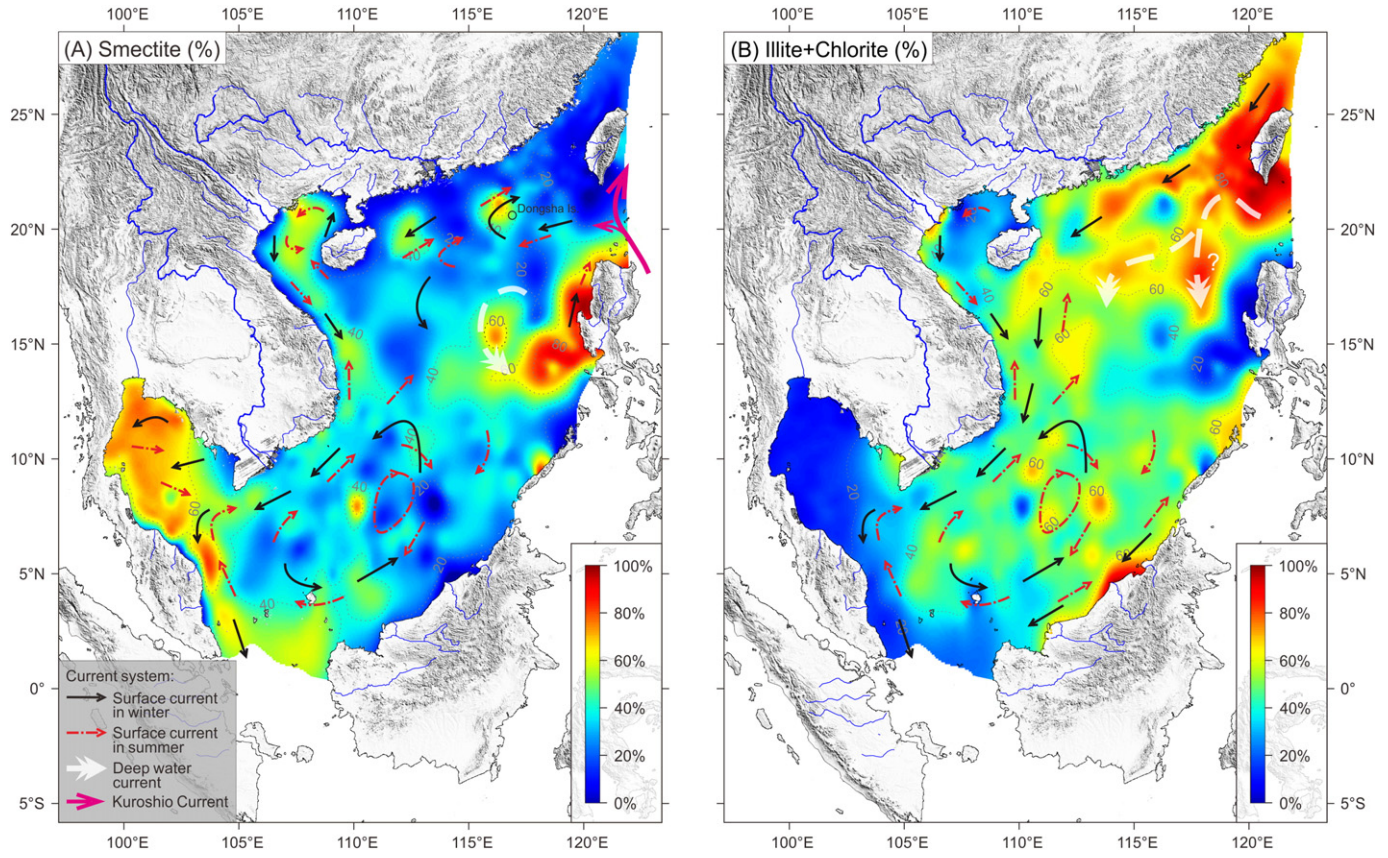

Fig. 12. Correlation of clay mineral distribution with current systems in the SCS. (A) Smectite (%). (B) Illite + chlorite (%). See Fig. 3 for all major surface and deep current systems.

Strait, transports Taiwan-sourced illite and chlorite southwestward along the lower continental slope (Fig. 13B). There is a belt of high content of illite + chlorite extending southward to the deep basin (Figs. 12B and 13B). We interpret this southern belt to have been transported by the bottom current, which is still to be confirmed by in situ observations. Another tongue-shaped distribution of high illite + chlorite content on the eastern continental shelf appears to be formed by the Guangdong Coastal Current in winter (Fig. 13B), because the winter monsoon is much stronger than the summer monsoon at present (Chu and Wang, 2003). Therefore, illite and chlorite in the lower continental slope and deep basin could be carried by the deepwater/bottom current, while on the shelf they could be mainly transported by the Guangdong Coastal Current during winter (Liu et al., 2010b).

In the eastern SCS, the distribution of high contents of smectite (>80%) extends from Luzon offshore westward to the abyssal basin of the central SCS (Fig. 12A). There is no westward-flowing current in the region to contribute to westward smectite transport from Luzon, although the Deep Cyclonic Current in the central deep SCS could affect the accumulation of smectite to a certain degree (Figs. 13A and 14A). Smectite could be formed easily from rapid chemical weathering of andesitic–basaltic rocks, and such volcanic activity frequently occurs on Luzon. One of the largest volcanic eruptions of the twentieth century, the 1991 eruption of Mount Pinatubo in Luzon, commenced on June 12 with a series of vertical and lateral blasts and culminated in a paroxysmal explosion on June 15. The fallout of Pinatubo tephra was recorded by fully automated sediment traps moored in 1190 m and 3730 m water depths in the central SCS (Wiesner et al., 1995, 2004). The tephra covers about 30% of the bathypelagic SCS in a westward-elongated lobe (Fig. 14B), reflecting the prevailing upper-level wind direction. The distribution of tephra thickness matches well the high content of smectite in the eastern SCS (Fig. 14B). We suggest that the tephra from volcanic eruptions in Luzon like Mt. Pinatubo or others could contribute to the formation of high smectite through chemical weathering on the seafloor. The potential in situ volcanic activities in the eastern SCS may also contribute to the formation of smectite. Nevertheless, to test or verify this hypothesis, further chemical analysis of clay minerals in the eastern SCS is needed to distinguish the authigenic smectite from the terrigenous species.

The transport pathway of clay minerals in the southern SCS is difficult to identify because of the relatively homogenized nature of sediments (Fig. 12). The widely distributed SCS Southern Cyclonic Gyre in winter and Southern Anticyclonic Gyre in summer occupy most of the southern SCS, even extending to the northern Sunda Shelf (Figs. 3 and 12). These reversed surface current systems could rapidly mix clay minerals from many of the surrounding drainage systems. Only a narrow belt of high illite and chlorite contents occurs in the coastal zone of North Borneo (Fig. 12B). Given the spatial distribution of εNd values in surface sediments, we suggest that fluvial sediments from Borneo are transported northward along the narrow belt once entering the sea. The slightly higher illite and chlorite contents off the Mekong River delta indicate southeastward transport of Mekong River sediments (Xue et al., 2010, 2014; Unverricht et al., 2014).

High surficial smectite contents (>60%) are found across the majority of the Gulf of Thailand and though to be controlled mainly by surface currents, which are anticyclonic in summer and cyclonic in winter (Fig. 12A). The distribution of smectite is restricted to the Gulf probably due to the strong surface circulations in the entrance region, suggesting that the exchange of clay minerals between the Gulf of Thailand and the southern SCS is very limited. Instead, clay minerals in the Gulf of Tonkin are easily transported to the western SCS via the passage in the south. A narrow belt with high contents of illite and chlorite extends from the mouth of the Red River to the south, suggesting the southward transport carried by the year-round cyclonic gyre (Fig. 12B).

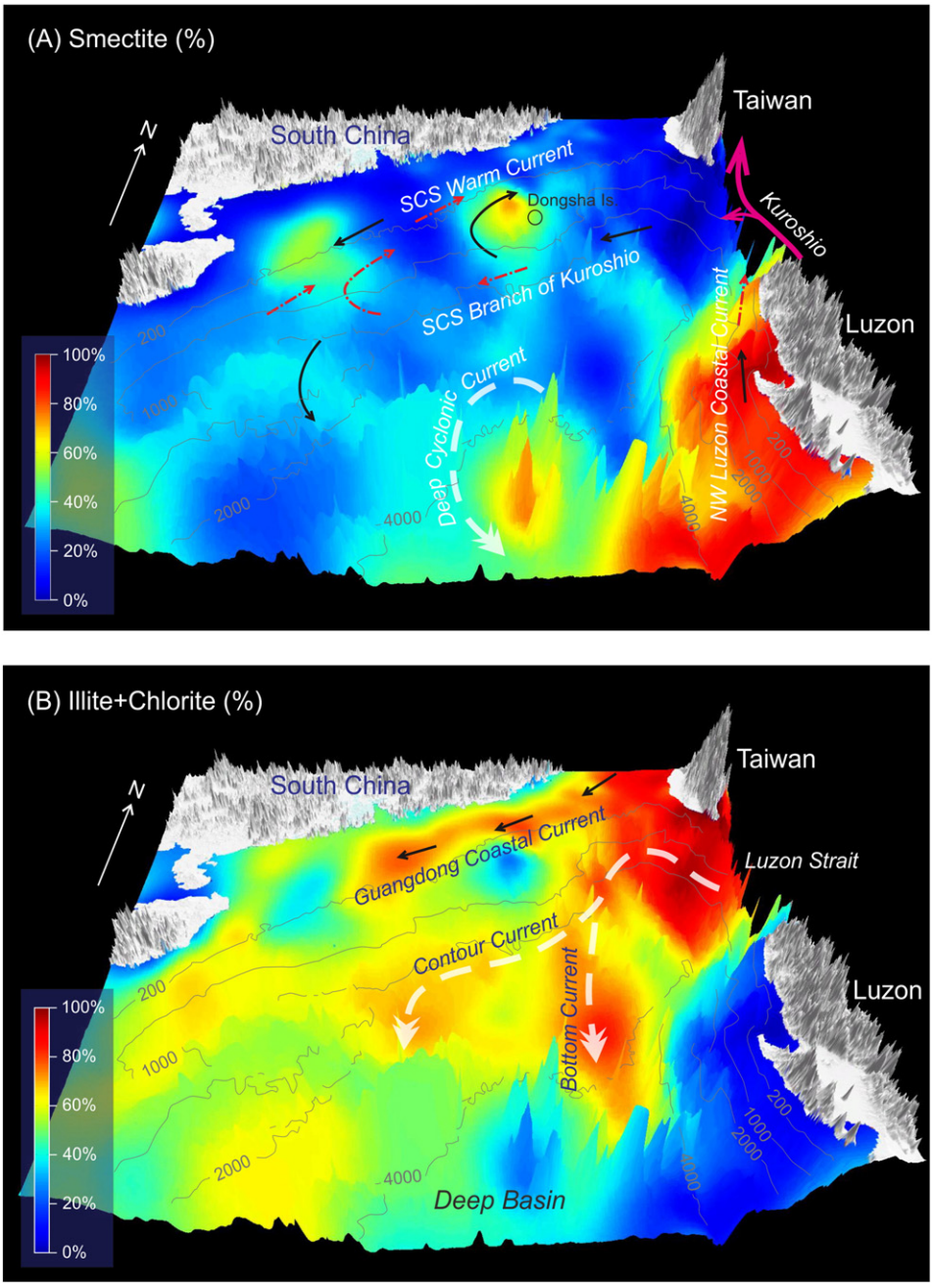

Fig. 13. Interpretation of spatial transport processes of the major clay mineral species in the northern SCS. (A) Smectite (%). (B) Illite + chlorite (%). The maps are created using the three-dimensional topography with overlays of clay mineral distribution (%). Isobath curves of 200, 1000, 2000, and 4000 m are indicated to show the seafloor configuration.

As indicated, the distribution of high content of kaolinite in the coastal zones of South China, Vietnam, and the Malay Peninsula (Fig. 8C) is regarded as the result of differential settling. Such elongated muddy deposits on the continental shelf are also believed to have formed from westward or southward transport of fluvial sediments (Liu et al., 2009a). Recent shallow seismic investigations confirm that sediments dispersed from the Pearl River drainage system accumulate in the coastal zone extending from the estuary southwestward to the Leizhou Peninsula (Ge et al., 2014). Therefore, the dilution of kaolinite by illite and chlorite from Taiwan and smectite from Luzon may be another factor affecting the observed sediment characteristics. The consequent dilution effect is thought to be strong enough to confine the distribution of kaolinite to the Pearl River offshore even without the differential settling (Liu et al., 2010b). A quantitative evaluation of the dilution effect on the continental shelf off South China indicates mixing of 52% detrital fine-grained sediments derived from the Pearl River, 29% from Taiwan, and 19% from Luzon (Liu et al., 2008b). The dilution effect scenario is very similar to the interpretation of clay mineral transport on the Brazilian continental shelf, resulting from mixing of Amazon sediments with other source materials (De Morais et al., 2006).

4.2. Mooring-observed deepwater transport process

To confirm and verify the modern source-to-sink transport process of fluvial sediments recorded on the seafloor, long-term deepwater mooring observations at some typical locations in the SCS have been made. Concerning the unique role of western Pacific water in controlling SCS circulation, we focus attention on the northeastern SCS as

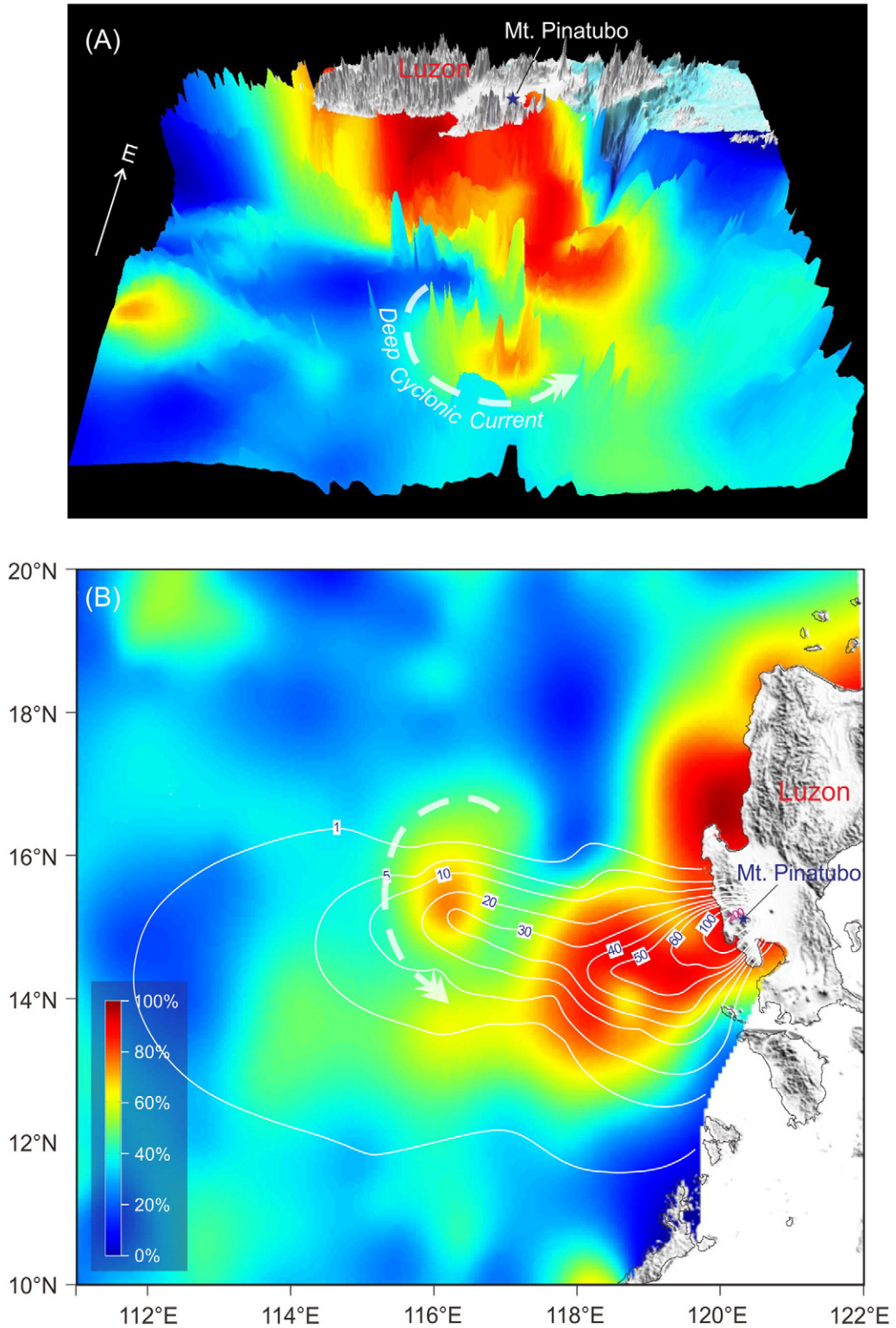

Fig. 14. Interpretation of the spatial distribution of high smectite content in the eastern SCS. (A) Distribution of smectite (%) on the three-dimensional topography map and correlation with the Deep Cyclonic Current (note: this map is looking eastward). (B) Planar distribution of smectite (%) mapped on a same location area with A. Thickness contours (white fine lines with values in mm) of the June 15, 1991 Mt. Pinatubo ash fall deposit (Wiesner et al., 2004) are superposed for comparison.

Fig. 15. Recent mooring observation systems in the SCS. (A) Topography of the northeastern SCS and locations of the mooring systems. D1 and D2 from Chang et al. (2010); BI from Tian and Qu (2012); C6, C7, and C8 from Zhang et al. (2013); TJ-A-1 from Zhang et al. (2014); BC and LT from Zhou et al. (2014). WG2 and WG3 are the two primary gaps on the Heng-Chun Ridge. The pathways of the deep Pacific water through the Luzon Strait entering into the SCS are labeled by the yellow arrows from Zhao et al. (2014). (B) Vertical structure of the TJ-A-1 full-water column mooring system (Zhang et al., 2014). (C) Map of sea level anomaly (SLA) with surface geostrophic current velocity (shown as black arrows) on 15 February 2012, showing that an anticyclonic mesoscale eddy passed by the mooring site (white star). Centroidal tracks of two eddies moving southwestward from birth ("B") until death ("D"), marked every 3 days (circles), are superimposed on the map. Red circles stand for an anticyclonic eddy born in November 2011; green circles represent an anticyclonic eddy born in November 2012. The inset figure in the lower part of (C) shows the u (along-slope) and v (cross-slope) coordinates (Zhang et al., 2014).

well as the Luzon Strait, where more measurements have been carried out recently to investigate deep circulation and sediment transport dynamics (Fig. 15A). The most widely accepted view is that the variability of the deep SCS circulation arises from deep western Pacific water mass transport through the Bashi Channel associated with strong overflow. In order to investigate the water exchange below 2000 m through two

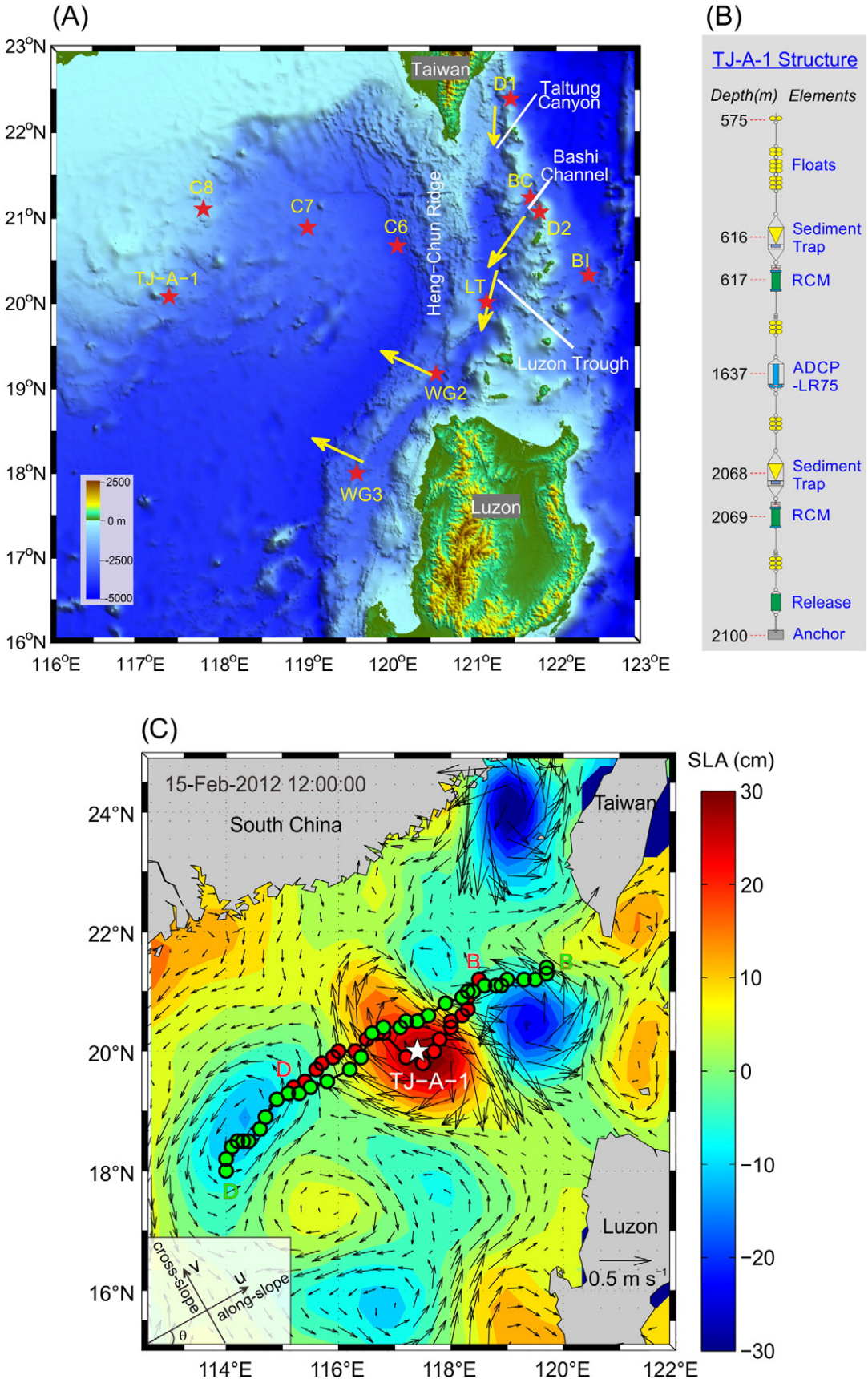

different channels connecting the SCS and the western Pacific, two near-bottom moorings equipped with a pair of RCMs (Recording Current Meters) were deployed in the Taltung Canyon (shown as D1 in Fig. 15A) and the Bashi Channel (shown as D2 in Fig. 15A) for about 9 months (Chang et al., 2010). The measurements show that the low-passed filtered current (tidal currents removed) in the Bashi Channel, with an average range of 17–30 cm s^{-1}, was much stronger than that in the Taltung Canyon at a similar depth, with an average range of 0.8–4 cm s^{-1}. Thus, Chang et al. (2010) argued that the Bashi Channel plays a more prominent role in funneling deepwater from the western Pacific to the SCS, at a remarkable rate of 1.06 ± 0.44 Sv (1 Sv = 10^6 m^3 s^{-1}). Zhao et al. (2014) combined moored and modeled results with ship-based hydrodynamic measurements to give a remarkably detailed picture of the deepwater flow pathways in the Luzon Strait. Their results suggest that the overall mean transport of the deep Pacific water flowing into the Luzon Strait is about 1.5 Sv, of which 1.2 Sv is through the Bashi Channel (consistent with the value of Chang et al., 2010) and 0.4 Sv through the Taltung Canyon, respectively (Fig. 15A). This water enters the Luzon Trough and ultimately flows into the SCS through two primary gaps on the Heng-Chun Ridge around stations WG2 and WG3 shown in Fig. 15A, with a mean transport of 0.7 and 0.9 Sv, respectively.

To understand the linkage between the Pacific western boundary current in the Philippine Sea and deep SCS circulation through the complex topography of the Luzon Strait, a mooring system was deployed at 2950 m (~120 m above the bottom) off eastern Bataan Island (shown as BI in Fig. 15A) between August 2010 and April 2011 (Tian and Qu, 2012). Based on a time-series of near-bottom current velocity obtained by a RCM at the mooring system, it was found that the meridional velocity with average magnitude of 8 cm s^{-1} dominates in the region east of Bataan Island, exhibiting a notable seasonal variation in current directions flowing southward in summer and northward in winter. However, the shift of seasonal directions does not fit with the westward sediment transport direction argued by Lüdmann et al. (2005). A temporal variation of the deep overflow spanning a scale from 30 to 60 days was revealed in the Taltung Canyon and the Bashi Channel (Chang et al., 2010). Further observation also indicates similar results with current speeds of ~23 cm s^{-1} and intraseasonal variations of the deep overflow obtained by two mooring systems in the Bashi Channel and the Luzon Trough (shown as BC and LT in Fig. 15A) (Zhou et al., 2014). Both the surface- and deepwater-generated eddies were considered to be the most likely mechanism for the intraseasonal variations of the deep overflow in the Luzon Strait (Chang et al., 2010).

The southwest-propagating eddies frequently generated southwest of Taiwan have been confirmed to intensify the deep current velocity and result in large temperature variations at a series of deepwater moorings in the northeastern SCS (Zhang et al., 2013, 2014). As documented in Zhang et al. (2013), the magnitude of the deep current velocity was enhanced up to twice the value without eddies based on three near-bottom moorings deployed in the northeastern SCS (shown as C6, C7, and C8 in Fig. 15A). The deep currents also flowed in opposite directions during the eddy events. A more integrated full-water-column mooring system was designed to explore the eddy-induced influence on deepwater sediment dynamic processes (shown as TJ-A-1 in Fig. 15A) (Zhang et al., 2014). The TJ-A-1 mooring system was deployed at 2100 m on the northeastern SCS continental slope for nearly two consecutive years from September 2011 to May 2013. Equipped with an Acoustic Doppler Current Profiler (ADCP), RCMs, and sediment trap systems (Fig. 15B), the mooring system yielded a continuous time-series of current velocity, temperature, suspended-sediment concentration (SSC), and sediment particle samples. Combined with high-resolution sea surface level anomaly (SLA) fields, two anticyclonic eddies with a highly nonlinear character crossed the mooring station (Fig. 15C). Both eddies originated southwest of Taiwan and propagated southwestward at a mean speed of 10 cm s^{-1} (Zhang et al., 2014). The influence of eddies is evident from the simultaneous variations in the SLA (Fig. 16A) and along-slope current velocity (Fig. 16B, C) when the mesoscale eddies passed through. During the passage of the two eddies, the amplitude of the current velocities at depth was almost twice the normal values and the direction shifted from northwestward to southeastward (Zhang et al., 2014) (Fig. 16B). This finding is consistent to the results revealed by the C6 mooring (Zhang et al., 2013).

More comprehensively, the TJ-A-1 mooring system recorded two periods with dramatic increases in the near-bottom SSC (Fig. 16D) which corresponded to periods of anomalous velocities induced by the eddies. During the first anticyclonic eddy whose center crossed TJ-A-1, the increase in SSC lasted 1.5 months from 1 February to 10 March 2012, and the SSC was enhanced about sixfold with a mean value of 1.2 mg l^{-1} compared to the background value of 0.2 mg l^{-1}. Two similar enhanced SSC events occurred during the second anticyclonic eddy, whose southern edge crossed the mooring station with a mean value of 1.2 mg l^{-1} and 2.8 mg l^{-1}, respectively. Correspondingly, the distinct increase of sediments collected by the near-bottom sediment trap on this mooring further illustrates the eddy influence on sediment transport (Fig. 16E). However, the duration of the enhanced SSC induced by the second eddy was much shorter than the first. Various time lags between enhanced SSC near the bottom and the SLA at the surface were found: 12 days when the first eddy and 29 days when the second eddy passed through, respectively, indicating the complex deepwater dynamic responses to the passing eddies (Zhang et al., 2014). The high nonlinearity of these two anticyclonic eddies allows them to trap and transport water and sediment along their tracks. According to the clay mineral analysis, the suspended sediments at the TJ-A-1 mooring station included high contents of illite and chlorite terrigenous particles reaching up to 59 ± 5%. Therefore, the enhanced suspended sediment load is interpreted to have been trapped and transported from southwest Taiwan along the slope to the northeastern SCS by the mesoscale eddies. The total net southwestward sediment transport driven by these two eddies was estimated at about 1.05 Mt (Fig. 16F), amounting to ~2% of the total annual sediment discharge from southwestern Taiwan rivers. The results presented by the TJ-A-1 mooring system provide observational evidence for deepwater hydrodynamic and sediment transport processes driven by mesoscale eddies and imply that the eddies are able to transport large amounts of sediments derived from the neighboring source areas and then release them in the SCS deep basin.

5. Source-to-sink transport variability during Late Quaternary glacial cycles

The modern source-to-sink transport processes of fluvial sediments in the SCS could have been much different during Late Quaternary ice ages when the global sea level stood ~100 m lower than present (Fig. 17). Cold and arid climatic conditions in the glacial periods could have greatly affected fluvial sediment input into the SCS. Sea level fall would have resulted in a remarkable seaward extension of river mouths, and the wide continental shelf was mostly exposed, accelerating erosion by incision of river valleys to the lowered base level (Fig. 17B). Surface and deepwater circulation patterns could also have been altered by the change in the land–sea configuration. The East Asian winter monsoon was stronger during the glacial periods than today, likely resulting in more intense physical denudation in the surrounding drainage systems. Clay mineralogy can be a powerful tool to document changes of climatic and oceanographic condition in the SCS over the Late Quaternary glacial–interglacial variation (Liu et al., 2004, 2007c, 2010b). Herein, clay mineralogical data from six high-quality sediment cores in the northern, western, and southern SCS are synthesized to illustrate temporal variations in the terrigenous sediment provenance, and thus, transport processes and their applications to the East Asian monsoon evolution. Furthermore, a semi-

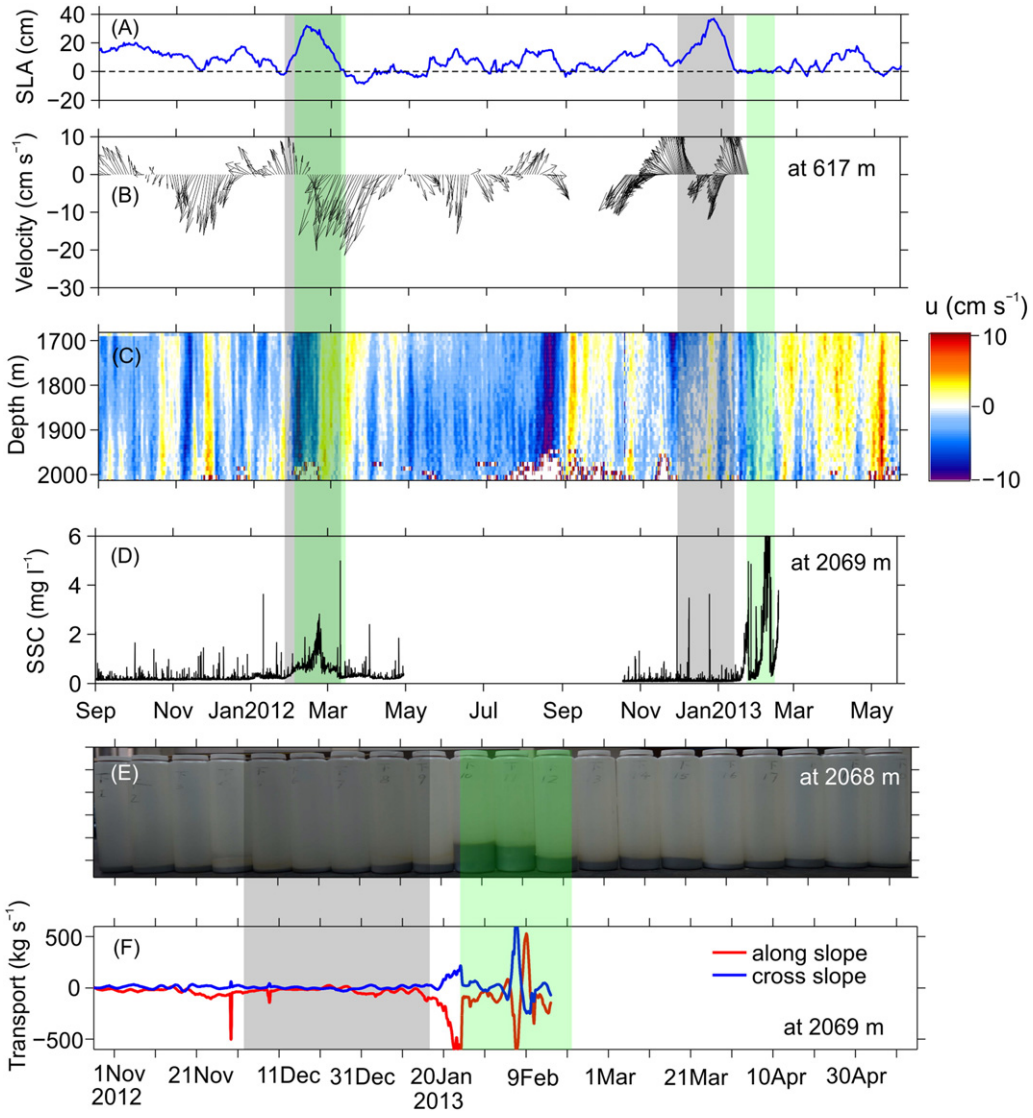

Fig. 16. Time series measurements obtained from the TJ-A-1 mooring system (modified after Zhang et al., 2014). This dataset shows responses to two anticyclonic eddies passing-through the study area from September 2011 to May 2013. (A) SLA (sea level anomaly). (B) Current velocity at 617 m obtained by the upper RCM (Recording Current Meter). (C) Along-slope current velocity profile obtained by a long-range ADCP (Acoustic Doppler Current Profiler). (D) Near-bottom SSC (suspended sediment concentration) at 2069 m (~31 m above the seafloor) obtained by the lower RCM. (E) Bottled sediment samples collected by the lower-layer sediment trap positioned at 2068 m during the second deployment (November 2012 to May 2013). (F) Sediment transport mass estimated from SSC and corresponding near-bottom velocities during the second deployment (November 2012 to May 2013). Shaded regions show the periods when two energetic eddies passed through the mooring site (gray) and the periods with enhanced SSC near the seafloor (green) following the eddy activities. It is noted that the lower-layer sediment trap during the first deployment (September 2011 to October 2012) failed in the operation, and no bottled sediment samples are available when the first eddy passed through; (E) and (F) show only the results of the bottled sediments corresponding to the second anticyclonic eddy.

quantitative study of sediment contributions from various provenances surrounding the northern SCS since the last glaciation is conducted to evaluate source-to-sink transport process of fine-grained fluvial sediments.

5.1. Glacial–cyclic terrigenous input

Time series variations in Quaternary clay mineral assemblages in the SCS usually represent glacial–interglacial cyclicity, with high illite and chlorite contents during glacial periods and high smectite content during interglacial periods, and they are interpreted either as chemical weathering closely related to contemporaneous climatic changes of source areas or as oceanic current transport (Liu et al., 2003, 2004; Wan et al., 2007). However, high-resolution studies of the clay mineralogy do not always show such a glacial–interglacial cycle, and sediment transport patterns are revealed to be quite different between various parts of the SCS, suggesting the complexity of terrigenous input from the surrounding drainage systems and related transport process during the geological past (Boulay et al., 2005).

In the northern SCS, high-resolution clay mineral assemblages of Core MD05-2904 and ODP Site 1145 in the Late Quaternary are dominated by illite, smectite, and chlorite, with only a minor proportion of kaolinite (Boulay et al., 2005; Liu et al., 2010c). The coupled provenance supply and oceanic current transport are considered as the major factors controlling temporal variations of the clay mineral compositions rather than glacial–interglacial cyclicity. The smectite/(illite + chlorite) ratio is used to reflect the relative contribution of clay minerals from major provenances of Taiwan and Luzon and to evaluate the transporting capability of different oceanic currents (Fig. 18) (Liu et al., 2010c). There are two primary factors that affect the provenance supply from

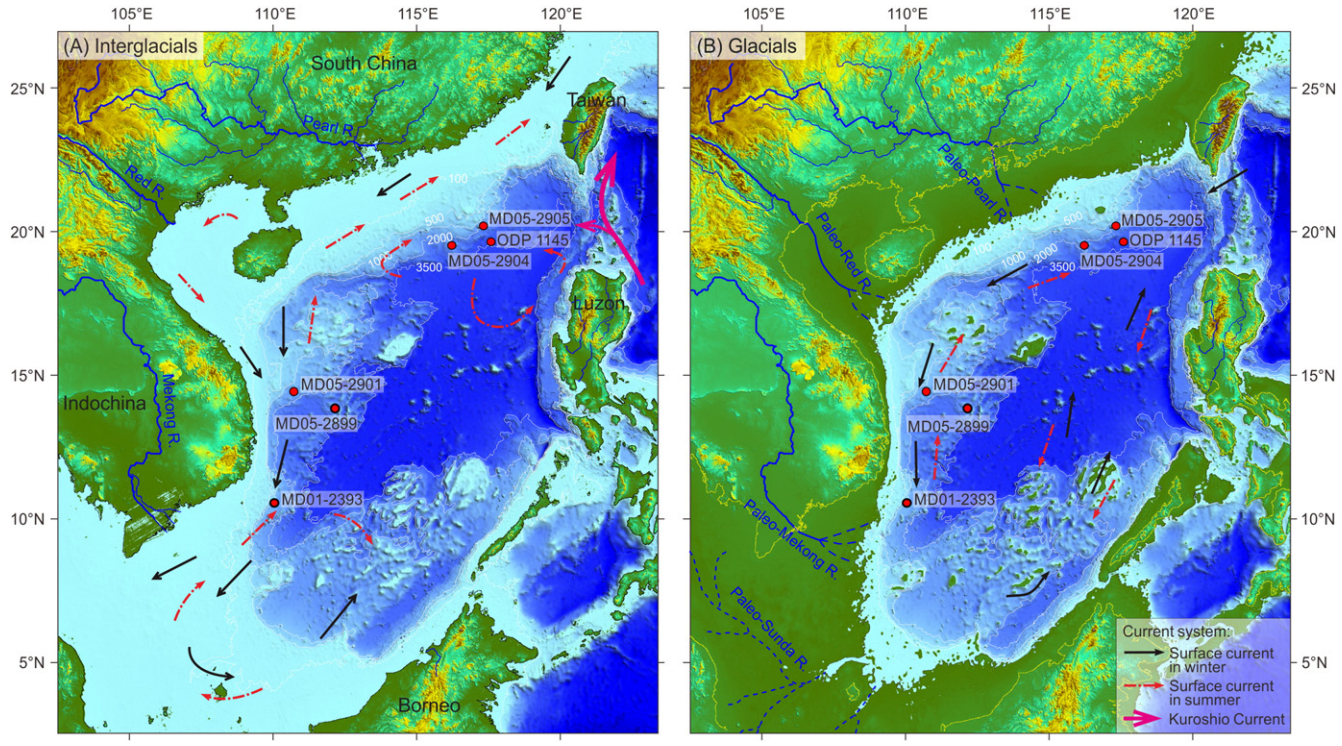

Fig. 17. Geographical configurations of the SCS between interglacial and glacial periods. (A) Interglacials: the coastline is approximately the present one; the current systems are simplified from Fig. 3. (B) Glacials: the coastline was moved to the approximate position of present 100 m isobaths (the present coastline is shown in yellow); the Kalimantan Strait and the Taiwan Strait were closed; the Gulf of Thailand, the Gulf of Tonkin, and other large areas of the continental shelf were exposed; surrounding fluvial drainage systems were extended seaward as paleo-river systems (e.g., the Paleo-Pearl River, the Paleo-Red River, and Paleo-Mekong River) with the Paleo-Sunda River system developed on the exposed Sunda Shelf. Surface current systems during the glacial periods were cyclonic during winter and anticyclonic during the summer (Wang et al., 1995). Locations of six cores used in this study are indicated: ODP Site 1145 (19°35.04′E, 117°37.86′N, water depth 3175 m), Core MD05-2904 (19°27.32′E, 116°15.15′N, water depth 2066 m), and Core MD05-2905 (20°08.17′E, 117°21.61′N, water depth 1647 m) in the northern SCS; Core MD05-2901 (14°22.50′N, 110°44.60′E, water depth 1454 m) and Core MD05-2899 (13°47.66′N, 112°10.89′E, water depth 2393 m) in the western SCS; Core MD01-2393 (10°30.15′N, 110°03.68′E, water depth 1230 m) in the southern SCS.

Taiwan and Luzon to the northern SCS. The first is the steep seafloor topography offshore the two islands in the northeastern SCS, resulting in very narrow continental shelves between river mouths and continental slopes, where the short sediment transport distance is largely unaffected by glacioeustasy (Liu et al., 2010c). The second is the tectonic uplift- and typhoon rainfall-controlled sediment discharge from the two islands, also independent of glacial–interglacial variations (Liu et al., 2008b, 2009b). In Taiwan, the illite- and chlorite-dominated primary clay mineral assemblage indicates mostly the intensity of physical denudation. Similarly in Luzon, the huge amount of smectite reflects the fast hydrolysis of andesitic–basaltic source rocks and the prompt delivery toward the sea. Therefore, relative contributions of Luzon versus Taiwan, as indicated by the smectite/(illite + chlorite) ratio, reflect the variations in sediment transporting capability of surface versus deep currents in the northeastern SCS (Liu et al., 2010b). However, evolution of the intensities of these currents in the Late Quaternary glacial–interglacial cycles remains unclear owing to insufficiency of related studies, making it difficult to interpret the high-frequency oscillations in the smectite/(illite + chlorite) ratio (Fig. 18). Enhanced eolian input from the Asia's dry interior during the Late Quaternary was proposed by previous investigations based on grain size analysis (Wang et al., 1999; Tamburini et al., 2003). However, further studies using end-member modeling of grain size data, clay mineralogy, and Nd and Sr isotopes concluded that the eolian supply is a minor component of sediments for the SCS including the glacial stages during the Quaternary (Liu et al., 2003; Boulay et al., 2005, 2007).

Similarly, clay minerals in the western SCS are also derived from various sources. Illite and chlorite are mostly provided by the Mekong and Red rivers (Liu et al., 2007c). Both rivers have undergone strong physical denudation in their upper reaches of the eastern Tibetan Plateau owing to the young uplift related tectonic activities, forming illite- and chlorite-dominated clay assemblage (Liu et al., 2007b). Clayey sediments that enter the SCS from the Pearl River are thought to be carried westward by the Guangdong Coastal Current, bringing the kaolinite-rich clay assemblage to the areas off Hainan Island (Fig. 8C). These sediments can be brought further southward to the western SCS by the cyclonic surface currents in winter. Therefore, the kaolinite/(illite + chlorite) ratio at Cores MD05-2901 and MD05-2899 from the western SCS is employed to study the relative contribution from the northern and southern sources. The kaolinite/(illite + chlorite) ratio at both cores indicates strong glacial–interglacial cycles, with high values in glacial periods and lower values in interglacial periods (Fig. 18; Liu et al., 2007c). This pattern can be explained by the alternation of surface current systems in the western SCS between the glacial and interglacial stages (Liu et al., 2007c). In interglacial periods, driven by the enhanced summer monsoon, the western SCS is dominated by the northward warm surface current, delivering abundant illite and chlorite from the Mekong River to the western SCS. Illite and chlorite from the Red River and kaolinite from the Pearl River are of minor importance in terms of their contribution, because the northward surface current could prevent them from southward transport. In glacial periods, sea-level fall caused the Pearl River mouth to move southward, and the amounts of kaolinite reaching the deep basin increased in the western SCS (Liu et al., 2010c). Meanwhile, surface circulation in the western SCS was dominated by the southward current during the glacial periods, which is similar to the present-day circulation during winter (Fig. 3). Clayey sediment in the western SCS was thus dominated by kaolinite input delivered by this southward-directed surface current,

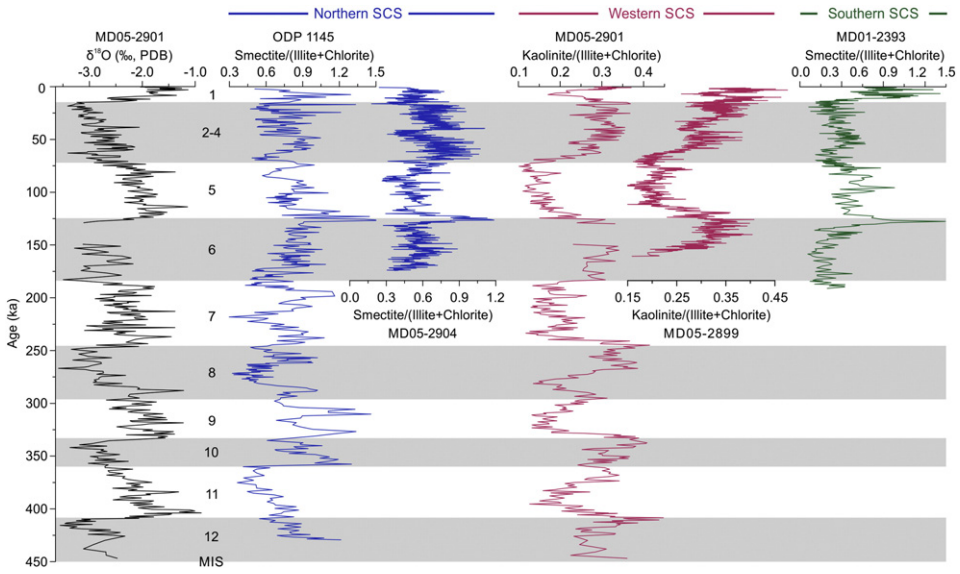

Fig. 18. Comparison of clay mineralogy proxies for fluvial sediment transport and inferred East Asian monsoon evolution during the Late Quaternary in the northern, western, and southern SCS. Clay mineralogical data of ODP Site 1145 from Boulay et al. (2005), Core MD05-2904 from Liu et al. (2010c), Core MD05-2901 from Liu et al. (2007c), and Core MD01-2393 from Liu et al. (2004).

and illite and chlorite from the Red and Mekong rivers were of minor importance. As a result, the clay mineral assemblage in the western SCS reflects mostly variations in the prevailing surface current under the influence of monsoon winds. High values of kaolinite/(illite + chlorite) ratio in Cores MD05-2899 and MD05-2901 during glacial periods indicate increased Pearl River-originated input driven by enhanced winter monsoon, while low values of kaolinite/(illite + chlorite) ratio during interglacial periods indicate increased Mekong River-originated input driven by enhanced summer monsoon (Liu et al., 2007c).

The southern sector of the SCS today is fed by terrigenous sediments from two nearby sources, the Sunda Shelf and the Mekong River. Sediments on the Sunda Slope are reported mainly from northward transport from the Sunda Shelf (Steinke et al., 2008; Zhao et al., 2011). Clay mineral changes in the past 17,000 years in this region mostly reflect the landward retreat of the coastline induced by the gradual rise of sea level (Steinke et al., 2008). However, sediment cores are too short to reveal the secular changes of clay minerals in the Late Quaternary glacial–interglacial cycles. Core MD01-2393 is located close to the Mekong River mouth, and the overwhelming majority of sediments in this core come from the Mekong River (Liu et al., 2004, 2005). Clay mineralogical variations in this core reflect mainly environmental changes in the Mekong River drainage system (Liu et al., 2004). The high content of smectite in Core MD01-2393, much higher than in the riverine samples of the Mekong River, probably results from the preferential settling of other clay species, especially kaolinite, upon entering the southern SCS. During cold and dry glacial periods, production of illite and chlorite in the Mekong drainage system was increased due to the strengthened physical erosion. During interglacial periods, smectite content in Mekong River sediments becomes higher when the Indochina Peninsula is more hydrated by the increased summer monsoon rainfall. The smectite/(illite + chlorite) ratio at Core MD01-2393 thus reflects the glacial–interglacial variations of clay mineral composition of the Mekong drainage system. High values of smectite/(illite + chlorite) ratio in the interglacial periods indicate the preferential formation of smectite in the Mekong drainage as a result of increased summer monsoon rainfall, while low values of smectite/(illite + chlorite) ratio in the glacial periods indicate increased erosion of illite and chlorite owing to the strengthened physical denudation.

5.2. Quantitative evaluation of Late Pleistocene to Holocene variability

The data presented above allow a high-resolution, quantitative reconstruction of transport processes in the northern SCS using the characteristic end-members in clay mineral compositions from three major provenances, i.e., major kaolinite and moderate illite and chlorite from the Pearl River, dominant illite and chlorite from Taiwan, and smectite from Luzon (Liu et al., 2008b). Two high-quality piston sediment cores are used to quantitatively reconstruct source-to-sink transport processes since the last glaciation.

Cores MD05-2904 and MD05-2905 are located at 2066 m and 1647 m water depth on the lower slope of the northeastern SCS, respectively (Fig. 17). They are situated in the tongue-shaped belt with high contents of illite and chlorite, which are expected to derive mainly from terrigenous input of Taiwan. High-resolution planktonic foraminifera oxygen isotope stratigraphy combined with AMS ^{14}C dates of both cores confirms their excellent quality with high sedimentation rates (average 17.5 cm/ka for Core MD05-2904 and 52.3 cm/ka for Core MD05-2905) for the last 28 ka (Yang, 2008; Ge et al., 2010). Clay mineral data provide high temporal resolution, at time intervals of 86 years for Core MD05-2904 and 44 years for Core MD05-2905. These Late Quaternary sedimentation rates allow for the investigation of multi-century-scale variations of terrigenous input and related paleoenvironmental implications.

The clay mineral assemblage of Core MD05-2904 consists of dominant illite (29–48%) and smectite (13–45%), with less abundant chlorite (17–28%) and kaolinite (6–14%) (Fig. 19A). No glacial–interglacial change is observed from their temporal variations, but a strong shift at around 16 ka BP occurs for four clay mineral species and illite crystallinity, including a decrease in smectite content from an average of 36% during the early stage (28–16 ka BP) to 30% in the late stage (16–0 ka BP) and an increase in illite content from an average of 34% during the early stage to 39% in the late stage. The kaolinite content is much lower overall, ranging from 6 to 14%, and reaches the highest value of 14% at around 16 ka BP; similarly, the illite crystallinity reaches higher values of about 0.20°Δ2θ at around 16 ka BP in contrast to earlier or later values of about 0.18°Δ2θ, implying that more illite was derived from the source area with the intensive chemical weathering (Fig. 19A). By comparison, the clay mineral assemblage of Core MD05-2905

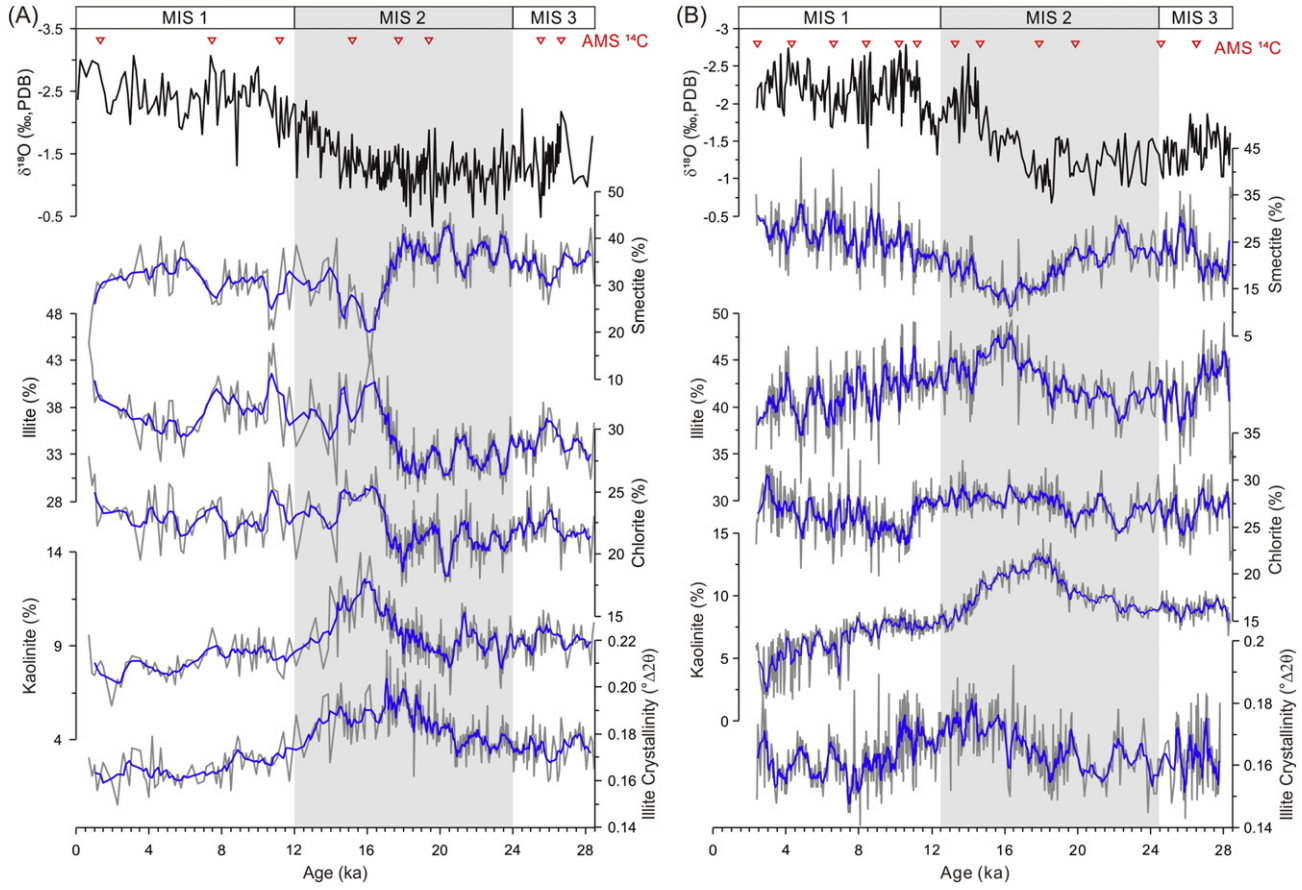

Fig. 19. High-resolution clay mineral assemblages since 28 ka BP during the last glacial period at Cores MD05-2904 and MD05-2905 on the lower slope of the northern SCS. (A) Core MD05-2904 (Liu et al., 2010c), with an average of 86 years temporal resolution from a total of 320 samples (2–4 cm sampling resolution). (B) Core MD05-2905 (Li et al., under review), with an average of 44 years temporal resolution from a total of 600 samples (2 cm sampling resolution). Planktonic foraminifera $\delta^{18}O$ stratigraphy and AMS ^{14}C dates (red triangles) of Cores MD05-2904 and MD05-2905 are from Ge et al. (2010) and Yang (2008), respectively. Clay mineralogical data are smoothed with a five-point running average in order to obtain more general variation trends.

contains more illite (32–49%) and chlorite (20–33%), less smectite (9–43%), and similar kaolinite (2–15%) (Fig. 19B). Their temporal variations do not present any clear glacial–interglacial changes either, but similarly show a shift of most clay mineral species and illite crystallinity at around 16 ka BP: decrease in smectite content from an average of 24% during the early stage to 15% at around 16 ka BP and then increase to 25% in the late stage; increase in illite content from average 42% during the early stage to 47% at around 16 ka BP; very low kaolinite content ranging from 3 to 13%, and reaching the highest value of 13% at around 16 ka BP (Fig. 19B).

Throughout the Late Quaternary glacial–interglacial cycles, South China, Taiwan, and Luzon are still the major sediment source areas, i.e., smectite deriving from Luzon, kaolinite from South China, and illite and chlorite originating from both South China and Taiwan (Liu et al., 2010c). A linear separation method is utilized to divide the illite and chlorite from South China and Taiwan by adopting the measured values of illite crystallinity at Cores MD05-2904 and MD05-2905, and average values from the two provenances (0.224°Δ2θ for South China and 0.155°Δ2θ for Taiwan, respectively) (Liu et al., 2010c; Li et al., under review). In this way, the illite contribution ratio of South China versus Taiwan with time is obtained. This ratio is applied to represent the sum of illite and chlorite from the two provenances because of their linear correlation for all samples of seafloor and surrounding drainage systems (Fig. 7). Therefore, a quantitative calculation of contributions from various provenances can be determined: the smectite content indicates the contribution from Luzon, the kaolinite content plus the part of illite and chlorite contents linearly separated by illite crystallinity stands for the contribution from South China, and the other part of illite and chlorite content shows the contribution from Taiwan (Liu et al., 2008b, 2010c).

The time-series quantitative evaluation of clay mineral contribution from major provenances of Luzon, Taiwan, and South China to Cores MD05-2904 and MD05-2905 is obtained since 28 ka BP in the last glaciation (Fig. 20). The contributions from the same provenance to two different sites can be compared by similar variation trends but different amplitudes, potentially referring to different distances of two sites to the fluvial systems of that provenance (Fig. 17). The contributions from Luzon at two cores display a similar pattern, remaining at 22–35% during late marine isotope stage (MIS) 3 to early MIS 2, with a significant decrease started in middle MIS 2 (~22.5 ka BP), reaching the lowest values of 12–21% at 16.5 ka BP coincident with the timing of H1 event (Heinrich Event 1) (Wang et al., 2001; Partin et al., 2007), and then increasing until it reached the Holocene level of about 25–30% (Fig. 20C, D). In contrast to Luzon, the contribution from Taiwan was relatively steady at an average value of ~61% in Core MD05-2905 (Fig. 20E), whereas Core MD05-2904 reveals rapid fluctuations with large amplitude (ranging from 43 to 77%) throughout the record, i.e., a gradual decrease (45–25%) during early–mid MIS 2 and then a slow increase (25–58%) until the Holocene (Fig. 20F). The South China contribution in both cores exhibits synchronous variations through time, increasing from constant values of 10–20% between 28.5 and 20 ka BP, with a significant high level (30–40%) during early

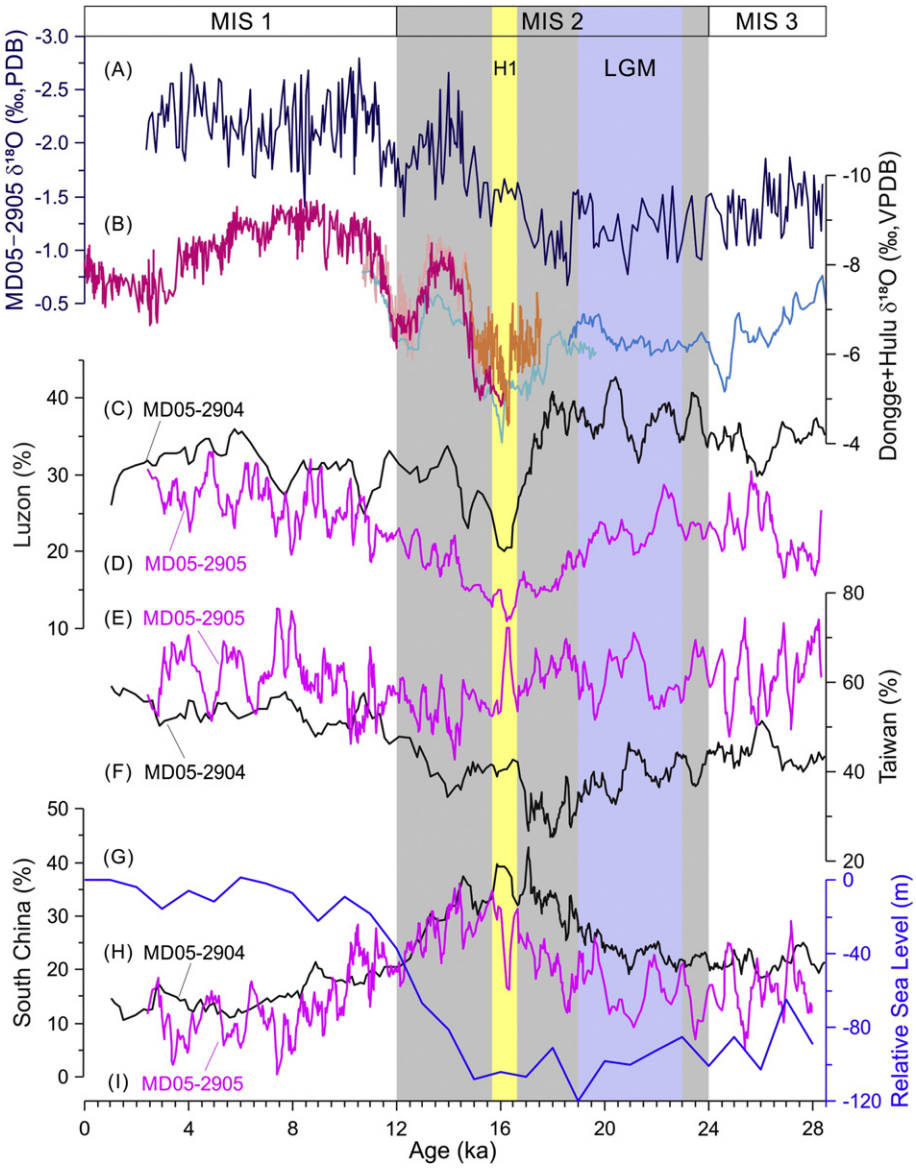

Fig. 20. Time series variations in fine-grained terrigenous contributions from major provenances of Luzon, Taiwan, and South China to Cores MD05-2904 and MD05-2905 in the northern SCS (modified after Li et al., under review). (A) Planktonic foraminiferal $\delta^{18}O$ record of Core MD05-2905 (Yang, 2008). (B) $\delta^{18}O$ of Hulu cave stalagmites (multi-colored) (Wang et al., 2001). (C) Luzon contribution to Core MD05-2904. (D) Luzon contribution to Core MD05-2905. (E) Taiwan contribution to Core MD05-2905. (F) Taiwan contribution to Core MD05-2904. (G) Relative Sea Level changes (Shackleton, 1987). (H) South China contribution to Core MD05-2904. (I) South China contribution to Core MD05-2905. Blue and yellow bars show the Last Glacial Maximum (LGM) and Heinrich 1 (H1) events, respectively.

stage of the last deglaciation and then a decrease to relatively low values (5–15%) (Fig. 20H, I) during the Holocene. The quantitative provenance evaluation shows that Taiwan is definitely the most important source (40–60%) of fine-grained terrigenous material to the northern SCS, while Luzon and the Pearl River serve as subordinate sources supplying 20–40%, and 15–25%, respectively. Despite the limitations of using percentage values in a three-variable system (the three provenance regions), with increasing contributions from one provenance when another provenance source decreases, this is still a significant approach for quantifying source-to-sink transport.

The westerly Core MD05-2904 received ~40% detrital material from Taiwan during the last glacial period, which increased to 55% during the Holocene (Fig. 20F), in comparison to the easterly Core MD05-2905 with a relative steady level of 60% (Fig. 20E), indicating that the deep-water circulation has increased during the Holocene. The enhanced deepwater transport ability allows for more Taiwan-derived material to be carried to the westerly slope. The Luzon contribution in both cores shows a good correlation with the Kuroshio Current intensity record in the Japan Sea (Sawada and Handa, 1998) and stalagmite $\delta^{18}O$ records in North Borneo (Partin et al., 2007), implying a potential hydrological impact from the tropical regions. Dry conditions evaluated from stalagmite $\delta^{18}O$ records suggest a tropical Pacific hydrological response to the ITCZ shift during H1 (Wang et al., 2001; Partin et al., 2007), which in turn may have affected the intensity of Kuroshio Current in the northern Pacific, resulting in a great reduction of terrigenous contribution from Luzon to the northern SCS (Fig. 20C, D). The overall South China terrigenous input to Core MD05-2904 (Fig. 20H) is ~10% larger than to Core MD05-2905 (Fig. 20I), which is reasonable, because Core MD05-2904 is located closer to the Pearl River mouth. Given the broad and shallow shelf off the South China coast, the South China contribution variations correspond with glacial–interglacial sea-level changes (Fig. 20G) (Shackleton, 1987). The highest value can

be found around ~16 ka BP (H1), rather than during the Last Glacial Maximum when the sea level stand was lowest, possibly reflecting the influence of a migrating rain front due to the southward shift of ITCZ, which enhances the physical erosion on the exposed shelf. Therefore, the South China contributions to the northern slope are primary affected by the sea-level changes, possibly associated with the monsoonal rainfall migration during the H1 event.

6. Conclusions

The unique geographical features and complicated ocean current dynamics coupled with the largest fluvial sediment discharge in a single semi-enclosed system allow us to assess source-to-sink transport processes in the South China Sea (SCS). For the first time, this study synthesizes existing clay mineralogical and geochemical data from ~1500 seafloor and river surface samples, covering the entire SCS region and 180 surrounding fluvial systems. Combined with deepwater in situ mooring observations, these data are used to describe modern SCS sediment transport processes from the river mouth to the continental shelf and then to the abyssal basin. Source-to-sink transport processes during the last glaciation are quantitatively reconstructed using high-resolution clay mineralogy records obtained from six high-quality sediment cores that are distributed in the northern, western, and southern SCS. Our results suggest that clay minerals have the potential for efficiently identifying source-to-sink transport processes, although approaches based on major-element geochemistry and Nd and Sr isotopes also contribute to this topic. We emphasize the following conclusions based on this synthesis:

1. The high diversity of clay mineral and geochemical compositions of fluvial sediments surrounding the SCS is attributable to the different levels of chemical weathering occurring on neighboring land areas. Comparing the spatial distribution pattern of the clay mineral species, four plausible mechanisms contributing to regional variability in chemical weathering can be summarized: (1) A long-term tropical warm and humid climate combined with a relatively stable tectonic setting leads to strongly intensive chemical weathering regardless of the variability in parent rocks, e.g., the Malay Peninsula and Sumatra. (2) Strong tectonic uplift combined with a tropical warm and humid climate or a stable tectonic setting combined with a subtropical warm and humid climate can induce moderate–intensive chemical weathering, e.g., Borneo and South China. (3) Strong tectonic uplift combined with a subtropical warm and humid climate can produce moderate chemical weathering, e.g., Taiwan and the Indochina Peninsula. (4) Lithology-dominated control (volcanic rocks) under subtropical climate conditions usually yields low to moderate chemical weathering, e.g., Luzon.
2. The effects of provenance control pattern and differential settling, two critical controlling mechanisms for source-to-sink transport processes, can be distinguished by the distribution of clay mineral assemblages combined with Nd and Sr isotopic compositions on the entire seafloor. Three significant features are summarized: (1) Strong provenance control on clay mineral distribution commonly occurs on portions of the seafloor adjacent to the drainage systems with prevailing clay mineral species, e.g., high contents of illite and chlorite in the northeastern SCS nearby Taiwan and high content of smectite in the eastern SCS nearby Luzon. (2) Strong differential settling occurs at least for kaolinite and smectite during their transport from fluvial estuary to abyssal basin; kaolinite has a weak cation exchange ability and can flocculate into large aggregates immediately upon entering a saltwater environment, whereas smectite particles can be transported for a long distance by various current systems. (3) High homogeneity of the four principal clay mineral species in the western and southern SCS is regarded as the result of intense mixing by the surface current systems.
3. Plausible mechanisms for modern source-to-sink transport processes are proposed by combining the clay mineralogical distribution on the seafloor with observed oceanic current systems. (1) In the northern SCS, smectite derived from Luzon is transported mainly by surface current with significant influence of the Kuroshio Current intrusion, illite and chlorite from Taiwan are mainly carried by the deep SCS Contour Current, while kaolinite from the Pearl River is clearly transported by the eastward Guangdong Coastal Current. The integrated deepwater mooring observation (TJ-A-1) confirmed that tremendous amounts of sediment derived from Taiwan are transported southwestward along the lower slope to the northwestern SCS by mesoscale eddies. (2) In the eastern SCS, the distinctive smectite content may be produced through chemical weathering of volcanic ash on the seafloor. (3) In the western and southern SCS, the transport pathway of clay minerals is difficult to identify because of highly homogenized clay–mineral distributions due to mixing by surface current systems.
4. High-resolution analysis of glacial–cyclic terrigenous input during the Late Quaternary reveals different sediment transport patterns in the northern, western, and southern SCS owing to changes in the land–sea configuration during the glacial periods. (1) In the northern SCS, terrigenous input was mainly controlled by provenance supply and ocean transport, with three major provenances contributing respective, but similar, clay mineral assemblages during both glacial and interglacial periods. (2) In the western SCS, the terrigenous clay assemblage reflects variations of the prevailing surface current influenced by monsoon winds, e.g., kaolinite mainly from the Pearl River was transported southward during the glacial periods, and illite and chlorite mainly from the Mekong River are transported northward during the interglacial periods. (3) In the southern SCS, the clay mineral input indicates intensive chemical weathering during the interglacial periods and strengthened physical erosion during the glacial periods. This is evident in the Mekong River drainage system where the clay mineralogy reflects the contemporaneous climatic change, which is controlled mainly by the East Asian monsoon evolution.
5. Terrigenous sediment transport processes dating back to the last glaciation are quantitatively reconstructed through analysis of two deepwater sediment cores located in the northern SCS. The contributions from three provenances (Luzon, Taiwan, and South China), quantified at high-resolution, show distinctive variations since 28 ka BP: (1) Contributions from South China to the two sites are similar, both with an increase up to 25% centered at 16 ka BP (ranging from 20 to 12 ka BP) from a general value of 10% to the peak value of 35%. The increase was caused by the southward shift of ITCZ during the H1 event and the early stage of deglacial sea-level rise. (2) Contributions from Luzon to the two sites during the Holocene are similar at around 30%, but about 15% higher on the westerly site (MD05-2904) than on the easterly site (MD05-2905) during the glacial period, implying more efficient westward transport of smectite from Luzon, controlled by the intensified influence of the Kuroshio Current intrusion. (3) Contributions from Taiwan to the easterly site (MD05-2905) remain at around 60% throughout the record, but show a 20% decrease during the glacial period and 5% decrease during the Holocene at the westerly site (MD05-2904), implying the stronger deepwater (contour current) transporting capability during the Holocene.

Supplementary data to this article can be found online at http://dx.doi.org/10.1016/j.earscirev.2015.08.005.

Acknowledgments

This study is a synthesis of the results of National Natural Science Foundation of China (NSFC) projects "Source, Transport, and Sedimentation of Terrigenous Sediments in the South China Sea (No. 40925008)"

and "In-Situ Observation of Bottom Current and Sediment Transport in the Northeastern South China Sea (No. 91128206)", and IOC-WESTPAC project "South China Sea Fluvial Sediments and Environmental Changes (FluSed)". Seafloor surface or core top samples were from many oceanic expeditions, including R/V SONNE 95, 115, 132, 140, 187, and 220 cruises in the central and southern South China Sea and the Gulf of Tonkin, and R/V Ocean Researcher-I and Ocean Researcher-II cruises in the Taiwan Strait and the northeastern South China Sea. Five sediment cores used in this study were from R/V Marion Dufresne cruise IMAGES-MARCO POLO. Lei Shao and Peijun Qiao from the State Key Laboratory of Marine Geology, Tongji University, are thanked for sharing Nd isotopic data and technical help during the geochemical analysis. We especially thank J.P. Walsh and Patricia Wiberg (Guest Editors), Paul Liu, and an anonymous reviewer for their constructive reviews on the early version of this paper. The work is also supported by the French-Chinese International Associated Laboratories (LIA) project MONOCL, the "Agence Nationale de la Recherche" through the project L-IPSL (ANR-10-LABX-18-01).

Authors would like to dedicate this paper to the friendship and memory of Prof. Chih-An Huh (co-author of this study), who passed way when the manuscript was in the peer-review process. Prof. Huh directed all his enthusiasm toward his favorite study and shared hundreds of sediment samples in the Taiwan Strait to this paper.

References

Barber, A.J., Crow, M.J., 2009. Structure of Sumatra and its implications for the tectonic assembly of Southeast Asia and the destruction of Paleotethys. Island Arc 18, 3–20.
Biscaye, P.E., 1965. Mineralogy and sedimentation of recent deep-sea clay in the Atlantic Ocean and adjacent seas and oceans. Geol. Soc. Am. Bull. 76, 803–832.
Boulay, S., Colin, C., Trentesaux, A., Frank, N., Liu, Z.F., 2005. Sediment sources and East Asian monsoon intensity over the last 450 ky. Mineralogical and geochemical investigations on South China Sea sediments. Palaeogeogr. Palaeoclimatol. Palaeoecol. 228, 260–277.
Boulay, S., Colin, C., Trentesaux, A., Clain, S., Liu, Z.F., Lauer-Leredde, C., 2007. Sedimentary responses to the Pleistocene climatic variations recorded in the South China Sea. Quat. Res. 68, 162–172.
Briais, A., Patriat, P., Tapponnier, P., 1993. Updated interpretation of magnetic anomalies and seafloor spreading stages in the South China Sea: implications for the tertiary tectonics of Southeast Asia. J. Geophys. Res. Solid Earth 98 (B4), 6299–6328.
Caruso, M.J., Gawarkiewicz, G.G., Beardsley, R.C., 2006. Interannual variability of the Kuroshio intrusion in the South China Sea. J. Oceanogr. 62, 559–575.
Chamley, H., 1989. Clay Sedimentology. Springer, New York (623 pp.).
Chang, Y.T., Hsu, W.L., Tai, J.H., Tang, T.Y., Chang, M.H., Chao, S.Y., 2010. Cold deep water in the South China Sea. J. Oceanogr. 66, 183–190.
Chen, P.Y., 1978. Minerals in bottom sediments of the South China Sea. Geol. Soc. Am. Bull. 89, 211–222.
Chu, P.C., Wang, G., 2003. Seasonal variability of thermohaline front in the central South China Sea. J. Oceanogr. 59, 65–78.
Clift, P.D., Lee, J.I., Clark, M.K., Blusztajn, J., 2002. Erosional response of South China to arc rifting and monsoonal strengthening; a record from the South China Sea. Mar. Geol. 184, 207–226.
Clift, P.D., Wan, S.M., Blusztajn, J., 2014. Reconstructing chemical weathering, physical erosion and monsoon intensity since 25 Ma in the northern South China Sea: a review of competing proxies. Earth-Sci. Rev. 130, 86–102.
Colin, C., Turpin, L., Bertaux, J., Desprairies, A., Kissel, C., 1999. Erosional history of the Himalayan and Burman ranges during the last two glacial–interglacial cycles. Earth Planet. Sci. Lett. 171, 647–660.
Colin, C., Turpin, L., Blamart, D., Frank, N., Kissel, C., Duchamp, S., 2006. Evolution of weathering patterns in the Indo-Burman Ranges over the last 280 kyr: effects of sediment provenance on $^{87}Sr/^{86}Sr$ ratios tracer. Geochem. Geophys. Geosyst. 7, Q03007. http://dx.doi.org/10.1029/2005GC000962.
Commission for the Geological Map of the World, 1975. Geological World Atlas, scale 1: 10,000,000. U. N. Educ. Sci. and Cult. Org., Paris.
Copard, K., Colin, C., Douville, E., Freiwald, A., Gudmundsson, G., Mol, B.D., Frank, N., 2010. Nd isotopes in deep-sea corals in the North-eastern Atlantic. Quat. Sci. Rev. 29, 2499–2508.
Dadson, S.J., Hovius, N., Chen, H., Dade, W.B., Hsieh, M.L., Willett, S.D., Hu, J.C., Horng, M.J., Chen, M.C., Stark, C.P., Lague, D., Lin, J.C., 2003. Links between erosion, runoff variability and seismicity in the Taiwan orogen. Nature 426, 648–651.
De Morais, J.O., Tintelnot, M., Irion, G., Souza Pinheiro, L., 2006. Pathways of clay mineral transport in the coastal zone of the Brazilian continental shelf from Ceará to the mouth of the Amazon River. Geo-Mar. Lett. 26, 16–22.
Expedition 349 Scientists, 2014. South China Sea tectonics: opening of the South China Sea and its implications for southeast Asian tectonics, climates, and deep mantle processes since the late Mesozoic. International Ocean Discovery Program Preliminary Report 349. http://dx.doi.org/10.14379/iodp.pr.349.2014.
Fang, G.H., Fang, W.D., Fang, Y., Wang, K., 1998. A survey of studies on the South China Sea upper ocean circulation. Acta Oceanogr. Taiwan. 37 (1), 1–16.
Ge, H.M., Li, Q.Y., Cheng, X.R., Zheng, H.B., He, J., 2010. Late Quaternary high resolution monsoon records in planktonic stable isotopes from northern South China Sea. Earth Sci. J. China Univ. Geosci. 35, 515–525 (in Chinese with English abstract).
Ge, Q., Liu, J.P., Xue, Z., Chu, F.Y., 2014. Dispersal of the Zhujiang River (Pearl River) derived sediment in the Holocene. Acta Oceanol. Sin. 33 (8), 1–9.
Gibbs, R.J., 1977. Clay mineral segregation in the marine environment. J. Sediment. Res. 47, 237–243.
Goldstein, S.J., Jacobsen, S.B., 1988. Nd and Sr isotopic systematics of river water suspended material — implications for crustal evolution. Earth Planet. Sci. Lett. 87, 249–265.
Grousset, F.E., Biscaye, P.E., Zindler, A., Prospero, J., Chester, R., 1988. Neodymium isotopes as tracers in marine sediments and aerosols: North Atlantic. Earth Planet. Sci. Lett. 87, 367–378.
Hall, R., 2002. Cenozoic geological and plate tectonic evolution of SE Asia and the SW Pacific: computer-based reconstructions, model and animations. J. Asian Earth Sci. 20, 353–431.
Hayes, D.E., Lewis, S.D., 1984. A geophysical study of the Manila Trench, Luzon, Philippines 1. Crustal structure, gravity, and regional tectonic evolution. J. Geophys. Res. 89, 9171–9195.
Hiscott, R.N., 2001. Depositional sequences controlled by high rates of sediment supply, sea-level variations, and growth faulting: the Quaternary Baram Delta of northwestern Borneo. Mar. Geol. 175, 67–102.
Holtzapffel, T., 1985. Les Minéraux Argileux: Préparation, Analyse Diffractométrique et Determination. Soc. Géol. Nord Publ. 12 (136 pp.).
Hu, J., Kawamura, H., Hong, H., Qi, Y., 2000. A review on the currents in the South China Sea: seasonal circulation, South China Sea warm current and Kuroshio intrusion. J. Oceanogr. 56, 607–624.
Huang, W., 2004. Sediment Distributional Patterns and Evolution in the South China Sea Since the Oligocene (Doctoral Dissertation (in Chinese with English abstract)), Tongji University, Shanghai (113 pp.).
Huang, W., Wang, P.X., 2006. Sediment mass and distribution in the South China Sea since the Oligocene. Sci. China D 49 (11), 1147–1155.
Huang, C.-Y., Wu, W.Y., Chang, C.P., Tsao, S., Yuan, P.B., Lin, C.W., Xia, K.Y., 1997. Tectonic evolution of accretionary prism in the arc–continent collision terrane of Taiwan. Tectonophysics 281, 31–35.
Huh, C.-A., Chen, W.F., Hsu, F.-H., Su, C.-C., Chiu, J.-K., Lin, S., Liu, C.-S., Huang, B.-J., 2011. Modern (<100 years) sedimentation in the Taiwan Strait: rates and source-to-sink pathways elucidated from radionuclides and particle size distribution. Cont. Shelf Res. 31, 47–63.
Hutchison, C.S., 1968. Dating tectonism in the Indosinian–Thai-Malayan orogen by thermoluminescence. Geol. Soc. Am. Bull. 79, 375–386.
Hutchison, C.S., 2005. Geology of North-west Borneo: Sarawak, Brunei and Sabah. Elsevier Science, Amsterdam (444 pp.).
Jacobsen, S.B., Wasserburg, G.J., 1980. Sm–Nd isotopic evolution of chondrites. Earth Planet. Sci. Lett. 50, 139–155.
Johnson, A.G., Kelley, J.T., 1984. Temporal, spatial, and textural variation in the mineralogy of Mississippi River suspended sediment. J. Sediment. Petrol. 54, 67–72.
Kondolf, G.M., Gao, Y.X., Annandale, G.W., Morris, G.L., Jiang, E.H., Zhang, J.H., Cao, Y.T., Carling, P., Fu, K.D., Guo, Q.C., Hotchkiss, R., Peteuil, C., Sumi, T., Wang, H.-W., Wang, Z.M., Wei, Z.L., Wu, B.S., Wu, C.P., Yang, C.T., 2014. Sustainable sediment management in reservoirs and regulated rivers: experiences from five continents. Earth's Futur. 2, 256–280. http://dx.doi.org/10.1002/2013EF000184.
Leloup, P.H., Arnaud, N., Lacassin, R., Kienast, J.R., Harrison, T.M., Trinh, P., Replumaz, A., Tapponnier, P., 2001. New constraints on the structure, thermochronology, and timing of the Ailao Shan-Red River shear zone, SE Asia. J. Geophys. Res. 106, 6683–6732.
Li, X.-H., Wei, G.J., Shao, L., Liu, Y., Liang, X.R., Jian, Z.M., Sun, M., Wang, P.X., 2003. Geochemical and Nd isotopic variations in sediments of the South China Sea: a response to Cenozoic tectonism in SE Asia. Earth Planet. Sci. Lett. 211, 207–220.
Li, Q.Y., Wang, P.X., Zhao, Q.H., Shao, L., Zhong, G.F., Tian, J., Cheng, X.R., Jian, Z.M., Su, X., 2006. A 33 Ma lithostratigraphic record of tectonic and paleoceanographic evolution of the South China Sea. Mar. Geol. 230, 217–235.
Li, C.-F., Xu, X., Lin, J., Sun, Z., Zhu, J., Yao, Y.J., Zhao, X.X., Liu, Q.S., Kulhanek, D.K., Wang, J., Song, T.R., Zhao, J.F., Qiu, N., Guan, Y.X., Zhou, Z.Y., Williams, T., Bao, R., Briais, A., Brown, E.A., Chen, Y.F., Clift, P.D., Colwell, F.S., Dadd, K.A., Ding, W.W., Almeida, I.H., Huang, X.-L., Hyun, S., Jiang, T., Koppers, A.A.P., Li, Q.Y., Liu, C.L., Liu, Z.F., Nagai, R.H., Peleo-Alampay, A., Su, X., Tejada, M.L.G., Trinh, H.S., Yeh, Y.-C., Zhang, C.-L., Zhang, F., Zhang, G.-L., 2014. Ages and magnetic structures of the South China Sea constrained by deep tow magnetic surveys and IODP Expedition 349. Geochem. Geophys. Geosyst. 15. http://dx.doi.org/10.1002/2014GC005567.
Li, X.J., Liu, Z.F., Colin, C., Yang, W.G., 2015. Time series contribution of clay minerals to the northern South China Sea since the last glaciation: implications for the deepwater current evolution. Mar. Geol. (under review).
Liu, Z.F., Li, X.J., 2011. Discussion on smectite formation in South China Sea sediments. Quat. Sci. 31, 199–206 (in Chinese with English abstract).
Liu, Z.F., Stattegger, K., 2014. South China Sea fluvial sediments: an introduction. J. Asian Earth Sci. 79, 507–508.
Liu, Z.F., Trentesaux, A., Clemens, S.C., Colin, C., Wang, P.X., Huang, B.Q., Boulay, S., 2003. Clay mineral assemblages in the northern South China Sea: implications for East Asian monsoon evolution over the past 2 million years. Mar. Geol. 201, 133–146.
Liu, Z.F., Colin, C., Trentesaux, A., Blamart, D., Bassinot, F., Siani, G., Sicre, M.-A., 2004. Erosional history of the eastern Tibetan Plateau since 190 kyr ago: clay mineralogical and geochemical investigations from the southwestern South China Sea. Mar. Geol. 209, 1–18.
Liu, Z.F., Colin, C., Trentesaux, A., Siani, G., Frank, N., Blamart, D., Farid, S., 2005. Late Quaternary climatic control on erosion and weathering in the eastern Tibetan Plateau and the Mekong Basin. Quat. Res. 63, 316–328.

Liu, Z.F., Colin, C., Huang, W., Chen, Z., Trentesaux, A., Chen, J.F., 2007a. Clay minerals in surface sediments of the Pearl River drainage basin and their contribution to the South China Sea. Chin. Sci. Bull. 52, 1101–1111.
Liu, Z.F., Colin, C., Huang, W., Le, K.P., Tong, S.Q., Chen, Z., Trentesaux, A., 2007b. Climatic and tectonic controls on weathering in South China and the Indochina Peninsula: clay mineralogical and geochemical investigations from the Pearl, Red, and Mekong drainage basins. Geochem. Geophys. Geosyst. 8, Q05005. http://dx.doi.org/10.1029/2006GC001490.
Liu, Z.F., Zhao, Y.L., Li, J.R., Colin, C., 2007c. Late Quaternary clay minerals off Middle Vietnam in the western South China Sea: implications for source analysis and East Asian monsoon evolution. Sci. China Ser. D Earth Sci. 50, 1674–1684.
Liu, J.P., Liu, C.S., Xu, K.H., Milliman, J.D., Chiu, J.K., Kao, S.J., Lin, S.W., 2008a. Flux and fate of small mountainous rivers derived sediments into the Taiwan Strait. Mar. Geol. 256, 65–76.
Liu, Z.F., Tuo, S.T., Colin, C., Liu, J.T., Huang, C.-Y., Selvaraj, K., Chen, C.-T.A., Zhao, Y.L., Siringan, F.P., Boulay, S., Chen, Z., 2008b. Detrital fine-grained sediment contribution from Taiwan to the northern South China Sea and its relation to regional ocean circulation. Mar. Geol. 255, 149–155.
Liu, J.P., Xue, Z., Ross, K., Wang, H.J., Yang, Z.S., Li, A.C., Gao, S., 2009a. Fate of sediments delivered to the sea by Asian large rivers: long-distance transport and formation of remote alongshore clinothems. Sediment. Rec. 7 (4), 4–9.
Liu, Z.F., Zhao, Y.L., Colin, C., Siringan, F.P., Wu, Q., 2009b. Chemical weathering in Luzon, Philippines from clay mineralogy and major-element geochemistry of river sediments. Appl. Geochem. 24, 2195–2205.
Liu, J.G., Chen, M.H., Chen, Z., Yan, W., 2010a. Clay mineral distribution in surface sediments of the South China Sea and its significance for in sediment sources and transport. Chin. J. Oceanol. Limnol. 28, 407–415.
Liu, Z.F., Colin, C., Li, X.J., Zhao, Y.L., Tuo, S.T., Chen, Z., Siringan, F.P., Liu, J.T., Huang, C.-Y., You, C.-F., Huang, K.-F., 2010b. Clay mineral distribution in surface sediments of the northeastern South China Sea and surrounding fluvial drainage basins: source and transport. Mar. Geol. 277, 48–60.
Liu, Z.F., Li, X.J., Colin, C., Ge, H.M., 2010c. A high-resolution clay mineralogical record in the northern South China Sea since the Last Glacial Maximum, and its time series provenance analysis. Chin. Sci. Bull. 55, 4058–4068.
Liu, J.G., Xiang, R., Chen, M.H., Chen, Z., Yan, W., Liu, F., 2011. Influence of the Kuroshio Current intrusion on depositional environment in the northern South China Sea: evidence from surface sediment records. Mar. Geol. 285, 59–68.
Liu, Z.F., Wang, H., Hantoro, W.S., Sathiamurthy, E., Colin, C., Zhao, Y.L., Li, J.R., 2012. Climatic and tectonic controls on chemical weathering in tropical Southeast Asia (Malay Peninsula, Borneo, and Sumatra). Chem. Geol. 291, 1–12.
Liu, J.G., Xiang, R., Chen, Z., Chen, M.H., Yan, W., Zhang, L.L., Chen, H., 2013a. Sources, transport and deposition of surface sediments from the South China Sea. Deep-Sea Res. I 71, 92–102.
Liu, J.T., Kao, S.-J., Huh, C.-A., Hung, C.-C., 2013b. Gravity flows associated with flood events and carbon burial: Taiwan as instructional source area. Annu. Rev. Mar. Sci. 5, 47–68.
Liu, J.G., Clift, P.D., Yan, W., Chen, Z., Chen, H., Xiang, R., Wang, D.X., 2014. Modern transport and deposition of settling particles in the northern South China Sea: sediment trap evidence adjacent to Xisha Trough. Deep-Sea Res. I 193, 145–155.
Lüdmann, T., Wong, H.K., Berglar, K., 2005. Upward flow of North Pacific Deep Water in the northern South China Sea as deduced from the occurrence of drift sediments. Geophys. Res. Lett. 32, L05614. http://dx.doi.org/10.1029/2004GL021967.
Milliman, J.D., Farnsworth, K.L., 2011. River Discharge to the Coastal Ocean: A Global Synthesis. Cambridge University Press, Cambridge (384 pp.).
Milliman, J.D., Syvitski, J.P.M., 1992. Geomorphic/tectonic control of sediment discharge to the ocean: the importance of small mountainous rivers. J. Geol. 100, 525–544.
Milliman, J.D., Farnsworth, K.L., Albertin, C.S., 1999. Flux and fate of fluvial sediments leaving large islands in the East Indies. J. Sea Res. 41, 97–107.
Nesbitt, H.W., Young, G.M., 1982. Early Proterozoic climates and plate motions inferred from major element chemistry of lutites. Nature 299, 715–717.
Nesbitt, H.W., Young, G.M., 1984. Prediction of some weathering trends of plutonic and volcanic rocks based on thermodynamic and kinetic considerations. Geochim. Cosmochim. Acta 48, 1523–1534.
Nesbitt, H.W., Young, G.M., 1989. Formation and diagenesis of weathering profiles. J. Geol. 97, 129–147.
Partin, J.W., Cobb, K.M., Adkins, J.F., Clark, B., Fernandes, D.P., 2007. Millennial-scale trends in west Pacific warm pool hydrology since the Last Glacial Maximum. Nature 449, 452–455.
Patchineelam, S.M., De Figueiredo, A.M., 2000. Preferential settling of smectite on the Amazon continental shelf. Geo-Mar. Lett. 20, 37–42.
Petschick, R., 2000. MacDiff 4.2.2 [online] Available: http://www.geol-pal.uni-frankfurt.de/Staff/Homepages/Petschick/MacDiff/MacDiffInfoE.html (Cited 01-12-2001).
Qu, T.D., Kim, Y.Y., Yaremchuk, M., Tozuka, T., Ishida, A., Yamagata, T., 2004. Can Luzon Strait transport play a role in conveying the impact of ENSO to the South China Sea? J. Clim. 17, 3644–3657.
Qu, T.D., Girton, J.B., Whitehead, J.A., 2006. Deepwater overflow through Luzon Strait. J. Geophys. Res. 111, C01002. http://dx.doi.org/10.1029/2005JC003139.
Rangin, C., Bellon, H., Benard, F., Letouzey, J., Muller, C., Sanudin, T., 1990. Neogene arc–continent collision in Sabah, Northern Borneo (Malaysia). Tectonophysics 183, 305–319.
Replumaz, A., Lacassin, R., Tapponnier, P., Leloup, P.H., 2001. Large river offsets and Plio-Quaternary dextral strike-slip rate on the Red River fault (Yunnan, China). J. Geophys. Res. 106, 819–836.
Saito, Y., Chaimanee, N., Jaropongsakul, T., Syvitski, J.P.M., 2007. Shrinking megadeltas in Asia: Sea-level rise and sediment reduction impacts from case study of the Chao Phraya Delta. LOICZ Inprint 2, 3–9.
Sawada, K., Handa, N., 1998. Variability of the path of the Kuroshio ocean current over the past 25,000 years. Nature 392, 592–595.
Schoenbohm, L.M., Whipple, K.X., Burchfiel, B.C., Chen, L., 2004. Geomorphic constraints on surface uplift, exhumation, and plateau growth in the Red River region, Yunnan Province, China. Geol. Soc. Am. Bull. 116, 895–909.
Shackleton, N.J., 1987. Oxygen isotopes, ice volume and sea level. Quat. Sci. Rev. 6, 183–190.
Shao, L., Li, X., Geng, J., Pang, X., Lei, Y., Qiao, P., Wang, L., Wang, H., 2007. Deep water bottom current deposition in the northern South China Sea. Sci. China Ser. D Earth Sci. 50, 1060–1066.
Shao, L., Qiao, P.J., Pang, X., Wei, G.J., Li, Q.Y., Miao, W.L., Li, A., 2009. Nd isotopic variations and its implications in the recent sediments from the northern South China Sea. Chin. Sci. Bull. 54, 311–317.
Shaw, P.-T., Chao, S.-Y., 1994. Surface circulation in the South China Sea. Deep-Sea Res. I 41, 1663–1683.
Shi, M.C., Chen, C.S., Xu, Q.C., Lin, H.C., Liu, G.M., Wang, H., Wang, F., Yan, J.H., 2002. The role of the Qiongzhou Strait in the seasonal variation of the South China Sea Circulation. J. Phys. Oceanogr. 32 (1), 103–121.
Shi, X.F., Liu, S.F., Fang, X.S., Qiao, S.Q., Khokiattiwong, S., Kornkanitnan, N., 2015. Distribution of clay minerals in surface sediments of the western Gulf of Thailand: sources and transport patterns. J. Asian Earth Sci. http://dx.doi.org/10.1016/j.jseaes.2015.02.005.
Stattegger, K., Kuhnt, W., Wong, H.K., Bühring, C., Haft, C., Hanebuth, T., Kawamura, H., Kienast, M., Lorenc, S., Lotz, B., Lüdmann, T., Lurati, M., Mühlhan, N., Paulsen, A.-M., Paulsen, J., Pracht, J., Putar-Roberts, A., Hung, N.Q., Richter, A., Salomon, B., Schimanski, A., Steinke, S., Szarek, R., Nhan, N.V., Weinelt, M., Winguth, C., 1997. Sequence stratigraphy, Late Pleistocene–Holocene sea level fluctuations and high resolution record of the post-Pleistocene transgressive on the Sunda Shelf. Cruise Report RV SONNE 115, Kota Kinabalu—Singapore, December 13, 1996–January 25, 1997 (211 pp.).
Staub, J.R., Among, H.L., Gastaldo, R.A., 2000. Seasonal sediment transport and deposition in the Rajang River delta, Sarawak, East Malaysia. Sediment. Geol. 133, 149–264.
Steinke, S., Hanebuth, T.J.J., Vogt, C., Stattegger, K., 2008. Sea level induced variations in clay mineral composition in the southwestern South China Sea over the past 17,000 yr. Mar. Geol. 250, 199–210.
Steuer, S., Franke, D., Meresse, F., Savva, D., Pubellier, M., Auxietre, J.-L., Aurelio, M., 2013. Time constraints on the evolution of southern Palawan Island, Philippines from onshore and offshore correlation of Miocene limestones. J. Asian Earth Sci. 76, 412–427.
Su, J., 2004. Overview of the South China Sea circulation and its influence on the coastal physical oceanography near the Pearl River Estuary. Cont. Shelf Res. 24, 1745–1760.
Sultan, K., Shazili, N.A., 2009. Distribution and geochemical baselines of major, minor and trace elements in tropical topsoils of the Terengganu River basin, Malaysia. J. Geochem. Explor. 103, 57–68.
Suzuki, S., Shizuo, T., Graciano, P.Y., Sevillo, D.D., Daniel, K.A., 2000. Composition and provenance of the upper cretaceous to Eocene sandstones in central Palawan, Philippines: constraints on the tectonic development of Palawan. Island Arc 9, 611–626.
Tamburini, F., Adatte, T., Föllmi, K., Bernasconi, S.M., Steinmann, P., 2003. Investigating the history of East Asian monsoon and climate during the last glacial interglacial period (0–140,000 years): mineralogy and geochemistry of ODP sites 1143 and 1144, South China Sea. Mar. Geol. 201, 147–168.
Tangang, F.T., Xia, C.S., Qiao, F.L., Juneng, L., Shan, F., 2011. Seasonal circulation in the Malay Peninsula eastern continental shelf from a wave-tide-circulation coupled model. Ocean Dyn. 61, 1317–1328.
Tapponnier, P., Peltzer, G., Le Dain, A.Y., Armijo, R., Cobbold, P., 1982. Propagating extrusion tectonics in Asia: new insights from simple experiments with plasticine. Geology 10, 611–616.
Taylor, B., Hayes, D.E., 1980. The tectonic evolution of the South China Basin. In: Hayes, D.E. (Ed.), The Tectonic and Geologic Evolution of Southeast Asian Seas and Islands. Geophysical Monograph 23, pp. 89–104.
Taylor, B., Hayes, D.E., 1983. Origin and history of the South China Sea Basin. In Hayes, D.E. (Ed.), the tectonic and geologic evolution of Southeast Asian seas and islands (Pt. 2). Geophys. Monogr. 27, 23–56.
Taylor, S.R., McLennan, S.M., 1985. The Continental Crust: Its Composition and Evolution. Blackwell, Malden, Mass. (312 pp.).
Tian, J.W., Qu, T.D., 2012. Advances in research on the deep South China Sea circulation. Chin. Sci. Bull. 57, 3115–3120.
Unverricht, D., Nguyen, T.C., Heinrich, C., Szczuciński, W., Lahajnar, N., Stattegger, K., 2014. Suspended sediment dynamics during the inter-monsoon season in the subaqueous Mekong Delta and adjacent shelf, southern Vietnam. J. Asian Earth Sci. 79, 509–519.
Wan, S.M., Li, A.C., Clift, P.D., Stuut, J.-B.W., 2007. Development of the East Asian monsoon: mineralogical and sedimentologic records in the northern South China Sea since 20 Ma. Palaeogeogr. Palaeoclimatol. Palaeoecol. 254, 561–582.
Wan, S.M., Li, A.C., Clift, P.D., Wu, S.G., Xu, K.H., Li, T.G., 2010. Increased contribution of terrigenous supply from Taiwan to the northern South China Sea since 3 Ma. Mar. Geol. 278, 115–121.
Wang, P.X., Li, Q.Y. (Eds.), 2009. The South China Sea: Paleoceanography and SedimentologyDevelopment in Palaeoenvironmental Research vol. 13. Springer (506 pp.).
Wang, P.X., Wang, L.J., Bian, Y.P., Jian, Z.M., 1995. Late Quaternary paleoceanography of the South China Sea: surface circulation and carbonate cycles. Mar. Geol. 127, 145–165.
Wang, L., Sarnthein, M., Erlenkeuser, H., Grimalt, J., Grootes, P., Heilig, S., Ivanova, E., Kienast, M., Pelejero, C., Pflaumann, U., 1999. East Asian monsoon climate during the Late Pleistocene: high-resolution sediment records from the South China Sea. Mar. Geol. 156, 245–284.
Wang, P.X., Prell, W.L., Blum, P., et al., 2000. Proceedings of Ocean Drilling ProgramInitial Reports 184. Texas A&M University, College Station, USA.

Wang, Y.J., Cheng, H., Edwards, R.L., An, Z.S., Wu, J.Y., Shen, C.-C., Dorale, J.A., 2001. A high-resolution absolute-dated Late Pleistocene monsoon record from Hulu Cave, China. Science 294, 2345–2348.
Wang, B., Clemens, S.C., Liu, P., 2003. Contrasting the Indian and East Asian monsoons: implications on geological timescales. Mar. Geol. 201, 5–21.
Wang, G.H., Xie, S.-P., Qu, T.D., Huang, R.X., 2011. Deep South China Sea circulation. Geophys. Res. Lett. 38, L05601. http://dx.doi.org/10.1029/2010GL046626.
Wang, P.X., Li, Q.Y., Tian, J., 2014. Pleistocene paleoceanography of the South China Sea: progress over the last 20 years. Mar. Geol. 352, 381–396.
Wattayakorn, G., King, B., Wolanski, E., Suthanaruk, P., 1998. Seasonal dispersion of petroleum contaminants in the Gulf of Thailand. Cont. Shelf Res. 641–659.
Webster, P.J., 1994. The role of hydrological processes in ocean–atmosphere interactions. Rev. Geophys. 32, 427–476.
Wei, G.J., Liu, Y., Ma, J.L., Xie, L.H., Chen, J.F., Deng, W.F., Tang, S., 2012. Nd, Sr isotopes and elemental geochemistry of surface sediments from the South China Sea: implications for provenance tracing. Mar. Geol. 319–322, 21–34.
Wiesner, M.G., Wang, Y., Zheng, L., 1995. Fallout of volcanic ash to the deep South China Sea induced by the 1991 eruption of Mount Pinatubo (Philippines). Geology 23, 885–888.
Wiesner, M.G., Arpa, C., Bracker, E., Catane, S., de Leon, M., Duyanen, J., Faber, U., Gerbich, C., Hess, S., Holbourn, A., Kaminski, M., Krüger, O., Kuhnt, W., Suu, N.H., Paulsen, H., Peleo-Alampay, A., Rimek, R., Seemann, B., Siringan, F., Steen, E., Szarek, R., Son, V.D., von Wersch, V., Wetzel, A., 1999. Cruise Report RV SONNE 140, Leg B, South China Sea. Nha Trang—Manila, April 22–May 04, 1999 (22 pp.).
Wiesner, M.G., Wetzel, A., Catane, S.G., Listanco, E.L., Mirabueno, H.T., 2004. Grain size, areal thickness distribution and controls on sedimentation of the 1991 Mount Pinatubo tephra layer in the South China Sea. Bull. Volcanol. 66, 226–242.
Wiesner, M.G., Stattegger, K., Voß, M., Schwarzer, K., Pohlmann, T., Amann, T., Bombar, D., de Silva, L., Dippner, J., Cuong, D.H., Hai, D.N., Trung, K.D., Freing, A., Grosse, J., Heidemann, U., Hein, H., Heyckendorf, K., Jagodzinski, R., Kagelmacher, A., Lahajnar, N., Thuyen, L.X., Liskow, I., Moisander, P., Montoya, J., Minh, N.B., Cho, N.D., Huan, N.H., Vinh, N.K., Lam, N.N., Thanh, N.T., Tuan, N.V., Peinert, R., Peleo-Alampay, A., Phach, P.V., Schimanski, A., Steen, E., Stichel, T., Subramaniam, A., Szuzucinski, W., Chung, T.V., Unverricht, D., Quang, V.V., Welsch, A., Wetzel, A., 2006. Land–ocean–atmosphere interactions in the coastal zone of Vietnam. Cruise Report RV SONNE 187, Nagasaki–Nha Trang, March 31–May 13, 2006 (99 pp.).
Wiesner, M.G., Stattegger, K., Pohlmann, T., Chen, F.J., Heddaeus, A., Heyckendorf, K., Jechlitschek, H., Lahajnar, N., Liskow, I., Li, X.J., Liu, Z.F., Lorenc, S., Merfke, M., Müller, S., Paleo-Alampay, A., Schönke, M., Schwarzer, K., Szczygielski, A., Steen, E., Unverricht, D., Wang, X.H., Welsch, A., Wetzel, A., Zhao, Y.L., 2012. Land–ocean–atmosphere interactions in the Gulf of Tonkin. Cruise Report RV SONNE 220, Hongkong–Haiphong–Hongkong, April 14–May 16, 2012 (101 pp.).
Wu, D.X., Wang, Y., Lin, X.P., Yang, J.Y., 2008. On the mechanism of the cyclonic circulation in the Gulf of Tonkin in the summer. J. Geophys. Res. 113, C09029. http://dx.doi.org/10.1029/2007JC004208.
Xia, H.Y., Li, X.H., Shi, M.C., 2001. Three-D numerical simulation of wind-driven current and density current in the Beibu Gulf. Acta Oceanol. Sin. 20 (4), 455–472.
Xue, Z., Liu, J.P., DeMaster, D., Nguyen, V.L., Ta, T.K.O., 2010. Late Holocene evolution of the Mekong subaqueous delta, southern Vietnam. Mar. Geol. 269, 46–60.
Xue, Z., Liu, J.P., DeMaster, D., Leithold, E.L., Wan, S.M., Ge, Q., Nguyen, V.L., Ta, T.K.O., 2014. Sedimentary processes on the Mekong subaqueous delta: clay mineral and geochemical analysis. J. Asian Earth Sci. 79, 520–528.
Yang, W.G., 2008. High-resolution Sedimentary Records Since the Last Glacial in the Northern South China Sea and Its Paleoclimatic Evolution (PhD Dissertation (in Chinese with English abstract)), Tongji University, Shanghai (127 pp.).
Yu, M.G., Liu, J.F., 1993. The system and pattern of the South China Sea circulation (in Chinese). Ocean Predict. 10 (2), 13–17.
Yuan, D., Han, W., Hu, D., 2006. Surface Kuroshio path in the Luzon Strait area derived from satellite remote sensing data. J. Geophys. Res. 111, C11007. http://dx.doi.org/10.1029/2005JC003412.
Zhang, W., Wei, X.Y., Zheng, J.H., Zhu, Y.L., Zhang, Y.J., 2012. Estimating suspended sediment loads in the Pearl River Delta region using sediment rating curves. Cont. Shelf Res. 38, 35–46.
Zhang, Z.W., Zhao, W., Tian, J.W., Liang, X.F., 2013. A mesoscale eddy pair southwest of Taiwan and its influence on deep circulation. J. Geophys. Res. Oceans 118, 6479–6494. http://dx.doi.org/10.1002/2013JC008994.
Zhang, Y.W., Liu, Z.F., Zhao, Y.L., Wang, W.G., Li, J.R., Xu, J.P., 2014. Mesoscale eddies transport deep-sea sediments. Sci. Rep. 4, 5937. http://dx.doi.org/10.1038/srep05937.
Zhao, Y.L., Liu, Z.F., Colin, C., Xie, X., Wu, Q., 2011. Turbidite deposition in the southern South China Sea during the last glacial: evidence from grain-size and major elements records. Chin. Sci. Bull. 56, 3558–3565.
Zhao, W., Zhou, C., Tian, J.W., Yang, Q.X., Wang, B., Xie, L.L., Qu, T.D., 2014. Deep water circulation in the Luzon Strait. J. Geophys. Res. Oceans 119, 790–804. http://dx.doi.org/10.1002/2013JC009587.
Zhou, C., Zhao, W., Tian, J.W., Yang, Q.X., Qu, T.D., 2014. Variability of the deep water overflow in the Luzon Strait. J. Phys. Oceanogr. 44 (11), 2972–2986.